

AD_____

Award Number: W81XWH-06-1-0431

TITLE: Optimization of Tomosynthesis Imaging for Improved Mass and Microcalcification Detection in the Breast

PRINCIPAL INVESTIGATOR: Dan Xia

CONTRACTING ORGANIZATION: The University of Chicago
Chicago, IL, 60637

REPORT DATE: April 2009

TYPE OF REPORT: Annual Summary

PREPARED FOR: U.S. Army Medical Research and Materiel Command
Fort Detrick, Maryland 21702-5012

DISTRIBUTION STATEMENT: Approved for Public Release;
Distribution Unlimited

The views, opinions and/or findings contained in this report are those of the author(s) and should not be construed as an official Department of the Army position, policy or decision unless so designated by other documentation.

REPORT DOCUMENTATION PAGE

Form Approved
OMB No. 0704-0188

Public reporting burden for this collection of information is estimated to average 1 hour per response, including the time for reviewing instructions, searching existing data sources, gathering and maintaining the data needed, and completing and reviewing this collection of information. Send comments regarding this burden estimate or any other aspect of this collection of information, including suggestions for reducing this burden to Department of Defense, Washington Headquarters Services, Directorate for Information Operations and Reports (0704-0188), 1215 Jefferson Davis Highway, Suite 1204, Arlington, VA 22202-4302. Respondents should be aware that notwithstanding any other provision of law, no person shall be subject to any penalty for failing to comply with a collection of information if it does not display a currently valid OMB control number. PLEASE DO NOT RETURN YOUR FORM TO THE ABOVE ADDRESS.

1. REPORT DATE 01-04-2008	2. REPORT TYPE Annual Summary	3. DATES COVERED 15 Mar 2006 – 14 Mar 2008		
4. TITLE AND SUBTITLE Optimization of Tomosynthesis Imaging for Improved Mass and Microcalcification Detection in the Breast		5a. CONTRACT NUMBER		
		5b. GRANT NUMBER W81XWH-06-1-0431		
		5c. PROGRAM ELEMENT NUMBER		
6. AUTHOR(S) Dan Xia Email: DANXIA@UCHICAGO.EDU		5d. PROJECT NUMBER		
		5e. TASK NUMBER		
		5f. WORK UNIT NUMBER		
7. PERFORMING ORGANIZATION NAME(S) AND ADDRESS(ES) The University of Chicago Chicago, IL, 60637		8. PERFORMING ORGANIZATION REPORT NUMBER		
9. SPONSORING / MONITORING AGENCY NAME(S) AND ADDRESS(ES) U.S. Army Medical Research and Materiel Command Fort Detrick, Maryland 21702-5012		10. SPONSOR/MONITOR'S ACRONYM(S)		
		11. SPONSOR/MONITOR'S REPORT NUMBER(S)		
12. DISTRIBUTION / AVAILABILITY STATEMENT Approved for Public Release; Distribution Unlimited				
13. SUPPLEMENTARY NOTES				
14. ABSTRACT The goal of this research is to obtain systematic understandings of the effects of various physical factors that are important in breast tomosynthesis imaging and to develop techniques for effectively dealing with their effects and for reducing radiation dose. During the second year of the project we have achieved fruitful results based upon the progress made in our first year of the project. Specifically, we have further investigated the performance of the total-variation (TV) based algorithm under different data conditions and different constraint parameters. Furthermore, we have also proposed and investigated a new tomosynthesis imaging method with non-planar trajectories for yielding more data information with the same amount of imaging dose. We have also simulated the scatter in tomosynthesis breast imaging by convolving the ideal projection data with angular dependent scatter kernel.				
15. SUBJECT TERMS tomosynthesis, iterative algorithms, convergence, scanning configuration, physical factors				
16. SECURITY CLASSIFICATION OF: a. REPORT U		17. LIMITATION OF ABSTRACT UU	18. NUMBER OF PAGES 19	19a. NAME OF RESPONSIBLE PERSON USAMRMC
				19b. TELEPHONE NUMBER (include area code)

Table of Contents

	<u>Page</u>
Introduction.....	5
Body.....	6
Key Research Accomplishments.....	15
Reportable Outcomes.....	16
Conclusion.....	17
References.....	18
Appendices.....	20

INTRODUCTION

Breast tomosynthesis is a tomographic imaging technique, and it has the potential advantage to overcome a major limitation of conventional mammography through recovering, to a large degree, the loss of 3D information about the breast in conventional, 2D mammography [1]. In the last several years, there has been renewed interest in developing breast tomosynthesis for detection of breast cancer [2,3,4]. Although considerable progress has been made, improvements to several areas of breast tomosynthesis technology are still needed before it becomes suitable for routine clinical use. In essence, breast tomosynthesis can be considered as a dedicated computed tomography with limited view for breast imaging, and it thus requires the development of special reconstruction algorithms for recovering 3D breast images from tomosynthesis data. In addition, various physical factors in breast tomosynthesis can affect the resulting image quality, and the issue of patient radiation dose in breast tomosynthesis is of a concern. The overall objective of this project is to investigate and develop reconstruction algorithms for obtaining breast images of practical use, to investigate and evaluate systematically the effects of various physical factors on image quality in breast tomosynthesis, and to use and evaluate (empirical) techniques for effectively compensating for the effects on breast tomosynthesis images and for possibly reducing imaging radiation dose in breast tomosynthesis. It is fully expected that the research will contribute to the effort in the field to develop and improve breast tomosynthesis for its clinical use. This report summarizes the progress of this Predoctoral Traineeship Award project made by the recipient during the past three years.

BODY

1 Training Accomplishments

At the time of this report, the recipient of the Predoctoral Traineeship Award has taken 22 out of 22 required courses towards his Ph.D. degree in medical physics. The courses include physics of medical imaging, physics of radiation therapy, mathematics for medical physicists, image processing, statistics, anatomy of the body, radiation biology and teaching assistant training.

2 Research Accomplishments

In tomosynthesis, data are acquired only at a small number of projection views over a limited angular range. Therefore, tomosynthesis data are highly sparse as compared to data acquired in conventional computed tomography (CT). Consequently, existing analytical algorithms for accurate reconstruction of CT images are generally not suitable for yielding useful images from tomosynthesis data. For example, the effect of filtering may not completely be canceled out due to the limited number of views and limited angular range, resulting in prominent artifacts in reconstructed images. In contrast, iterative algorithms can generally yield images with less artifacts than can the analytic algorithms. In this project, we have investigated and developed a total variation (TV) based iterative algorithm for reconstructing accurate images from incomplete projection data.

The TV algorithm that is considered in the project seeks to find the solution for the constrained optimization problem [5]:

$$\vec{f}^* = \operatorname{argmin} \|\vec{f}\|_{TV}, \quad (1)$$

subject to two constraints,

$$|M\vec{f} - \vec{g}| \leq \epsilon \quad \text{and} \quad \vec{f} \geq 0,$$

where vectors \vec{f}^* and \vec{g} indicate the reconstructed image and measured tomosynthesis data, and matrix M is the linear operator representing the cone-beam forward projection in breast tomosynthesis. The inequality used in the first constraint accounts for data inconsistency, such as noise, continuous-to-discrete inconsistency, etc. The parameter ϵ can be selected for controlling the impact level of potential data inconsistency on the image reconstruction.

2.1 Investigation of reconstruction algorithms for ideal tomosynthesis data

In an attempt to evaluate the performance upper-bound of the TV algorithm, we have first investigated the performance of the TV algorithm when applied to ideal tomosynthesis data, which are generated from discrete images. We generated projection data with 20 views over an angular range 2π . In this simulation study, one has a discrete matrix system (i.e., the matrix M in Eq. (1)), which allows possible recovery of the underlying discrete images. Therefore, the results obtained

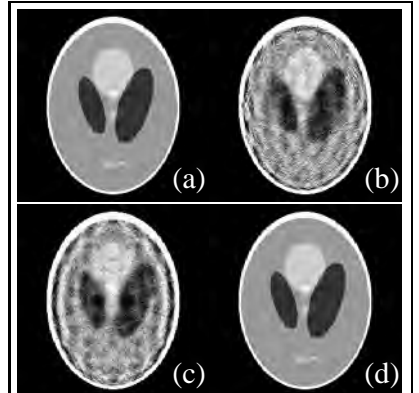


Figure 1: The Shepp-Logan phantom image (a) and the images reconstructed by use of (b) POCS, (c) EM, and (d) TV algorithms. The display gray scale is [0.9, 1.1].

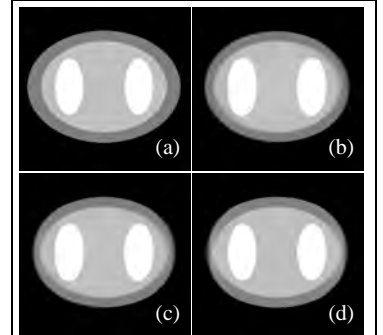


Figure 2: The phantom image (a) and the images reconstructed with different constraint parameter $\epsilon=13.1$ (b), $\epsilon=11.0$ (c), and $\epsilon=8.96$ (d). The display gray scale is [0.8, 1.2].

from ideal data provide us the upper bounds on the performance of the TV algorithm. For the comparison, we have also implemented two widely used existing iterative algorithms, projection onto convex set (POCS) algorithm [6] and expectation-maximization (EM) algorithm [7]. The results shown in Fig. 1 demonstrate that, under ideal situation, the TV algorithm can yield images with superior quality than POCS and EM algorithms. The results obtained are consistent with those obtained previously by our group [5].

2.2 Investigation of image reconstruction inconsistent tomosynthesis data

In the study described above, we have investigated the performance of the TV algorithm when applied to ideal tomosynthesis data, which are generated from an image on a discrete array. However, in realistic tomosynthesis imaging, the measured data are generally better modeled by use of continuous object functions. Because images can be reconstructed only for a discrete image from discrete data, discrete data generated from a continuous object function will contain some inconsistency. In this part of the study, we carried out studies on evaluation of the performance of the TV algorithm from data containing the continuous-to-discrete inconsistency. As mentioned previously, the parameter ϵ in TV algorithm is used for controlling the data inconsistency on the image reconstruction and different constraint parameter ϵ yields the image with different quality. Therefore, selection of a proper constraint parameter ϵ is important to achieve a good reconstruction from inconsistent tomosynthesis data.

We have investigated systematically the performance of the TV algorithm with different ϵ 's. In one of the studies, projection data on 20 views over an angular range 2π were generated analytically from a continuous phantom, as shown in Fig. 2a. Thus the generated projection data contain the continuous-to-discrete inconsistency. From this inconsistent data set, images were then reconstructed by selecting different ϵ 's. In Figs. 2b, c, and d, we show three images reconstructed by use of the TV algorithm with three different constraint parameters $\epsilon=8.96$, 11.0 , and 13.1 . The root-mean-square errors (RMSEs) between the true image and three reconstructed images, as an index of the image quality, have been calculated, which are 28.9 , 31.3 , and 33.2 , respectively. It can be observed that, the RMSE increases as ϵ increases. In general, a large constraint parameter ϵ results in the reconstructed image with a small total variation and the large difference between the reconstructed image and true image.

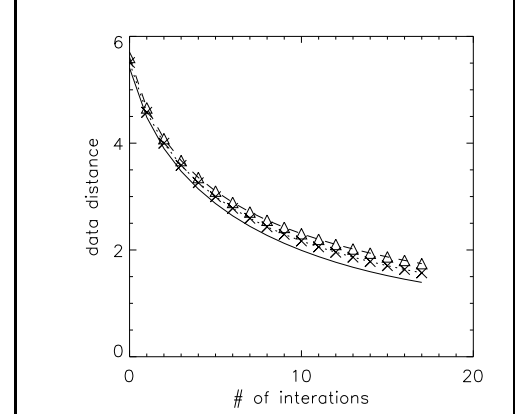


Figure 3: The data distance obtained by use of TV algorithm with different relaxation parameters: 0.90 (solid line), 0.95 (cross), and 0.99 (triangle). The image obtained with a small relaxation parameter has a small data distance for each iteration.

2.3 Improvement of TV algorithm efficiency

The convergence efficiency is important for iterative algorithms because, for most applications, it is desirable to obtain sufficiently accurate image in a given time. Therefore, a reconstruction algorithm which yields accurate image within a 10 – 30 iterations is preferable. The TV algorithm solves the constrained minimization problem by employing adaptive steepest descent POCS (ASD-POCS) to enforce the some convex constraints on the image, such as data fidelity and image-value positivity, combined with steepest descent to reduce TV of the image. However, a large number of iterations is required to reach the satisfactory solution, especially when the task is challenging (detecting a low contrast object) or when the data is inconsistent (noisy or high scatter contamination). By modifying the original TV algorithm, we have developed a new approach

to improve the efficiency of TV algorithm. The modification of the TV algorithm includes two aspects: (1) using ASD-POCS with adjusted relaxation parameters to let data fidelity satisfied within a few iterations, and (2) updating the image along a new direction, which is the combination of two gradient directions: data distance and TV.

We have investigated systematically the performance of the ASD-POCS with different relaxation parameters. From the same projection data set, several reconstructions were performed by choosing different relaxation parameters. In one of these studies, we generated projection data with 60 views over angular range π . From this data set, we have reconstructed images from this data set by use of the ASD-POCS with three different relaxation parameters, 0.90, 0.95, and 0.99. The distance between the data estimated from the reconstructed image and the generated data is used to indicate the degree of data fidelity. Our results demonstrate that this distance decreases fast when the small relaxation parameter is used, as shown in Fig. 3. So it provides a guidance to adjust the relaxation parameters in ASD-POCS to reach the desired data fidelity constraint within a small number of iterations.

The change of the image at each iteration is designed to along a new direction, which is formed by combining local data distance gradient direction and local image TV gradient direction. This modified approach tightly confines the updated image within the vicinity of the target data level set, and thus has higher efficiency in the TV minimization. We have modified the TV algorithm to incorporate this new direction for minimizing the TV. In example study, we have generated the projection data from the image shown in Fig. 4a. From the projection data set, the image was reconstructed by use of the proposed TV algorithm, which is shown in Fig. 4b. For the comparison, the image reconstructed by use of the original TV algorithm from the same data is also displayed in Fig. 4c. The corresponding image TVs are also displayed in Fig. 5, which clearly demonstrates that the image TV obtained with the proposed algorithm decreases faster than that obtained with the original TV algorithm. Moreover, the RMSEs of these two reconstructed images are calculated, which are 7.25 for new TV reconstruction, 8.75 for the original TV reconstruction, respectively. The smaller RMSE obtained with the new TV algorithm suggests that at the same iteration, the TV algorithm with the new designed TV-minimization direction can yield the image with better quality, and, as much, the efficiency of the new TV algorithm has been improved.

2.4 Implementation of TV algorithm to incorporate information of object support

The TV algorithm is a constrained optimization algorithm, which seeks to find the image with minimum TV under the data constraints and image positivity. Therefore, this algorithm can be extended to include additional constraints such as object support, finite lower-bound and upper-bound on image values. The incorporation of these physical constraints to the reconstruction algorithms is expected to improve the image quality. Compared to structure information within the object, information of the object support can be obtained relatively easily before the reconstruction, therefore

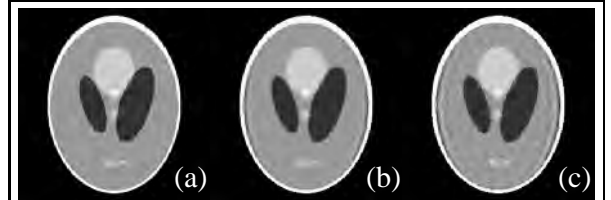


Figure 4: The true image (a) and images reconstructed by use of (b) proposed TV algorithm and (c) original TV algorithm after 200 iterations. Notice that these two images represents the intermediate images after certain iterations. The display gray scale is [0.9, 1.1].

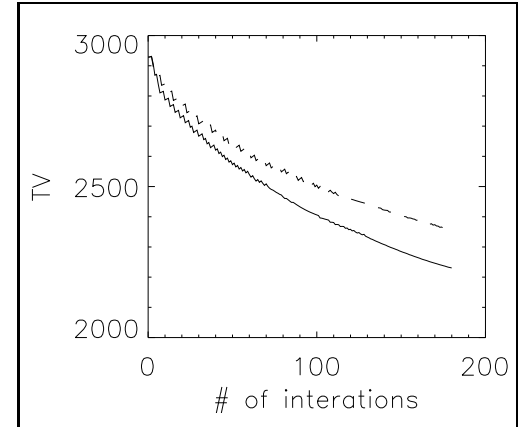


Figure 5: The TVs of reconstructed images for each iteration obtained by use of proposed TV algorithm (solid line) and the original TV algorithm (dashed line).

it can be regarded as a prior information in our reconstruction. In this work, we have developed an approach by incorporating the prior information into TV reconstruction. In the modified TV algorithm, only the image values within the support are updated while the image values outside the support is forced to be zero during each iteration.

We have conducted a study to investigate the performance of the TV algorithm with the object support. We have generated the projection data with 15 views over angular range 2π . The image of object support was considered as a prior information, which is already known. Two images are reconstructed by use of the TV with and without object support information, as shown in Fig. 6. It can be observed that reconstruction artifacts in the image obtained by use of TV algorithm with object support information has been removed.

2.5 Investigation of the effects of scanning parameters in breast tomosynthesis

Currently, breast tomosynthesis acquires data at about 12 to 20 projection views over a limited angular range around 20 to 50 degrees. Typically, a circular source trajectory is adopted for collection of cone-beam projections. It remains, however, largely unexplored as to what the optimal scanning configurations are in tomosynthesis imaging. In this work, we have conducted investigation on image reconstruction from data acquired at a small number of projection views over a limited angular range.

In the study, the source was moved along the circular trajectory. The projection data were generated from a numerical 3D breast phantom in Fig. 7a. The overall shape of the breast phantom was a truncated ellipsoid. The pectoralis muscle was represented by a rectangular slab. The ensemble of ductal structures was represented by a crescent shaped object. The mass lesions were in the fatty tissue, dense fibroglandular tissue, and the fatty tissue but with overlaying dense tissue, respectively. Attenuation coefficients for breast tissues were taken from Ref. [8] and from the online table of NIST x-ray data for 30 keV photons [9].

We first generated cone-beam data at 15, 20, 40, and 60 projection views over 2π . The reason for the angular range is 2π is that the study results would not be affected by the issue of the limited angular range. From these data sets, we have used the TV algorithm to reconstruct images. As an example, the images within 2D slices $x = 0$ and $y = 0$ reconstructed from 15 view data are displayed in Fig. 7. For comparison, we have conducted reconstructions by using POCS

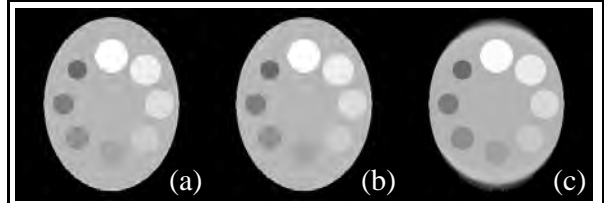


Figure 6: The true image (left) and images reconstructed by use of TV algorithm with the objection support (middle) and without the object support (right). The display gray scale is [0.5, 1.5].

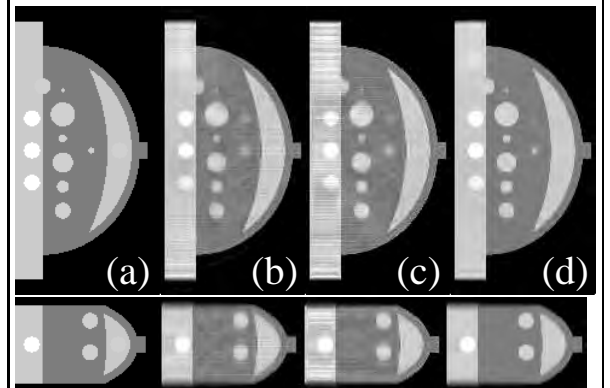


Figure 7: The true image (a) and the images reconstructed by use of (b) POCS, (c) EM, and (d) TV algorithms from data within angular ranges 2π for 2D slice $x = 0$ mm (top row) and $y = 0$ mm (bottom row). The display gray scale is [0.0, 0.5].

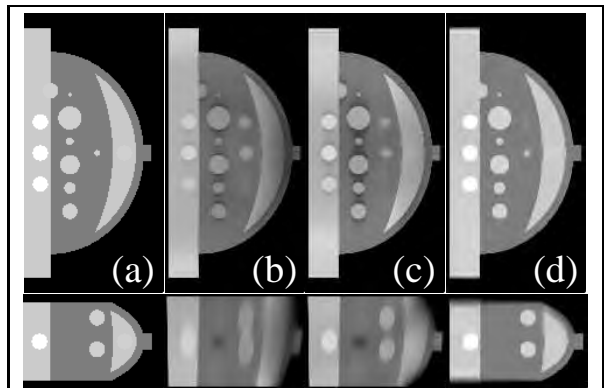


Figure 8: The true image (a) and images reconstructed from data within angular ranges (b) $\pi/4$, (c) $\pi/2$, and (d) π by use of TV algorithm for 2D slice $x = 0$ mm (top row) and $y = 0$ mm (bottom row). The display gray scale is [0.0, 0.5].

and EM algorithms as well. The evaluation indicates that the TV algorithm is more accurate than the EM and ART algorithms in reconstructing images from few-view data and that images obtained with TV algorithm contains less artifacts.

We also studied image reconstruction from data acquired over a limited angular range. Specifically, we have selected angular ranges of $\pi/4$, $\pi/2$, and π and collected data at 15, 20, 40, and 60 views over each of these angular ranges. From the collected data, we reconstructed images by use of TV, POCS, and EM algorithms. The images reconstructed from 15 projection views within the angular range $\pi/4$, $\pi/2$, and π by use of TV algorithm are displayed in Fig. 8. We can observe that, from few-few data over limited angular range, TV algorithm can yield images with useful information (the objects represent the breast lesions are visible). Moreover, these results suggest that, when the angular range increases, the distortion to the lesions is suppressed, as shown in the bottom row in Fig.8.

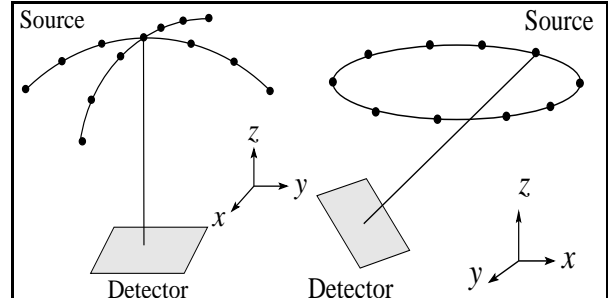


Figure 9: Illustration of two non-conventional scanning trajectories: double-arc (left) and oblique circle trajectories (right).

2.6 Investigation of the effect of source trajectories in tomosynthesis

In conventional tomosynthesis, the X-ray source generally is moved along a curve which is part of a circular trajectory. Because of the limitation of the angular coverage, it is always challenging to obtain the images of high quality from conventional tomosynthesis data. In this project, we have proposed a new imaging strategy by using different source trajectories for increasing data information in tomosynthesis, which may result in the improvement of the reconstructed image quality without increasing the imaging radiation dose [10]. In the investigation of this new imaging approach to tomosynthesis imaging, we have considered two new trajectories: one consists of two orthogonal arcs and the other is a circular trajectory above the scanned object, as shown in Fig. 9. These two trajectories are referred to as double-arc trajectory and oblique-circle trajectory, respectively. The source to rotation center is 7.0 cm. A flat-panel detector is placed perpendicular to the line connecting the source and the rotation center. The source-to-detector distance is 10.0 cm. We have generated analytically the data so that the data contain the continuous-to-discrete inconsistency. Images were reconstructed by use of TV algorithm from data acquired with these trajectories.

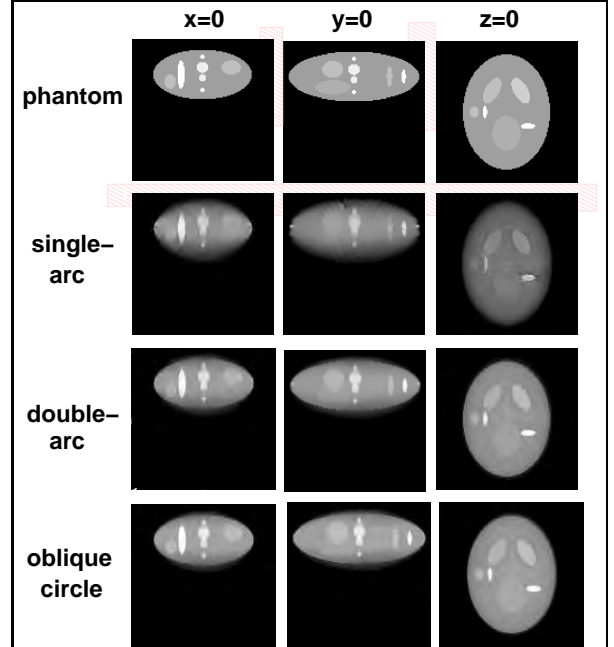


Figure 10: The true image (first row) and the images reconstructed from projection data acquired with the one-arc trajectory (second row), the double-arc trajectory (third row), and oblique circle trajectory (forth row). The first to third columns represent the 2D slices at $x = 0$ cm, $y = 0$ cm, and $z = 0$ cm, respectively. The display gray scale is [0, 2].

In an example study of a series of investigations, we have generated projection data from the phantom shown in the first row of Fig. 10 at 30 views uniformly distributed on the part of a circular trajectory used in breast tomosynthesis, whose angular range is 60° . In the Cartesian

coordinate system, the source trajectory can be written as $\vec{r}_0(\lambda) = (R\sin\lambda, 0, R\cos\lambda)$, where $\lambda \in [-\frac{\pi}{6}, \frac{\pi}{6}]$. From the data, we subsequently reconstructed images by using the TV algorithm, and we displayed in the second row of Fig. 10 the reconstructed images within planes specified by $x = 0$ cm, $y = 0$ cm, and $z = 0$ cm.

We also considered both double-arc trajectory and oblique-circle trajectory. In these two scanning configurations, the geometric parameters such as the source-to-rotation-center distance and detector-to-source distance were chosen to be identical to those in the above study for the planar circular trajectory. The two arcs in the double-arc source trajectory are written as $\vec{r}_0(\lambda) = (R\sin\lambda, 0, R\cos\lambda)$ for $\lambda \in [-\frac{\pi}{6}, \frac{\pi}{6}]$ and $\vec{r}_0(\lambda) = (0, R\sin(\lambda - \frac{\pi}{3}), R\cos(\lambda - \frac{\pi}{3}))$ for $\lambda \in [\frac{\pi}{6}, \frac{\pi}{2}]$, respectively. The oblique trajectory is written as $\vec{r}_0(\lambda) = (R\sin\alpha\sin\lambda, R\sin\alpha\cos\lambda, R\cos\alpha)$, and α is a parameter to describe the angle between z -axis and the ray connecting source and center of detector, which is 30^0 in our simulation study. Using these new trajectories, we generate analytically projection data from the same phantom over total 30 views of which are uniformly distributed on the trajectories. Therefore, the total imaging radiation doses in the studies involving the different trajectories are the same. From the generated data, we reconstructed images by use of the TV algorithm. In the third and forth rows of Fig. 10, we show the reconstructed images for these two trajectories within planes specified by $x = 0$ cm, $y = 0$ cm, and $z = 0.5$ cm, respectively. Comparison of the results in Fig. 10 suggests that with the same number of views (or, equivalently, the same amount of imaging dose), data acquired with our proposed trajectories tomosynthesis may contain more information than that acquired with the conventional tomosynthesis, leading to images with improved quality.

2.7 Investigation of the physical factors in tomosynthesis imaging

In realistic tomosynthesis imaging, a number of physical factors can significantly affect image quality, thereby lowering the detection rate of mass and microcalcification in breast. In this project, we have conducted investigation of the impact of the major physical factors, including data noise, scatter, non-linear partial volume, beam-hardening, and non-isotropic image spatial resolution. We summarize briefly our investigations below.

2.7.1 Noise properties

For tomosynthesis breast imaging that aims to have comparable radiation dosage with the standard mammography, the resulting data will contain substantial noise because the radiation exposure in one, or two, view in the standard mammography will be divided among many more projection views in tomosynthesis. In general, images generated from these tomosynthesis data will be noisier, leading to decreased detectability of microcalcification and low-contrast structures. The noise characteristics of the images, however, depend significantly on the reconstruction. A systematic noise analysis in the context of the tomosynthesis imaging is required.

In an attempt to separate the issues of few-view and limited angular range from data noise, we have first performed a thorough noise study for image reconstruction from projection data collected at a large number of views over 2π [11]. The result of this study provides a theoretical guidance to the investigation of the noise properties in tomosynthesis in which data are acquired at a small number of views over a limited angular range. In this study, we specifically focus on investigating how data noise are propagated into the reconstructed images. Both theoretical and numerical analyses were carried out, and the results indicate that variances of reconstructed images are spatially varying and that the levels of variances in different

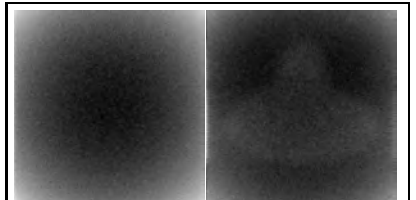


Figure 11: Empirical variance images obtained by use of analytical algorithm from fan-beam data containing Gaussian (left) and Poisson (right) noise.

regions are not affecting significantly each other, as shown in Fig. 11. Because the study was based upon a theoretical result, it was computationally possible to accomplish this initial study. On the other hand, noise studies involve the iterative algorithms such as the POCS, EM, and TV algorithms are much more demanding computationally.

2.7.2 X-ray scatter effect

For most existing reconstruction algorithms, the projection data are assumed to include only the x-ray transmission on a straight line connecting the source and detector element. However, a fraction of scattered x-ray intensity is also involved in realistic measurements. The inconsistencies introduced by the presence of scattered radiations in the projection data can lead to a decrease of low-contrast detectability, cupping artifacts and streak artifacts between dense objects. The effect of X-ray scatter poses a challenging problem in image reconstruction because the precise functional form of the distribution of the scattered radiations depends on the subject being scanned [12].

Taking advantage of the fact that the scattered X-ray intensity does not display significant high-resolution structures, we have proposed a convolution method in our study of scatter effect. Specifically, we have employed an existing scatter kernel to generate scatter components in tomosynthesis projection data [13]. In this model, critical physical parameters such as chest wall to nipple distance, breast thickness, and breast glandularity have been taken into account. We have generated and evaluated scatter components for projection angles: 0° , 6° , 12° , 18° , 24° , and 30° , which are typical angles in breast tomosynthesis. Based upon the convolution kernel and scatter components, we determined the scatter kernel for any projection angle by use of interpolation/extrapolation methods. Once we obtain these kernels for any angles, we then estimated the scatter-less projection data by deconvolving with the scatter kernel.

In an attempt to test the algorithm, we have applied this method to image reconstruction from data acquired with a real breast CT scanner, in which the source and the flat panel can be rotated around the patient's breast. For each scan, projection data were collected at typical 500 views uniformly distributed over 360° . From the full data set, we selected a subset of data at 20 views uniformly distributed over 72° for simulating tomosynthesis data. For each projection, the scatter-less projection were estimated from the original data by using the deconvolution method. From the corrected projection data we reconstructed the breast image by use of TV algorithm, the result is shown in Fig. 12a. For comparison, the image reconstruction from projection data with scatter was also performed, which is shown in Fig. 12b. It can be observed that the contrast in Fig. 12a is higher than that in 12b, which suggests that the compensation of scatter effect can improve the image quality in tomosynthesis imaging.

2.7.3 Non-linear partial volume effect

The ideal imaging model in tomosynthesis imaging assumes a point-like x-ray source and infinitely small detector elements. However, in realistic situation the source and detector elements both have finite sizes. As a result, the measured data reflect the averaged projections, which are equal to the negative exponentials of the path integrals, over the areas of the source spot and/or the detector bin. Obviously, this process for generating the averaged line integrals violates the ideal imaging model. In CT images, this non-linear averaging can result in conspicuous artifacts, such as streak artifacts that occur tangential to the structures with sharp attenuation transitions

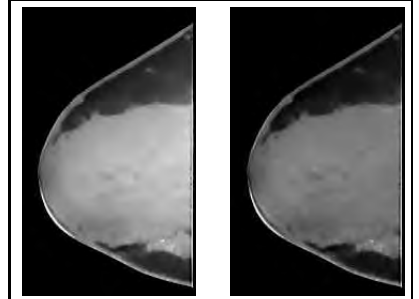


Figure 12: Images reconstructed from data with scatter correction (left) and without scatter correction (right). The display gray scale is [0.18, 0.29].

[14, 15]. Therefore in this study, we have investigated the non-linear partial volume effect in the tomosynthesis imaging, especially for the detection of breast microcalcifications.

In our simulation, the projection data were generated from a numerical 3D breast phantom with some microcalcifications, as shown in Fig. 13a. The smallest white points in the image represent the microcalcifications. We have generated tomosynthesis data at 30 projection views uniformly distributed over the angular range $\pi/4$. For each project view, we have sub-divided the x-ray source with finite size $0.75 \times 0.75 \text{ mm}^2$ and detector elements with finite size $0.75 \times 0.75 \text{ mm}^2$ into 5×5 sub-elements and computed the integrals over the 625 lines joining the sub-elements of the source and the sub-elements of the detector element. The projection data for each element were then obtained by taking the logarithm of the average of the negative exponentials of these line integrals. From the generated tomosynthesis data, the image was reconstructed by use of TV algorithm, which is displayed in Fig. 13b. Compared to the image reconstructed from the data without modeling non-linear partial volume effect, as shown in Fig. 13c, there is no obvious additional artifacts in the image obtained from data with non-linear partial volume effect. The result suggests that in tomosynthesis, the artifacts caused by non-linear partial volume effect is overwhelmed by the artifacts caused by other effects, such as limited scanning angular range.

2.7.4 Beam-hardening effect

Beam hardening is an unavoidable physical factor that needs to be accounted in x-ray systems. In most existing work on algorithm development for image reconstruction, the projection data are assumed to be the transmission of monochromatic x-rays through the subject. A realistic x-ray source, however, has a broad spectrum and is not monochromatic. Because the x-ray attenuation of an object depends on the photon energy, with lower-energy photons being attenuated more strongly, the mean energy of the x-ray beam will increase as it penetrates through, i.e., at exit the beam becomes harder than original. Consequently, the monochromatic imaging model is incorrect and this effect, without compensation, can cause artifacts such as cupping, streaking, and an overall shift of the CT number in the reconstructed images [16, 17].

We have investigated the beam hardening effect by considering a realistic x-ray spectrum in our simulations. In this study, the x-ray source was modeled a 28 kVp setting with a molybdenum anode. Based upon the spectrum of this source, we obtained the relative photon fluence at energy $E = 5, 10, 15, 20, 25, 30 \text{ keV}$, respectively. The attenuation coefficient within a numerical breast phantom (Fig. 4a) is designed as a function of the x-ray energy, which were taken from Ref. [8]. Based upon the known relative photon fluence, we have accordingly weighted the exponentials of line integrals for each individual energy, then took the logarithm of the sum of the weighted exponentials to form the final projection data for the polychromatic source. With this method, we generate the tomosynthesis data by using the scanning configuration described in Sec. 2.7.3. The image was reconstructed by use of the TV algorithm, which is shown in Fig. 14c. For the comparison the image reconstruction for monochromatic x-ray

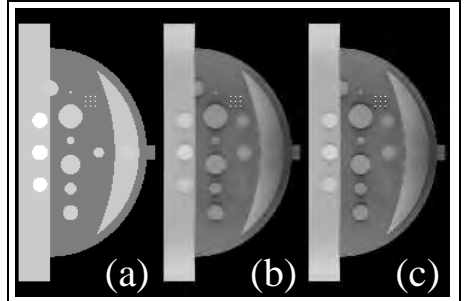


Figure 13: Breast phantom image with some microcalcifications (a) and images reconstructed from data acquired with modeling non-linear partial volume effect (b) and data acquired without modeling non-linear partial volume effect (c). The display gray scale is [0.0, 0.5].

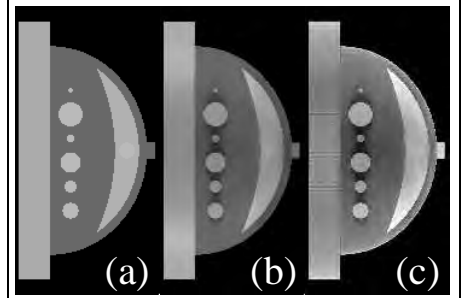


Figure 14: Breast phantom image for 30keV energy (a) and the images reconstructed from data acquired with 30keV monochromatic x-ray source (b) and realistic x-ray source data (c). The display gray scales for figures (a) and (b) are [0.1, 0.5], while the display gray scale for figure (c) is [0.2, 1.0] because of the CT number shift.

was also performed, the result is displayed in Fig. 14b. One can find the severe artifacts, such as cupping and CT number shift, in the image reconstructed from data simulated by using polychromatic x-ray. Therefore, the correction of beam-hardening in tomosynthesis imaging may be necessary, which is now under investigation.

2.7.5 Non-isotropic resolution

In current breast tomosynthesis, the spatial resolution within a transverse plane is much finer than that along the longitudinal direction, and image representation with non-isotropic image size is used in iterative algorithms for reducing computational time. Such an image representation can lead to significant artifacts in iterative reconstruction. We have been investigating the effect of non-isotropic image representation on iterative reconstruction accuracy of breast tomosynthesis images [18]. We have reconstructed images by use of POCS, EM, and TV algorithms for image representations with different ratios of the in-plane and longitudinal pixel size, which are shown in Fig. 15. Our results demonstrate that non-isotropic image representation can lead to image artifacts in reconstructed images. The appearance and severity of the artifacts depend not only upon the ratio between the in-plane and longitudinal resolution but also upon the iterative algorithms. The TV algorithm seems to be less susceptible to the effect than the POCS and EM algorithms.

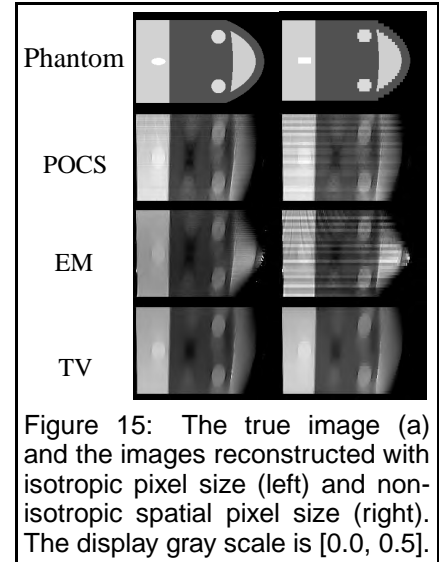


Figure 15: The true image (a) and the images reconstructed with isotropic pixel size (left) and non-isotropic spatial pixel size (right). The display gray scale is [0.0, 0.5].

KEY RESEARCH ACCOMPLISHMENTS

- We have modified the TV algorithm tailored to breast tomosynthesis.
- We have implemented the existing EM and POCS algorithms for comparison with our TV algorithm.
- We have determined the upper bound on the performance of TV algorithm for image reconstruction from discrete tomosynthesis data.
- We have implemented a projection program to compute both discrete-to-discrete projection and continuous-to-discrete projection data.
- We have conducted an investigation on the effect of different constraint parameter ϵ for the data containing continuous-to-discrete inconsistency.
- We have modified TV algorithm for improvement of efficiency by using different relaxation parameter.
- We have proposed an approach for efficiently minimizing TV in the reconstruction.
- We have implemented the TV algorithm to incorporate the object support information to improve tomosynthesis reconstruction.
- We have investigated the effects of scanning parameters in breast tomosynthesis imaging by using different numbers of views over different angular ranges.
- We have conducted a preliminary investigation of the different source trajectories in tomosynthesis breast imaging for improving image quality.
- We have performed a preliminary investigation of the data noise.
- We have generated the scatter component in breast tomosynthesis by involving the scatter-free projection data with the scatter kernel.
- We have applied a deconvolution method to real breast data to improve the image reconstruction.
- We have performed a preliminary investigation on the effect of the non-linear partial volume in breast tomosynthesis.
- We have conducted a preliminary investigation on the effect of beam-hardening in breast tomosynthesis.
- We have performed a preliminary investigation on the effect of the non-isotropic spatial resolution in breast tomosynthesis.

REPORTABLE OUTCOMES

Peer-reviewed Journal Articles

1. **D. Xia**, L. Yu, E. Y. Sidky, Y. Zou, N. Zuo, and X. Pan: Noise properties of chord-image reconstruction, *IEEE Transaction on Medical Imaging* **26**, pp. 1328-1344, 2007.

Conference Proceeding Articles

1. **D. Xia**, E. Y. Sidky, L. Yu, and X. Pan: Noise properties in helical cone-beam CT images, *IEEE Medical Image Conference Record*, M14-420, 2006.
2. **D. Xia**, S. Cho, X. Pan: Image noise properties in circular sinusoid cone-beam CT, *IEEE Medical Image Conference Record*, M13-285, 2007.
3. **D. Xia**, J. Bian, E. Y. Sidky, C. A. Pelizzari, and X. Pan: Tomosynthesis with Source Positions Distributed over a Surface, *Proc. SPIE*, Vol. 6913, pp. 69132A, 2008.
4. J Bian, NJ Packard, K Yang, **D Xia**, JM Boone, X Pan: Non-circular scans and image reconstruction for breast CT, *Proc. SPIE*, vol. 6913, pp. 69134G, 2008.

Conference Presentations and Abstracts

1. **D. Xia**, J. Bian, E. Sidky, and X. Pan: Image representation with non-isotropic spatial resolution on iterative reconstruction accuracy in breast tomosynthesis, *RSNA scientific assembly and annual meeting program*, SSC13-01, 2007.

CONCLUSIONS

The recipient of the Predoctoral Traineeship Award has finished the required courses towards his Ph.D. degree. These trainings have proved useful for the recipient to achieve the proposed research goals.

During the research, we have implemented and investigated the TV algorithm for image reconstruction in breast tomosynthesis. We have conducted numerical studies to investigate the image reconstruction from ideal projection data by use of the TV algorithm and the existing EM and TV algorithms, which give the upper bound on the performance of these reconstruction algorithms. Our results suggest that, in general, the TV algorithm provide tomosynthesis images with quality higher than EM and TV algorithms in terms of the metrics such as root-mean-square error. We have performed the numerical studies to investigate the image reconstruction for the data containing continuous-to-discrete inconsistency, which happens in real scans. In this study, the images were reconstructed by use of the TV algorithm with different constraint parameter ϵ . The relationship between the image quality, in terms of the metrics such as RMSE, and the constraint parameter ϵ has been identified. Base upon the original TV algorithm, we have further modified TV algorithm to improve the performance of image reconstruction, including improving the TV algorithm efficiency and incorporating the information of object support. The TV reconstruction with information of object support yields the better image than does the original TV.

In this project, we have also investigation of different scanning configurations in breast tomosynthesis. The tomosynthesis data were collected from different angular ranges at different numbers of views. Our results suggest that when the angular range decreases, image quality obtained with these algorithms decreases. Moreover, we have proposed a new imaging strategy by using trajectories for increasing data information in tomosynthesis. The results obtained with the new scanning trajectories demonstrate that with the same number of views (or, equivalently, the same amount of imaging dose), data acquired with the proposed non-planar trajectory tomosynthesis may contain more information than that acquired with the conventional tomosynthesis, leading to images with improved quality.

Furthermore, we have also performed the studies to model some critical physical factors in breast tomosynthesis, including data noise, scatter, non-linear partial volume, beam hardening and non-isotropic spatial resolution on tomosynthesis images. The effect of these physical factors has been investigated. Our results demonstrate that noise, scatter, beam hardening can affect the image quality obtained from the tomosynthesis data, which should be compensated during the reconstruction process, while the artifacts caused by the non-linear partial volume effect in breast tomosynthesis is negligible. Moreover, a deconvolution method for scatter correction has been applied for real breast data, and has been demonstrated to be helpful for improving the image quality.

Overall, we have achieved the goals for this project and laid the foundation for our continuation of breast cancer research. The future research will continue on the evaluation and correction of physical factors such as beam-hardening. Moreover, the developed TV algorithm will be applied to real data of breasts for additional evaluation of the scanning configurations and reconstruction algorithms. For this, real-patient data base will be needed for testing and assessing the reconstruction algorithms and imaging parameters.

REFERENCES

1. R. E. Bird, T. W. Wallace, and B. C. Yankaskas: Analysis of cancers missed at screening mammography, *Radiology*, vol. 184, pp. 613-617, 1992.
2. J. T. Dobbins III and D. J. Godfrey: Digital x-ray tomosynthesis: current state of the TV and clinical potential, *Phys. Med. Biol.*, Vol. 48, pp. R65-R106, 2003.
3. M. Bissonnette, M. Hansroul, E. Masson, S. Savard, S. Cadieux, P. Warmoes, D. Gravel, J. Agopyan, B. Polischuk, W. Haerer, T. Mertelmeier, J. Y. Lo, Y. Chen, J. T. Dobbins III, J. L. Jesneck, and S. Singh: Digital breast tomosynthesis using an amorphous selenium flat panel detector, *Proc. SPIE*, Vol. 5745, pp. 529, 2005.
4. L. T. Niklason, B. T. Christian, D. B. Kopans, D. E. Vastleberry, B. H. Opsahl-Ong, C. E. Landberg, P. J. Slanetz, A. A. Giardino, R. Moore, D. Albagli, M. C. Fejule, P. F. Fitzgerald, D. F. Fobare, B. W. Giambattista, R. F. Kwasnick, J. Liu, S. J. Lubowski, G. E. Possin, J. F. Richotte, C. Y. Wei, and R. F. Wirth: Digital tomosynthesis in breast imaging. *Radiology*, Vol. 205, pp. 399-406, 1997.
5. E. Sidky, C.-M. Kao, and X. Pan: Accurate image reconstruction from few-views and limited-angle data in divergent-beam CT, *J. X-ray Sci. Tech.*, Vol. 14, pp. 119-139, 2006.
6. G. T. Herman: *Image Reconstruction from Projections*, Academic Press, New York, pp. 161-179, 1980.
7. K. Lange, and R. Carson: EM reconstruction algorithms for emission and transmission tomography, *J. Comput. Assist. Tomogr.*, Vol. 8, pp. 306-316, 1984.
8. I. C. Johns and M. J. Yaffe: X-ray characterisation of normal and neoplastic breast tissues, *Phys. Med. Biol.*, 32:675-695, 1987.
9. J. H. Hubbell and S. M. Seltzer: Tables of X-ray mass attenuation coefficients and mass energy-absorption coefficients from 1 keV to 20 MeV for elements Z=1 to 92 and 48 additional substances of dosimetric interest, <http://www.physics.nist.gov/PhysRefData/XrayMass-Coef/cover.html>.
10. D. Xia, J. Bian, E. Y. Sidky, C. A. Pelizzari, and X. Pan: Tomosynthesis with source positions distributed over a surface, *Proc. SPIE*, Vol. 6913, pp. 69132A, 2008.
11. D. Xia, L. Yu, E. Y. Sidky, Y. Zou, N. Zuo, and X. Pan: Noise properties of chord-image reconstruction, *IEEE Transaction on Medical Imaging* 26, pp. 1328-1344, 2007.
12. J. H. Siewersen and D. A. Jaffray: Cone-beam computed tomography with a flat-panel imager: Magnitude and effects of x-ray scatter, *Med. Phys.* Vol. 31, pp. 1195-1202, 2004.
13. I. Sechopoulos, S. Suryanarayanan, S. Vedantham, C. J. D'Orsi, and A. Karelasa: Scatter radiation in digital tomosynthesis of the breast, *Med. Phys.* Vol. 34, pp. 564-576, 2007.
14. Zou Y, Sidky E, and Pan X : Partial volume and aliasing artefacts in helical cone-beam CT, *Phys. Med. Biol.* 49, 2365-2375, 2004.
15. Glover GH and Pelc NJ : Nonlinear partial volume artifacts in x-ray computed tomography, *Med. Phys.* 7, 238-248, 1980.
16. Hsieh J, Molthen RC, Dawson CA and Johnson RH : An iterative approach to the beam hardening correction in cone beam CT, *Med. Phys.* 27, 23-29, 2000.

17. Sidky E, Zou Y, and Pan X : Impact of polychromatic x-ray sources on helical, cone-beam computed tomography and dual-energy methods. *Phys. Med. Biol.* 49, 2293-2303, 2004.
18. D. Xia, J. Bian, E. Sidky, and X. Pan: Image representation with non-isotropic spatial resolution on iterative reconstruction accuracy in breast tomosynthesis, RSNA scientific assembly and annual meeting program, SSC13-01, 2007.

APPENDICES

- Appendix A: **D. Xia**, L. Yu, E. Y. Sidky, Y. Zou, N. Zuo, and X. Pan: Noise properties of chord-image reconstruction, *IEEE Transaction on Medical Imaging* **26**, pp. 1328-1344, 2007.
- Appendix B: **D. Xia**, J. Bian, E. Sidky, and X. Pan: Image representation with non-isotropic spatial resolution on iterative reconstruction accuracy in breast tomosynthesis, RSNA scientific assembly and annual meeting program, SSC13-01, 2007.
- Appendix C: **D. Xia**, S. Cho, X. Pan: Image noise properties in circular sinusoid cone-beam CT, IEEE Medical Image Conference Record, M13-285, 2007.
- Appendix D: **D. Xia**, Junguo Bian, Emil Y. Sidky, Charles A. Pelizzari, and Xiaochuan Pan: Tomosynthesis with source positions distributed over a surface, Proc. SPIE, Vol. 6913, pp. 69132A, 2008.
- Appendix E: J Bian, NJ Packard, K Yang, **D Xia**, JM Boone, X Pan: Non-circular scans and image reconstruction for breast CT, Proc. SPIE, vol. 6913, pp. 69134G, 2008.

Noise Properties of Chord-Image Reconstruction

Dan Xia, *Student Member, IEEE*, Lifeng Yu, Emil Y. Sidky, Yu Zou, Nianming Zuo, and Xiaochuan Pan*, *Fellow, IEEE*

Abstract—Recently, there has been much progress in algorithm development for image reconstruction in cone-beam computed tomography (CT). Current algorithms, including the chord-based algorithms, now accept minimal data sets for obtaining images on volume regions-of-interest (ROIs) thereby potentially allowing for reduction of X-ray dose in diagnostic CT. As these developments are relatively new, little effort has been directed at investigating the response of the resulting algorithm implementations to physical factors such as data noise. In this paper, we perform an investigation on the noise properties of ROI images reconstructed by using chord-based algorithms for different scanning configurations. We find that, for the cases under study, the chord-based algorithms yield images with comparable quality. Additionally, it is observed that, in many situations, large data sets contain extraneous data that may not reduce the ROI-image variances.

Index Terms—Chord, computed tomography (CT), cone-beam CT, noise, reconstruction.

I. INTRODUCTION

IN recent years, exact algorithms have been developed for reconstructing images [1] and for reconstructing images on “ π -lines” [2]–[4] from helical cone-beam data. Since 2005, papers have been published on algorithm development for reconstructing images on chords for general trajectories [5]–[8]. Some of these algorithms can reconstruct images within 3-D regions of interest (ROIs) from cone-beam data containing both longitudinal and transverse truncations. The introduction of the M -line concept and reconstruction [5], [9] provides additional flexibility for covering volume ROIs.

As these algorithm developments are relatively recent, little effort has been directed at investigating their noise properties. With the algorithm development for ROI-image reconstruction, it has been tacitly assumed that the reduction in necessary scanning angle and in projection data may lead to ROI images from less radiation exposure. This conclusion may, however, depend

Manuscript received May 8, 2006; revised March 26, 2007. This work was supported by the National Institutes of Health under Grant EB00225 and Grant EB02765. The work of D. Xia was supported in part by Department of Defense (DoD) under Predoctoral Training Grant BC051553. The work of E. Y. Sidky was supported by the National Institutes of Health under Grant K01 EB003913. The work of N. Zuo was supported in part by the National Science Foundation of China under Grant 60328101. The contents are solely the responsibility of the authors and do not necessarily represent the official views of the National Institutes of Health. Asterisk indicates corresponding author.

D. Xia, L. Yu, E. Y. Sidky, and Y. Zou are with the Department of Radiology, The University of Chicago, Chicago, IL 60637 USA.

N. Zuo is with the National Laboratory of Pattern Recognition, Institute of Automation, Chinese Academy of Sciences, 100080 Beijing, China..

*X. Pan is with the Department of Radiology, The University of Chicago, Chicago, IL 60637 USA.

Color versions of some of the figures in this paper are available online at <http://ieeexplore.ieee.org>.

Digital Object Identifier 10.1109/TMI.2007.898567

on the noise properties of reconstruction algorithms. If ROI reconstruction from the minimal (or reduced) data set leads to noisier ROI images than reconstruction of the same ROI from a larger data set, it may be necessary to increase the X-ray source intensity for the ROI data set to attain the same image quality as those reconstructed from larger data sets. Such an increase can offset the fact that reduced or minimum projection data are needed for ROI reconstruction.

The focus of this paper is to investigate the noise properties of image reconstruction from minimal data set and large data set by use of chord-based algorithms. We demonstrate that the minimal data set can indeed lead to actual reduction of radiation exposure for attaining comparable image quality, defined in terms of image variance, as that obtained with a larger data set. In Section II, we briefly summarize the chord-based reconstruction algorithms: backprojection filtration (BPF) [2], [6], minimum data filtered backprojection (MDFBP) [4], [6], and filtered backprojection (FBP) [6], [10] algorithms. In Section III, we perform analysis and empirical studies on noise properties of images reconstructed from parallel-beam, fan-beam, and cone-beam data. Finally, a discussion is given in Section IV.

II. CHORD-BASED RECONSTRUCTION ALGORITHMS

We consider a continuous source trajectory specified by $\vec{r}_0(s) = (x(s), y(s), z(s))$, where $x(s)$, $y(s)$, and $z(s)$ denote the x –, y –, and z – components of $\vec{r}_0(s)$ in the fixed-coordinate system, and s is a curve parameter indicating the position of the X-ray source on the trajectory. The projection data of the object function $f(\vec{r})$ can be mathematically expressed as

$$D(\vec{r}_0(s), \hat{\beta}) = \int_0^\infty dt f(\vec{r}_0(s) + t\hat{\beta}) \quad (1)$$

where the unit vector $\hat{\beta}$ denotes the direction of a specific X-ray passing through the point \vec{r} . We also introduce two additional coordinate systems $\{u, v, w\}$ and $\{u_d, v_d\}$ to describe the geometry in a general scan. They are fixed on the rotating source point and the cone-beam projection of the source point, respectively, which are referred to as the rotation-coordinate and detector-coordinate systems. Let $\hat{e}_u(s)$, $\hat{e}_v(s)$, and $\hat{e}_w(s)$ denote the orthogonal unit vectors of the rotation-coordinate system. The rotation-coordinate system can be chosen such that $\hat{e}_u(s)$ and $\hat{e}_w(s)$ are within the x – y plane and $\hat{e}_v(s)$ is parallel to the z axis. One can also choose the “well oriented” coordinate system as the rotation-coordinate system [5], in which unit vector $\hat{e}_u(s)$ is parallel to and unit vectors $\hat{e}_v(s)$ and $\hat{e}_w(s)$

are perpendicular to the direction of $(d\vec{r}_0(s)/ds)$. We assume that a detector plane is placed at a distance S from the source point and orients along $\hat{e}_w(s)$. The detector-coordinate system $\{u_d, v_d\}$ is the cone-beam projection of the 2-D coordinate system $\{u, v\}$ onto the detector plane, and the u_d and v_d axis are along $\hat{e}_u(s)$ and $\hat{e}_v(s)$, respectively. In this situation, we also use $P(u_d, v_d, s)$ to denote the cone-beam projection, thus $D(\vec{r}_0(s), \hat{\beta}) = P(u_d, v_d, s)$, when

$$\hat{\beta} = \frac{1}{A(u_d, v_d)} [u_d \hat{e}_u(s) + v_d \hat{e}_v(s) - S \hat{e}_w(s)]$$

and $A(u_d, v_d) = \sqrt{u_d^2 + v_d^2 + S^2}$. (2)

In a 2-D case, it can be observed that $v_d = 0$. For notational convenience, we use $A(u_d)$ and $P(u_d, s)$ to denote $A(u_d, 0)$ and $P(u_d, 0, s)$, respectively.

A *chord* is a line segment connecting two points $\vec{r}_0(s_a)$ and $\vec{r}_0(s_b)$ on the trajectory. Any point \vec{r} on the chord can be expressed as

$$\vec{r} = \frac{\vec{r}_0(s_a) + \vec{r}_0(s_b)}{2} + x_c \hat{e}_c, \quad x_c \in [-l, l] \quad (3)$$

where $\hat{e}_c = (\vec{r}_0(s_b) - \vec{r}_0(s_a)) / |\vec{r}_0(s_b) - \vec{r}_0(s_a)|$ denotes the direction of the chord, and $l = (1/2)|\vec{r}_0(s_b) - \vec{r}_0(s_a)|$ is one half of the chord length. For a helical trajectory, the curve parameter s is linearly related to the rotation angle λ , and in the current work, we select $s = \lambda$. When s_a and s_b are within one turn, the chord becomes the conventional π -line segment [2], [11], [12]. The intersection between a chord and the object is referred to as a *support segment*. Let x_{c1} and x_{c2} represent the end points of a support segment. Because the trajectory under consideration never intersects the object, we have $[x_{c1}, x_{c2}] \subset [-l, l]$. Therefore, one can use (x_c, s_a, s_b) and $f_c(x_c, s_a, s_b)$ to denote a point and the corresponding image on the chord. We have previously developed three algorithms, which are referred to as the BPF [2], [6], [10], MDFBP [4], [6], and FBP [6], [10] algorithms, respectively, for exact image reconstruction on a chord of a general trajectory.

A. BPF Algorithm

The BPF algorithm [2], [6] reconstructs the image on a chord specified by s_a and s_b as

$$f_c(x_c, s_a, s_b) = \hat{f}(x_c, s_a, s_b) + \frac{1}{2\pi} \frac{P(u_{d0}, v_{d0}, s_a)}{b(x_c)} \times \left[\frac{\sqrt{(l-x_B)(l-x_A)}}{l-x_c} + \frac{\sqrt{(l+x_A)(l+x_B)}}{l+x_c} \right] \quad (4)$$

where $x_c \in [x_A, x_B]$, and parameters x_A and x_B are two points on the chord satisfying $[x_{c1}, x_{c2}] \subset [x_A, x_B] \subset [-l, l]$. The function $b(x_c)$ is defined as $b(x_c) = \sqrt{(x_B - x_c)(x_c - x_A)}$, and $P(u_{d0}, v_{d0}, s_a)$ denotes the projection along the chord

specified by s_a and s_b . The filtered image $\hat{f}(x_c, s_a, s_b)$ is given by

$$\hat{f}(x_c, s_a, s_b) = \frac{1}{2\pi^2} \frac{1}{b(x_c)} \int_{\mathbf{R}} \frac{dx'_c}{x_c - x'_c} b(x'_c) g(x'_c, s_a, s_b) \quad (5)$$

where the backprojection image on the chord can be written as

$$g(x'_c, s_a, s_b) = \Pi_c(x'_c) \int_{s_a}^{s_b} ds \frac{\text{sgn}(-\hat{\beta} \cdot \hat{e}_w)}{|\vec{r}' - \vec{r}_0(s)|^2} \times \left\{ -\frac{d\vec{r}_0(s)}{ds} \cdot \hat{\beta} P(u_d, v_d, s) \right. \\ + \left[\frac{d\vec{r}_0(s)}{ds} \cdot \hat{e}_u(s) + \frac{u_d}{S(s)} \frac{d\vec{r}_0(s)}{ds} \cdot \hat{e}_w(s) \right] \times A(u_d, v_d) \frac{\partial P(u_d, v_d, s)}{\partial u_d} \\ + \left[\frac{d\vec{r}_0(s)}{ds} \cdot \hat{e}_v(s) + \frac{v_d}{S(s)} \frac{d\vec{r}_0(s)}{ds} \cdot \hat{e}_w(s) \right] \times A(u_d, v_d) \frac{\partial P(u_d, v_d, s)}{\partial v_d} \left. \right\} \quad (6)$$

and the rect function $\Pi_c(x'_c) = 1$ if $x'_c \in [x_A, x_B]$ and zero otherwise. It can be observed in (4) that the chord image can be obtained exactly from knowledge of the backprojection image $g(x'_c, s_a, s_b)$ for $x'_c \in [x_A, x_B]$, which we refer to as the *reconstruction segment* because it determines the actual reconstruction interval on the chord. In particular, because the reconstruction segment $[x_A, x_B]$ can be chosen as small as the support segment $[x_{c1}, x_{c2}]$, the chord image can be reconstructed from knowledge of $g(x'_c, s_a, s_b)$ only on the support segment. This interesting property of the Hilbert transform forms the basis for exact image reconstruction on a chord from projections containing longitudinal or transverse truncations [13].

B. MDFBP Algorithm

The BPF algorithm reconstructs the chord image by performing a 1-D filtration [i.e., the integration over x'_c in (4)] of the backprojection image [i.e., the integration over s in (6)]. On the other hand, the MDFBP algorithm [4], [6] reconstructs the chord image by performing a 1-D data filtration (i.e., the integration over u'_c) prior to their backprojection (i.e., the integration over s) onto the chord

$$f_c(x_c, s_a, s_b) = \frac{1}{2\pi^2} \frac{1}{b(x_c)} \int_{s_a}^{s_b} ds [w_2(1 - u_c) + w_1 u_c] \int_{\mathbf{R}} \frac{du'_c}{u_c - u'_c} P_{\Pi} \\ + \frac{1}{2\pi} \frac{P(u_{d0}, v_{d0}, s_a)}{b(x_c)} \times \left[\frac{\sqrt{(l-x_B)(l-x_A)}}{l-x_c} + \frac{\sqrt{(l+x_A)(l+x_B)}}{l+x_c} \right] \quad (7)$$

where the modified data function is given by

$$P_{\Pi} = \Pi_c(x'_c) \frac{b(x'_c)}{w_2(1 - u'_c) + w_1 u'_c} \frac{\text{sgn}(-\hat{\beta} \cdot \hat{e}_w)}{|\vec{r} - \vec{r}_0(s)|^2} \\ \times \left\{ -\frac{d\vec{r}_0(s)}{ds} \cdot \hat{\beta} P(u_d, v_d, s) \right. \\ + \left[\frac{d\vec{r}_0(s)}{ds} \cdot \hat{e}_u(s) + \frac{u_d}{S(s)} \frac{d\vec{r}_0(s)}{ds} \cdot \hat{e}_w(s) \right] \\ \times A(u_d, v_d) \frac{\partial P(u_d, v_d, s)}{\partial u_d} \\ + \left[\frac{d\vec{r}_0(s)}{ds} \cdot \hat{e}_v(s) + \frac{v_d}{S(s)} \frac{d\vec{r}_0(s)}{ds} \cdot \hat{e}_w(s) \right] \\ \left. \times A(u_d, v_d) \frac{\partial P(u_d, v_d, s)}{\partial v_d} \right\}$$

$w_1 = -[\vec{r}_0(s_a) - \vec{r}_0(s)] \cdot \hat{e}_w$, and $w_2 = -[\vec{r}_0(s_b) - \vec{r}_0(s)] \cdot \hat{e}_w$. For a source position s , the variables u_c and u'_c denote the cone-beam projections of x_c and x'_c onto the detector and can be obtained, respectively, by replacing x with x_c and x'_c in

$$u = \frac{w_2(x + l)}{w_1(l - x) + w_2(x + l)}. \quad (8)$$

The rect function $\Pi_c(x'_c)$ in (8) indicates that the MDFBP algorithm can reconstruct a chord image from knowledge of data only on the cone-beam projection of the reconstruction segment $[x_A, x_B]$, which can be as small as the support segment. Therefore, similar to the BPF algorithm, the MDFBP algorithm can also reconstruct a chord image from data containing truncations [4], [6].

C. FBP Algorithm

The chord-based FBP algorithm [6], [10] can be expressed as

$$f_c(x_c, s_a, s_b) = \frac{1}{2\pi^2} \int_{s_a}^{s_b} ds \frac{A}{|\vec{r} - \vec{r}_0(s)|} \\ \times \int_{-\infty}^{\infty} \frac{du'_c}{u_c - u'_c} \frac{1}{|\vec{r} - \vec{r}_0(s)|} \frac{\partial}{\partial q} D(\vec{r}_0(q), \hat{\beta}) \Big|_{q=s} \quad (9)$$

where u_c indicates the cone-beam projection of x_c onto the detector and is determined by using x_c to replace x in (8), and A denotes the distance from the source point $\vec{r}_0(s)$ to a point on the detector at which the ray connecting \vec{r} and $\vec{r}_0(s)$ intersects the detector. As the filtering (i.e., the integration over u'_c) is carried out over the projection of the straight line containing the chord, similar to other existing FBP-based algorithms, the chord-based FBP algorithm cannot exactly reconstruct ROI images from data containing transverse truncations.

D. Data-Sufficiency Conditions

As shown in (9), a data-sufficiency condition for the FBP algorithm is: 1) data are available over the trajectory segment $s \in [s_a, s_b]$ and 2) for each s , data on the cone-beam projection of the chord are nontruncated. This condition is similar to that for other FBP-based algorithms [1], [9], [14], [15], [16]. From (4) and (7), a data-sufficiency condition for the chord-based

BPF and MDFBP algorithms is: 1) data are collected over the trajectory segment $[s_a, s_b]$ and 2) at each s , data only on the cone-beam projection of the reconstruction segment $[x_A, x_B]$ on the chord are available. It follows that, because the reconstruction segment $[x_A, x_B]$ can be chosen as small as the support segment $[x_{c1}, x_{c2}]$, the BPF and MDFBP algorithms require, at each s , data only on the cone-beam projection of the support segment $[x_{c1}, x_{c2}]$ (instead of the entire chord-line as the chord-based FBP algorithm requires). Different selections of the reconstruction segment $[x_A, x_B]$ imply that different amounts of data at each s can be used for reconstructing the chord image. Under the ideal continuous conditions, different selections of $[x_A, x_B]$ yield identical chord images. However, when data contain noise and other inconsistencies, and when different selections of $[x_A, x_B]$ are used, the BPF and MDFBP algorithms in their discrete forms may yield different chord images. This is an issue that will be investigated in the following.

III. NOISE PROPERTIES OF CHORD-BASED IMAGE RECONSTRUCTION

The BPF, MDFBP, and FBP algorithms described above can be applied to reconstructing chord images from parallel-, fan-, and cone-beam data [17]. Algorithms analogous to the BPF algorithm that are capable of reconstructing 2-D ROI images from truncation data have also previously been proposed [8], [13], [18]. We study the noise properties of chord-based reconstruction by use of these algorithms in their discrete forms. As mentioned above, the BPF and MDFBP algorithms can reconstruct the image on the reconstruction segment $[x_A, x_B]$ as long as it covers the support segment $[x_{c1}, x_{c2}]$. We analyze image-noise properties on reconstruction segments of different lengths.

A. Analysis of Image-Noise Properties

The chord-based algorithms invoke three major mathematical operations: differentiation, backprojection, and filtration. To a large extent, the BPF, MDFBP, and FBP algorithms differ in the orders of invoking these operations. Below, we focus on investigating the noise properties of differentiation, backprojection, and filtration in the BPF algorithm. The approach taken in the investigation is readily applicable to analyzing the noise properties of the MDFBP and FBP algorithms. In the presence of data noise, the measured projection $\mathbf{D}(\vec{r}_0(s), \hat{\beta})$ should be interpreted as a stochastic process. (Throughout the paper, we use boldface and normal letters to denote a stochastic process and its mean, respectively.) Because the backprojection $\mathbf{g}(x_c, s_a, s_b)$ and the final image $\mathbf{f}_c(x_c, s_a, s_b)$ on a chord are computed from $\mathbf{D}(\vec{r}_0(s), \hat{\beta})$, they should also be considered as stochastic processes. We focus in this section on investigating the chord-image variance $\mathbf{f}_c(x_c, s_a, s_b)$ by the investigation of noise propagation through each step involved in the BPF reconstruction algorithm.

1) *Noise Properties of Differentiation/Backprojection for Parallel-Beam Data:* Let $\mathbf{P}(u_d, s)$ denote the parallel-beam projection on detector bin u_d acquired at view s . We assume the covariance of the projection data $\mathbf{P}(u_d, s)$ to be uncorrelated, i.e.,

$$\text{Cov}\{\mathbf{P}(u_d, s), \mathbf{P}(u'_d, s')\} = \sigma^2(u_d, s)\delta(u_d - u'_d)\delta(s - s') \quad (10)$$

where $\sigma^2(u_d, s)$ denotes the variance of the projection data. The backprojection image on the chord is given by [13]

$$\mathbf{g}(x_c, s_a, s_b) = \int_{-\frac{\pi}{2}}^{\frac{\pi}{2}} ds \frac{\partial}{\partial u_d} \mathbf{P}(u_d, s) \quad (11)$$

where $u_d = \vec{r} \cdot \hat{e}_u(s)$. The final image variances on a chord depend upon the covariance of the backprojection image, which, using (11), can be written as

$$\begin{aligned} \text{Cov} \{ \mathbf{g}(x_c, s_a, s_b), \mathbf{g}(x'_c, s_a, s_b) \} \\ = \int_{-\frac{\pi}{2}}^{\frac{\pi}{2}} ds \int_{-\frac{\pi}{2}}^{\frac{\pi}{2}} ds' \text{Cov} \left\{ \frac{\partial}{\partial u_d} \mathbf{P}(u_d, s), \frac{\partial}{\partial u'_d} \mathbf{P}(u'_d, s') \right\}. \end{aligned} \quad (12)$$

The evaluation of the backprojection-image covariance involves the data-derivative covariance, which can be conveniently written as

$$\begin{aligned} \text{Cov} \left\{ \frac{\partial}{\partial u_d} \mathbf{P}(u_d, s), \frac{\partial}{\partial u'_d} \mathbf{P}(u'_d, s') \right\} = a\omega \sigma^2(u_d, s) \\ \times \delta(u_d - u'_d) \delta(s - s') + T_{\text{para}}(u_d, u'_d, s, s') \end{aligned} \quad (13)$$

where $\text{Var}\{\mathbf{P}(u_d, s)\} = \sigma^2(u_d, s)$ denotes the known data variance, which can be a function of u_d and s . The second term $T_{\text{para}}(u_d, u'_d, s, s')$ represents the difference between the term on the left-hand side and the first term on the right-hand side of (13). Although the magnitude of $T_{\text{para}}(u_d, u'_d, s, s')$ can be larger than or comparable to that of the first term in the right-hand side of (13), numerical results that follow show that its contribution to the final image variance on a chord is negligibly small. Therefore, we consider only the first term in the derivation of the chord-image variance below. The parameters a and ω are introduced to account for the interpolation effect of the discrete data derivative and discrete backprojection on the chord-image variance. Using the first term in (13), we can rewrite (12) as

$$\begin{aligned} \text{Cov} \{ \mathbf{g}(x_c, s_a, s_b), \mathbf{g}(x'_c, s_a, s_b) \} \\ \approx a\omega \int_{-\frac{\pi}{2}}^{\frac{\pi}{2}} ds \sigma^2(u_d, s) \delta(u_d - u'_d). \end{aligned} \quad (14)$$

We now consider two points x_c and x'_c on the chord and let u_d and u'_d denote their parallel-beam or fan-beam projections onto the detector. Clearly, for a source position s that satisfies $s \neq s_a$ or s_b , one can conclude that

$$\begin{aligned} u_d - u'_d = 0 & \text{ if } x_c - x'_c = 0 \\ u_d - u'_d \neq 0 & \text{ if } x_c - x'_c \neq 0. \end{aligned} \quad (15)$$

Thus, if $x_c = x'_c$, $\text{Cov}\{\mathbf{g}(x_c, s_a, s_b), \mathbf{g}(x_c, s_a, s_b)\} = \delta(0)a\omega \int_{-\pi/2}^{\pi/2} ds \sigma^2(u_d, s)$ and, if $x_c \neq x'_c$,

$\text{Cov}\{\mathbf{g}(x_c, s_a, s_b), \mathbf{g}(x'_c, s_a, s_b)\} = 0$. Therefore, the covariance of the backprojection image for parallel-beam projections can be re-expressed as

$$\text{Cov} \{ \mathbf{g}(x_c, s_a, s_b), \mathbf{g}(x'_c, s_a, s_b) \} \approx c(x_c) \delta(x_c - x'_c) \quad (16)$$

where

$$c(x_c) = a\omega \int_{-\frac{\pi}{2}}^{\frac{\pi}{2}} ds \sigma^2(u_d, s). \quad (17)$$

2) *Noise Properties of Differentiation/Backprojection for Fan-Beam Data:* In the fan-beam case, we use $\mathbf{P}(u_d, s)$ to denote the projection on detector bin u_d acquired at view s . Again, we assume $\mathbf{P}(u_d, s)$ to be uncorrelated and to satisfy (10). The backprojection image in (6) can be re-expressed as

$$\mathbf{g}(x_c, s_a, s_b) = \int_{s_a}^{s_b} ds \frac{1}{|\vec{r} - \vec{r}_0(s)|^2} \mathbf{P}'(u_d, s) \quad (18)$$

where $u_d = (S\vec{r} \cdot \hat{e}_u(s) / (\vec{r}_0(s) - \vec{r}) \cdot \hat{e}_w(s))$ is the fan-beam projection of x_c onto the detector. The weighted-data derivative $\mathbf{P}'(u_d, s)$ is given by

$$\mathbf{P}'(u_d, s) = A^2(u_d) \left| \frac{d\vec{r}_0(s)}{ds} \right| \frac{\partial}{\partial u_d} \left[\frac{\mathbf{P}(u_d, s)}{A(u_d)} \right]. \quad (19)$$

Using (18), one can write the covariance of the backprojection image as

$$\begin{aligned} \text{Cov} \{ \mathbf{g}(x_c, s_a, s_b), \mathbf{g}(x'_c, s_a, s_b) \} \\ = \int_{s_a}^{s_b} ds \int_{s_a}^{s_b} ds' \frac{1}{|\vec{r} - \vec{r}_0(s)|^2} \frac{1}{|\vec{r} - \vec{r}_0(s')|^2} \\ \times \text{Cov} \{ \mathbf{P}'(u_d, s), \mathbf{P}'(u'_d, s') \} \end{aligned} \quad (20)$$

which depends upon the covariance of $\mathbf{P}'(u_d, s)$. Again, we can conveniently write the covariance of $\mathbf{P}'(u_d, s)$ as

$$\begin{aligned} \text{Cov} \{ \mathbf{P}'(u_d, s), \mathbf{P}'(u'_d, s') \} \\ = a\omega \sigma^2(u_d, s) A^2(u_d) \left| \frac{d\vec{r}_0(s)}{ds} \right|^2 \delta(u_d - u'_d) \delta(s - s') \\ + T_{\text{fan}}(u_d, u'_d, s, s') \end{aligned} \quad (21)$$

where $\text{Var}\{\mathbf{P}(u_d, s)\} = \sigma^2(u_d, s)$ denotes the known data variance, which can be a function of u_d and s . The second term $T_{\text{fan}}(u_d, u'_d, s, s')$ represents the difference between the term on the left-hand side and the first term in the right-hand side of (21). As numerical results indicate, it turns out that $T_{\text{fan}}(u_d, u'_d, s, s')$ will also have a negligible contribution to the chord-image variance. Therefore, we consider only the first term in the derivation of the chord-image variance below. Again, the parameters a and ω are introduced to account for the interpolation effect of the discrete data derivative and discrete

backprojection on the chord-image variance. Using the first term in (21), we can rewrite (20) as

$$\begin{aligned} \text{Cov}\{\mathbf{g}(x_c, s_a, s_b), \mathbf{g}(x'_c, s_a, s_b)\} \\ \approx a\omega \int_{s_a}^{s_b} ds \frac{\sigma^2(u_d, s) A^2(u_d)}{|\vec{r} - \vec{r}_0(s)|^4} \left| \frac{d\vec{r}_0(s)}{ds} \right|^2 \delta(u_d - u'_d). \end{aligned} \quad (22)$$

Similar to the parallel-beam case described previously, using (15), one can conclude that

$$\text{Cov}\{\mathbf{g}(x_c, s_a, s_b), \mathbf{g}(x'_c, s_a, s_b)\} \approx c(x_c) \delta(x_c - x'_c) \quad (23)$$

where

$$c(x_c) = a\omega \int_{s_a}^{s_b} ds \frac{A^2(u_d)}{|\vec{r} - \vec{r}_0(s)|^4} \left| \frac{d\vec{r}_0(s)}{ds} \right|^2 \sigma^2(u_d, s). \quad (24)$$

3) *Noise Properties of Differentiation/Backprojection for Cone-Beam Data:* In the cone-beam case, let $\mathbf{P}(u_d, v_d, s)$ denote the projection at view s on a detector bin specified by (u_d, v_d) . In the so-called “well oriented” rotation-coordinate system [5], unit vector $\hat{e}_u(s)$ is parallel to and unit vectors $\hat{e}_v(s)$ and $\hat{e}_w(s)$ are orthogonal to the tangential direction $(d\vec{r}_0(s)/ds)$ of the source trajectory. Let u_d and v_d denote the coordinates along $\hat{e}_u(s)$ and $\hat{e}_v(s)$. It can be shown [5] that the backprojection image depends only upon the data derivative along u_d . Therefore, the reconstruction formula for the cone-beam backprojection image can be obtained from that for the fan-beam backprojection image in (18) by simply replacing $P(u_d, s)$ and $A(u_d)$ with $P(u_d, v_d, s)$ and $A(u_d, v_d)$, respectively. Subsequently, one can show that the covariance of the cone-beam backprojection image $\mathbf{g}(x_c, s_a, s_b)$ also satisfies (23) and (24).

4) *Estimation of Parameters a and ω in Discrete Form:* The parameter a is introduced to account for the interpolation effect of the discrete data-derivative on the chord-image variance. We consider a two-point derivative, which was used in our numerical studies. Let \mathbf{P}_i denote the discrete data, where $i = 1, 2, \dots, I$, and I indicates the total number of data points. We assume that data \mathbf{P}_i are uncorrelated and use $\text{Var}\{\mathbf{P}_i\}$ to denote their variances. The two-point data derivative is defined as

$$\bar{\mathbf{P}}_i = \frac{1}{2}[\mathbf{P}_{i+1} - \mathbf{P}_{i-1}]. \quad (25)$$

Therefore, the variance of the discrete data derivative $\bar{\mathbf{P}}_i$ can be written as

$$\text{Var}\{\bar{\mathbf{P}}_i\} = \frac{1}{2} \frac{\text{Var}\{\mathbf{P}_{i+1}\} + \text{Var}\{\mathbf{P}_{i-1}\}}{2}. \quad (26)$$

When data variances are identical, (26) becomes

$$\text{Var}\{\bar{\mathbf{P}}_i\} = \frac{1}{2} \text{Var}\{\mathbf{P}_i\}. \quad (27)$$

Therefore, in our studies, we select $a = 1/2$, which is the coefficient in (27).

The parameter ω was introduced to account for the interpolation effect of discrete backprojection on the chord-image variances. The estimated value of ω depends obviously upon the

specific interpolation scheme used in the discrete backprojection. We illustrate our estimation of ω when a two-point interpolation is used for the discrete backprojection in the parallel- and fan-beam cases. One can readily obtain estimates of ω when other interpolation schemes are used. In our studies, u_d is measured in the unit of detector-bin size. Let $i = \text{floor}(u_d) + I_0$, where I_0 denotes the index corresponding to $u_d = 0$. At a backprojection view s , we use \mathbf{P}'_i to denote the discrete weighted-data derivatives. For a given u_d , we express the interpolated weighted-data derivative as

$$\mathbf{P}'_{u_d} = (1 - \gamma)\mathbf{P}'_i + \gamma\mathbf{P}'_{i+1} \quad (28)$$

where $\gamma = u_d - i$. Furthermore, we can write the variance of \mathbf{P}'_{u_d} as

$$\text{Var}\{\mathbf{P}'_{u_d}\} \approx [(1 - \gamma)^2 + \gamma^2] \text{Var}\{\mathbf{P}'_i\}. \quad (29)$$

For the sake of simplifying the estimation of ω , we have ignored the correlation between \mathbf{P}'_i and \mathbf{P}'_{i+1} and assumed that $\text{Var}\{\mathbf{P}'_i\} \approx \text{Var}\{\mathbf{P}'_{i+1}\}$. We select ω as the average over all of the possible γ s, which can be computed as

$$\omega = \int_0^1 [(1 - \gamma)^2 + \gamma^2] d\gamma = \frac{2}{3}. \quad (30)$$

Finally, with a substitution of $a = 1/2$ and $\omega = 2/3$ into (17) and (24), we obtain the variances $c(x_c)$ of the backprojection images on the chords for the parallel-beam and fan-beam projections, respectively, as

$$c(x_c) = \frac{1}{3} \int_{-\frac{\pi}{2}}^{\frac{\pi}{2}} ds \sigma^2(u_d, s) \quad (31)$$

$$c(x_c) = \frac{1}{3} \int_{s_a}^{s_b} ds \frac{A^2(u_d)}{|\vec{r} - \vec{r}_0(s)|^4} \left| \frac{d\vec{r}_0(s)}{ds} \right|^2 \sigma^2(u_d, s). \quad (32)$$

5) *Noise Property of Weighted Hilbert Transform Over a Finite Interval:* The weighted Hilbert transform constitutes an important step in the chord-based BPF, MDFBP, and FBP algorithms. Consequently, the noise properties of these algorithms depend upon that of the weighted Hilbert transform, which we study in the following. Let $\hat{f}(x_c, s_a, s_b)$ denote the weighted Hilbert transform of the backprojection image $g(x_c, s_a, s_b)$

$$\hat{f}(x_c, s_a, s_b) = \frac{1}{b(x_c)} \int_{x_A}^{x_B} \frac{dx'_c}{x_c - x'_c} b(x'_c) g(x'_c, s_a, s_b). \quad (33)$$

We assume that $g(x'_c, s_a, s_b)$ is band-limited to ν_m . Therefore, the Hilbert transform kernel $(1/x_c)$ can be replaced by

$$h(x_c) = -\pi j \int_{-\nu_m}^{\nu_m} d\nu \text{sgn}[\nu] e^{2\pi j \nu x_c} = \frac{2 \sin^2(\pi \nu_m x_c)}{x_c}. \quad (34)$$

In the presence of noise, the weighted Hilbert transform $\hat{f}(x_c, s_a, s_b)$ should be interpreted as a stochastic process,

which is denoted in boldface. The variance of $\hat{\mathbf{f}}(x_c, s_a, s_b)$ can be written as

$$\begin{aligned} \text{Var} \left\{ \hat{\mathbf{f}}(x_c, s_a, s_b) \right\} &= \frac{1}{b^2(x_c)} \int_{x_A}^{x_B} dx'_c \int_{x_A}^{x_B} dx''_c b(x'_c) b(x''_c) \\ &\quad \times h(x_c - x'_c) h(x_c - x''_c) \\ &\quad \times \text{Cov} \{ \mathbf{g}(x'_c, s_a, s_b), \mathbf{g}(x''_c, s_a, s_b) \}. \end{aligned} \quad (35)$$

As (16) and (23) show, the backprojection image $\mathbf{g}(x_c, s_a, s_b)$ can be treated as an approximated uncorrelated stochastic process. Using the result of (16) or (23), we can write (35) as

$$\begin{aligned} \text{Var} \left\{ \hat{\mathbf{f}}(x_c, s_a, s_b) \right\} &= \frac{1}{b^2(x_c)} \int_{x_A}^{x_B} dx'_c c(x'_c) h^2(x_c - x'_c) b^2(x'_c). \end{aligned} \quad (36)$$

In our numerical studies in Sections III-B1 and III-C1, we have used $\nu_m = (1/2\Delta_c)$, where Δ_c denote the sample interval of $\mathbf{g}(x_c, s_a, s_b)$.

6) *Noise Properties of Chord Images*: Using (4), one can write the variance of the reconstructed chord image as

$$\begin{aligned} \text{Var} \{ \mathbf{f}_c(x_c, s_a, s_b) \} &\approx \text{Var} \left\{ \hat{\mathbf{f}}(x_c, s_a, s_b) \right\} + \frac{\text{Var} \{ \mathbf{P}(u_{d0}, v_{d0}, s_a) \}}{4\pi^2 b^2(x_c)} \\ &\quad \times \left[\frac{\sqrt{(l-x_B)(x_A+l)}}{l-x_c} + \frac{\sqrt{(l+x_A)(l+x_B)}}{l+x_c} \right]^2. \end{aligned} \quad (37)$$

Substituting (36) into (37) yields

$$\begin{aligned} \text{Var} \{ \mathbf{f}_c(x_c, s_a, s_b) \} &\approx \frac{1}{b^2(x_c)} \int_{x_A}^{x_B} dx'_c c(x'_c) h^2(x_c - x'_c) b^2(x'_c) \\ &\quad + \frac{\text{Var} \{ \mathbf{P}(u_{d0}, v_{d0}, s_a) \}}{4\pi^2 b^2(x_c)} \\ &\quad \times \left[\frac{\sqrt{(l-x_B)(x_A+l)}}{l-x_c} + \frac{\sqrt{(l+x_A)(l+x_B)}}{l+x_c} \right]^2 \end{aligned} \quad (38)$$

which provides a formula for computing the chord-image variance.

B. Numerical Studies of Noise Properties in Parallel-Beam Reconstruction

Using the parallel-beam configuration in Fig. 1(b) and the parameters given in Table I, we calculated noiseless projections for the numerical phantom in Fig. 1(a). We have used an object-independent Gaussian noise model and an object-dependent Poisson-noise model in the numerical studies. For each noise model, we generated 10 000 sets of noisy data by using noiseless data as the means. The standard deviation σ_0 of Gaussian noise used is 1.6% of the maximum value in the noiseless data,

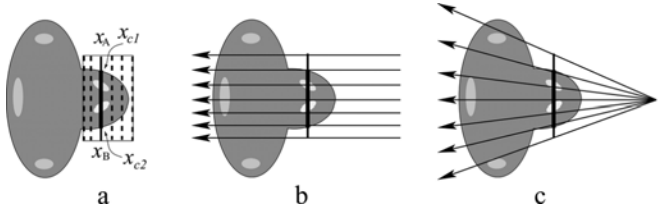


Fig. 1. (a) Phantom in numerical studies. (b) Parallel-beam configuration. (c) Fan-beam configuration. Solid line segment with endpoints x_A and x_B represents reconstruction segment. Thick segment with endpoints x_{c1} and x_{c2} indicates support segment. It should be noted that $[x_A, x_B] \supseteq [x_{c1}, x_{c2}]$. Rectangular ROI is decomposed into a set of (dashed) line segments.

whereas the standard deviation for the Poisson noise is the noiseless data scaled to yield a total photon count of 5×10^5 for each view. We investigated four reconstruction segments with different lengths $L_{AB} = |x_B - x_A| : 7.8, 10.0, 14.1$, and 20.0 cm, all of which are located at $x = 4.06$ cm. It can be observed in Fig. 1(b) that the length of the support segment, 5.5 cm in length, is shorter than the four reconstruction segments considered. Therefore, the image on this chord can be reconstructed exactly by use of data determined by these reconstruction segments. One can also conclude from Fig. 1(b) that the minimum data required by the first three reconstruction segments, which are shorter than the maximum dimension (about 15.6 cm) of the object support, are truncated.

1) *Noise Properties in Reconstruction from Truncated Parallel-Beam Data*: From the 10 000 sets of data containing Gaussian noise, we used (4)–(6) to reconstruct 10 000 noisy $\mathbf{f}_c(x_c, s_a, s_b)$, $\hat{\mathbf{f}}(x_c, s_a, s_b)$, and $\mathbf{g}(x_c, s_a, s_b)$, respectively, on the four reconstruction segments described previously. Based upon these noisy reconstructions, we subsequently computed their corresponding empirical variances, which are shown in the upper row of Fig. 2. We compare the empirical results to the analytical results obtained by use of (16), (36), and (38). The function $c(x_c)$ is determined by using $\sigma(u_d, s) = \sigma_0$ in (31), where σ_0 is 1.6% of the maximum value in noiseless data. The analytical results are displayed in the middle row of Fig. 2. Similarly, using (4)–(6), we reconstructed 10 000 sets of noisy $\mathbf{g}(x_c, s_a, s_b)$, $\hat{\mathbf{f}}(x_c, s_a, s_b)$, and $\mathbf{f}_c(x_c, s_a, s_b)$ on the four segments from 10 000 sets of data containing Poisson noise. The computed empirical variances from these noisy images are displayed in the upper row of Fig. 3. Using the noiseless data as the Poisson-noise variance $\sigma^2(u_d, s)$ in (17), one can readily determine $c(x_c)$; and using the determined $c(x_c)$ in (16), (36), and (38), one can compute analytical image variances, which are displayed in the middle row of Fig. 3. The results show that the analytical and empirical results agree well with each other, suggesting that (38) provides an adequate estimation of the chord-image variance.

It can also be observed in Fig. 2(c) and Fig. 3(c) that the shorter the reconstruction segment, the higher the chord-image variances. This is only because the second term in (38) increases as L_{AB} (i.e., $(x_A - x_c)(x_c - x_B)$) decreases. However, the difference of the chord-image variances in the central part of the support segment is quite small among these reconstruction segments. The implication of this result is that there may be a significant gain in terms of dose reduction by using a short

TABLE I

PARAMETERS FOR CIRCULAR PARALLEL-BEAM, CIRCULAR FAN-BEAM, AND HELICAL CONE-BEAM SCANNING CONFIGURATIONS WHICH ARE USED IN OUR SIMULATION STUDIES. SDD IS SOURCE-TO-DETECTOR DISTANCE AND SID DENOTES SOURCE-TO-ISOCENTER DISTANCE

	Circular parallel-beam scan	Circular fan-beam scan	Helical cone-beam scan
Number of views per turn	1024	512	300
Angular range	$[-\frac{\pi}{2}, \frac{\pi}{2}]$	$[-\pi, \pi]$	$[-\pi, \pi]$
Detector bins	256	256	128×128
Detector bin size (mm)	1.1	1.6	3.1×3.1
SDD (mm)	-	200	200
SID (mm)	-	200	200
Helical pitch (mm)	-	-	90

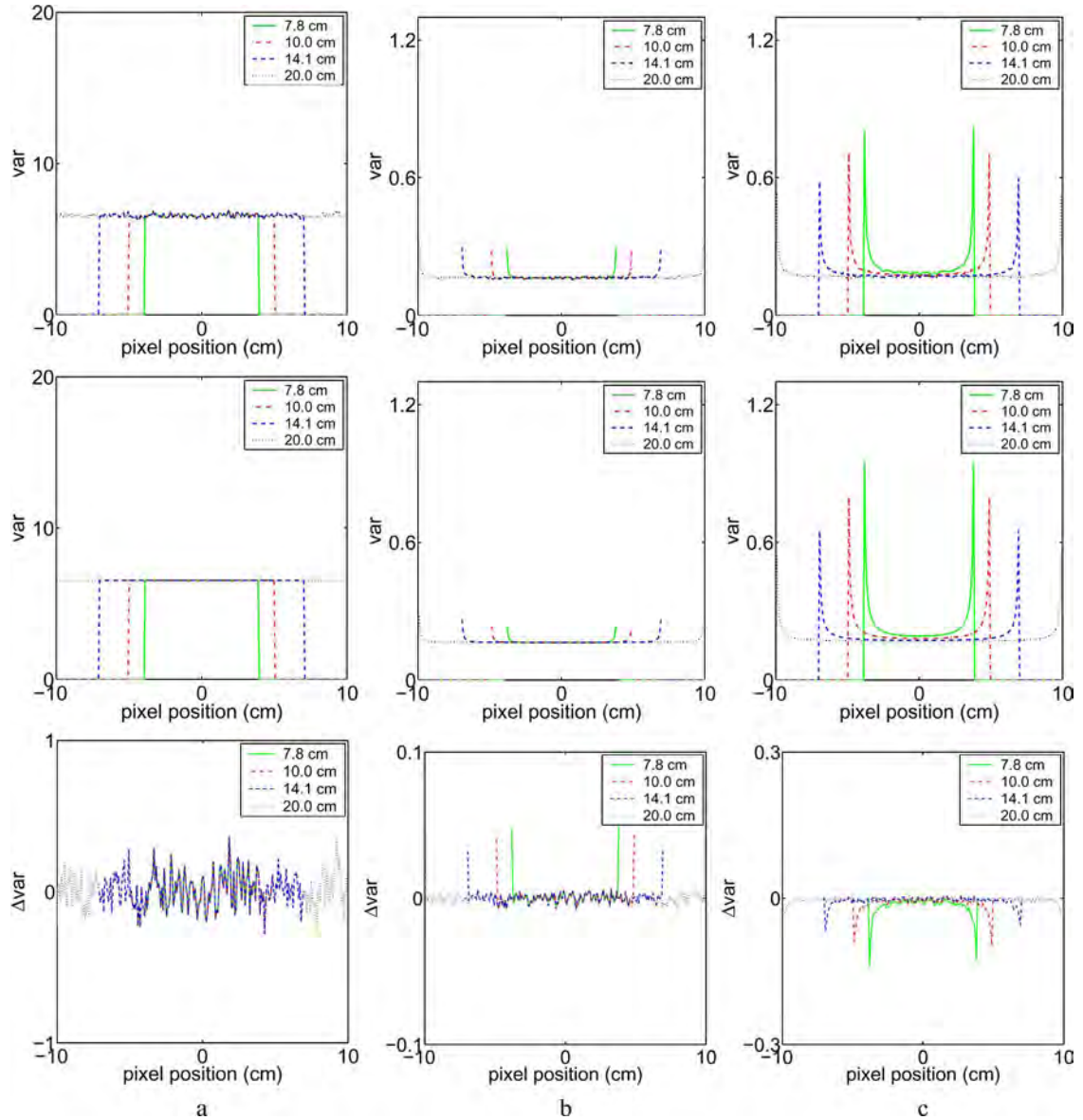


Fig. 2. Empirical (top row) and analytical (middle row) variances of (a) $g(x_c, s_a, s_b)$, (b) $\hat{f}(x_c, s_a, s_b)$, and (c) $f_c(x_c, s_a, s_b)$ obtained on four reconstruction segments from parallel-beam data containing Gaussian noise. Difference between empirical variances and analytical variances is also shown in bottom row, which demonstrates analytical variances agree well with the empirical variances. Lengths of these segments are indicated in the box in upper-right corners of plots.

reconstruction segment, because data required to reconstruct an image on this reconstruction segment is less than that required by using a longer reconstruction segment, thus resulting in a reduced illumination coverage to the object. For similar X-ray

intensities, which are directly related to the data-noise level, the reconstruction using a short reconstruction segment appears to yield image variance within the support segment that is comparable to that obtained with a longer reconstruction segment.

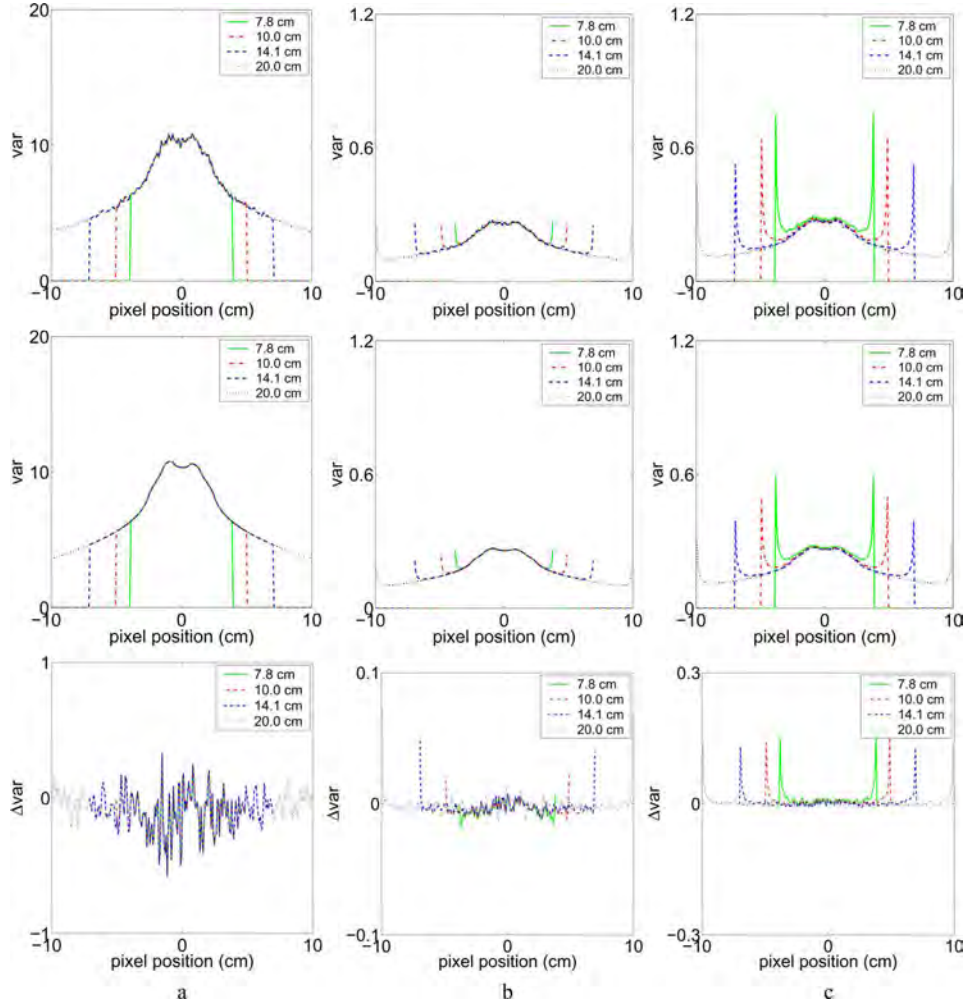


Fig. 3. Empirical (top row) and analytical (middle row) variances of (a) $g(x_c, s_a, s_b)$, (b) $\hat{f}(x_c, s_a, s_b)$, and (c) $f_c(x_c, s_a, s_b)$ obtained on four reconstruction segments from parallel-beam data containing Poisson noise. Difference between empirical variances and analytical variances is also shown in bottom row, which demonstrates analytical variances agree well with empirical variances. Lengths of these segments are indicated in the box in upper-right corners of plots.

We have also performed numerical studies of the noise properties of the reconstructed ROI images by use of the BPF and MDFBP algorithms from truncated data. Using the numerical phantom in Fig. 1 and each of Gaussian- and Poisson-noise models described above, we generated 500 noisy, truncated data sets for image reconstruction on reconstruction segments of a length $L_{AB} = 10.0$ cm, as shown in Fig. 1(a), which completely cover the ROI. We subsequently reconstructed 500 noisy images by using the BPF and MDFBP algorithms. We display in Fig. 4 noisy ROI images reconstructed using the BPF and MDFBP algorithms from data containing Gaussian noise (upper row) and Poisson noise (lower row).

Using the reconstructed 500 sets of Gaussian-noise images and 500 sets of Poisson-noise images, we computed empirical variances of the ROI images, which are shown in the upper row and lower row of Fig. 5, respectively. We display in the third column of Fig. 5 the variance profiles on the dashed lines indicated in the variance images. Results in Fig. 5 support the conclusion that both BPF and MDFBP algorithms yield images with comparable variance levels.

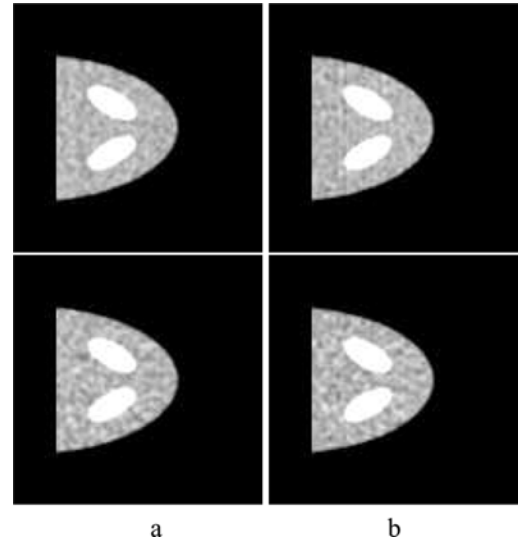


Fig. 4. ROI-images obtained by use of (a) BPF algorithm and (b) MDFBP algorithm from truncated parallel-beam data containing Gaussian noise (upper row) and Poisson noise (lower row).

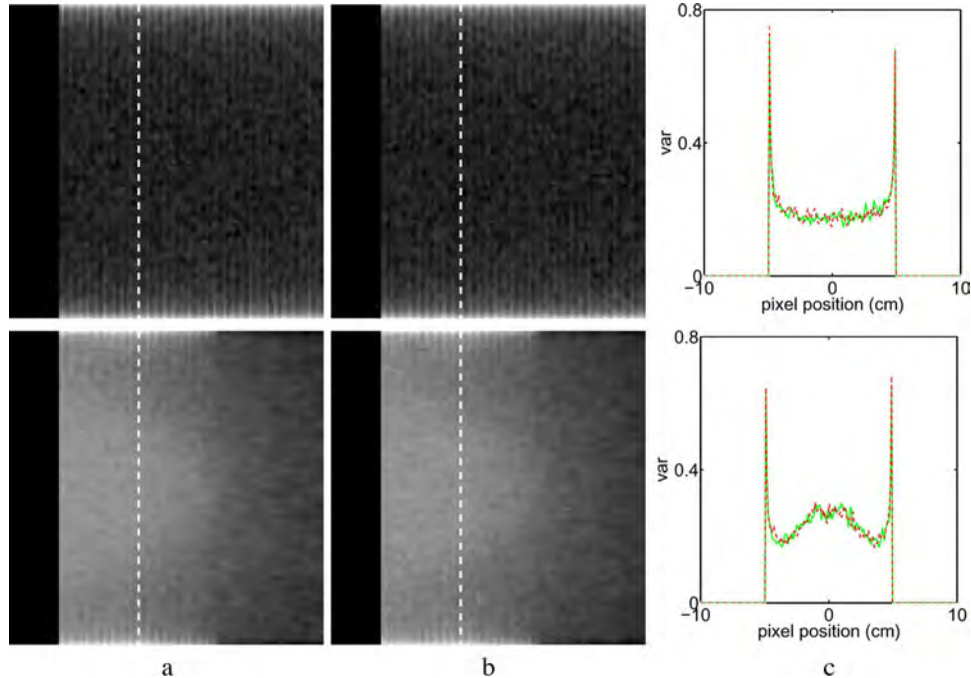


Fig. 5. Empirical ROI-image variances obtained by use of (a) BPF and (b) MDFBP algorithms from truncated parallel-beam data containing Gaussian noise (upper row) and Poisson noise (lower row), respectively. (c) Variance profiles on the dashed lines indicated in columns (a) and (b) obtained with the BPF (solid) and MDFBP (dashed) algorithms, respectively. For purpose of displaying details in central (i.e., low variance) regions, we have applied a logarithmic scale to the variance images. Display windows are $[-0.86, 0.50]$ and $[-1.28, 0.20]$ for Gaussian noise and Poisson noise, respectively.

2) *Noise Properties in Reconstruction from Nontruncated Parallel-Beam Data:* As discussed above, the FBP algorithm cannot reconstruct exactly images from truncated data. Therefore, we study the noise properties of the FBP algorithm from parallel-beam data without truncations. For the purpose of comparison, we have also included reconstruction results of the BPF and MDFBP algorithms from the same nontruncated data. Using the numerical phantom in Fig. 1 and each of the Gaussian- and Poisson-noise models, we generated 500 noisy data sets from which 500 noisy images were obtained by use of each of the BPF, MDFBP, and FBP algorithms. Using these noisy images, we computed empirical variance images, which are shown in the upper and lower rows of Fig. 6, respectively, for the Gaussian- and Poisson-noise models. We also display in Fig. 7 the variance profiles on the dashed lines (i.e., on a chord) indicated on the variance images in Fig. 6. The profile results were obtained by use of the BPF (solid), MDFBP (dashed), and FBP (dotted) algorithms for the (a) Gaussian-noise model and (b) Poisson-noise model. It can be observed that image variances obtained with the three algorithms are similar and that the only difference comes at the extreme ends of the shown reconstruction segments. The BPF and MDFBP algorithms show a significant increase in the image variance at both ends of the profile. The reason for this is that the reconstruction segment was taken to be the width of the image array, and the prefactor for the finite Hilbert transform in (4) and (7) has a singularity at the ends of the reconstruction segment. In practical situations this prefactor is of little consequence because the reconstruction segment can be selected larger to avoid the singular behavior; furthermore, because the singularity goes as the $-1/2$ power, its effect is evident only very close to the endpoints of the reconstruction segment.

C. Numerical Studies of Noise Properties in Fan-Beam Reconstruction

Using the fan-beam configuration in Fig. 1(c) and the parameters listed in Table I, we calculated fan-beam noiseless data for the numerical phantom in Fig. 1(a). We have also used an object-independent Gaussian-noise model and an object-dependent Poisson-noise model in this numerical study. The standard deviation σ_0 of Gaussian noise used is 2.3% of the maximum value in noiseless fan-beam data, whereas the standard deviation for the Poisson noise is the noiseless data scaled to yield a total photon count of 5×10^5 for each view. For each noise model, 10 000 sets of noisy data were generated by use of the corresponding noiseless data as the means. We investigated reconstruction segments of four different lengths $L_{AB} = 7.8, 10.0, 14.1$, and 20.0 cm. All of the segments are located at $x = 4.06$ cm. It can be observed in Fig. 1(c) that the length of the support segment is 5.5 cm, which is shorter than the four reconstruction segments. Therefore, the image on this chord can be reconstructed exactly by use of data determined by these reconstruction segments. One can also conclude from Fig. 1(c) that data determined by the first three reconstruction segments, which are shorter than the maximum dimension (about 15.6 cm) of the object support, are truncated.

1) *Noise Properties in Reconstruction from Truncated Fan-Beam Data:* From the 10 000 sets of data containing Gaussian noise, we used (4)–(6) to reconstruct 10 000 noisy $\mathbf{f}_c(x_c, s_a, s_b)$, $\hat{\mathbf{f}}(x_c, s_a, s_b)$, and $\mathbf{g}(x_c, s_a, s_b)$, respectively, on the four reconstruction segments described. Based upon these noisy reconstructions, we subsequently computed their corresponding empirical variances, which are shown in the upper row of Fig. 8.

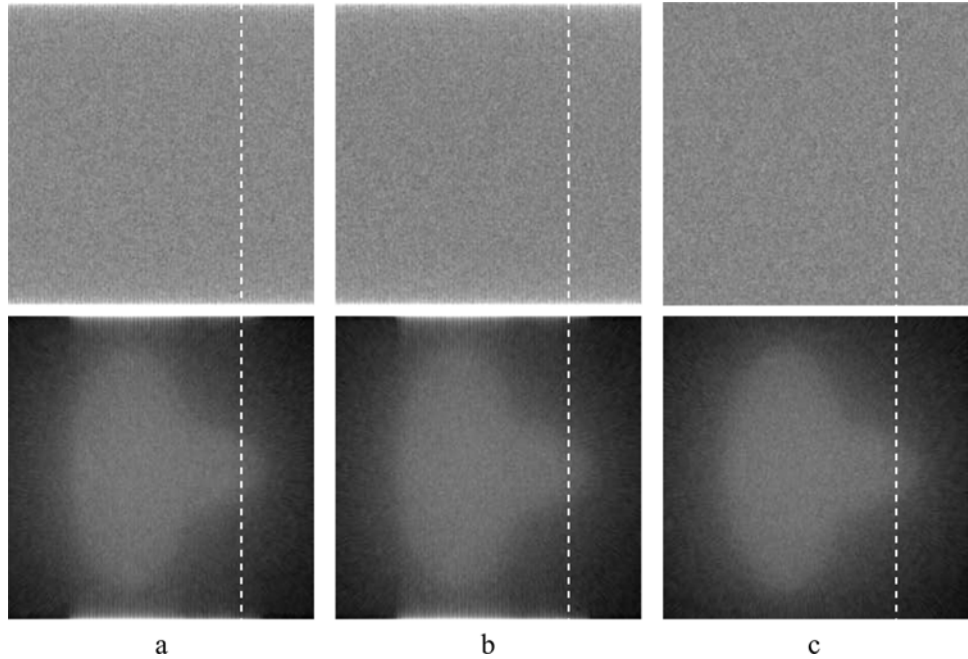


Fig. 6. Empirical variance images obtained by use of (a) BPF, (b) MDFBP, and (c) FBP algorithms from nontruncated parallel-beam data containing Gaussian noise (upper row) and Poisson noise (lower row). For the purpose of displaying details in central (i.e., low variance) regions, we have applied a logarithmic scale to variance images. Display windows are $[-1.3, 0.30]$ and $[-1.3, 0.40]$ for Gaussian noise and Poisson noise, respectively.

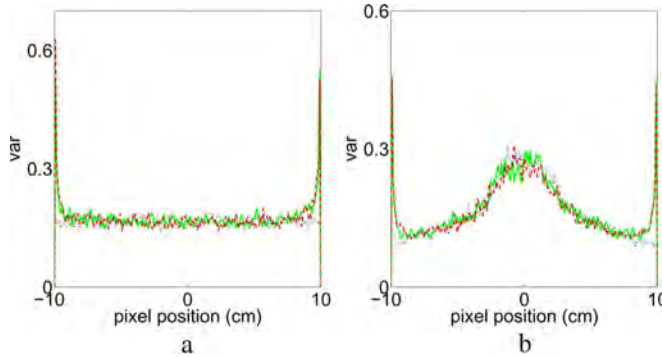


Fig. 7. Variance profiles on the dashed lines indicated in variance images shown in Fig. 6. They were obtained for the Gaussian (a) and Poisson (b) noise models by use of the BPF (solid), MDFBP (dashed), and FBP (dotted) algorithms, respectively.

As for the analytic variance, one can determine $c(x_c)$ by using $\sigma(u_d, s) = \sigma_0$ in (32), where σ_0 is 2.3% of the maximum value in noiseless fan-beam data. Using $c(x_c)$ in (23), (36), and (38), we computed analytically image variances, which are displayed in the middle row of Fig. 8. Similarly, using (4)–(6), we reconstructed 10 000 sets of noisy $\mathbf{f}_c(x_c, s_a, s_b)$, $\hat{\mathbf{f}}(x_c, s_a, s_b)$, and $\mathbf{g}(x_c, s_a, s_b)$ on the four segments from 10 000 sets of fan-beam data containing Poisson noise. The computed empirical variances from these noisy images are displayed in the upper row of Fig. 9. Furthermore, using the noiseless fan-beam data as the Poisson-noise variance $\sigma^2(u_d, s)$ in (32), one can readily determine $c(x_c)$. Using the determined $c(x_c)$ in (23), (36), and (38), we computed analytically image variances, which are displayed in the middle row of Fig. 9. It can be observed that the analytic and empirical results agree well with each other,

suggesting that (38) provides an adequate analytic estimation of the chord-image variance for the fan-beam case as well. It is interesting to note in Fig. 8(a) and Fig. 9(a) that the variances of $\mathbf{g}(x_c, s_a, s_b)$ are spatially varying on the chord. Based upon (32), one can readily conclude that this spatial variation is caused by the spatially variant factor $(A^2(u_d)/|\vec{r} - \vec{r}_0(s)|^4)$.

Again, from these results, observations similar to those for the parallel-beam case can be made for the fan-beam case. For example, as Fig. 8(c) and Fig. 9(c) show, the shorter the reconstruction segment, the higher the chord-image variances. This is only because the second term in (38) increases as L_{AB} (i.e., $(x_A - x_c)(x_c - x_B)$) decreases. The implication of these results is that there may be a significant gain in terms of dose reduction by using a short reconstruction segment, because data required to reconstruct an image on this reconstruction segment is less than that required by using a longer reconstruction segment, which can result in reduction of illumination coverage of the object.

We have also performed numerical studies of the noise properties of the reconstructed ROI images by use of the BPF and MDFBP algorithms from truncated data. Using the numerical phantom in Fig. 1 and each of the Gaussian- and Poisson-noise models described previously, we generated 500 noisy truncated data sets for image reconstruction on reconstruction segments of a length $L_{AB} = 10.0$ cm, as shown in Fig. 1(a), which cover the ROI completely. We subsequently reconstruct 500 noisy images by using each of the BPF and MDFBP algorithms. Using the reconstructed 500 sets of Gaussian-noise images and 500 sets of Poisson-noise images, we computed empirical variance images within the ROI, which are shown in the upper row and lower row of Fig. 10, respectively. Moreover, we display in the third column of Fig. 10 the variance profiles on the dashed lines

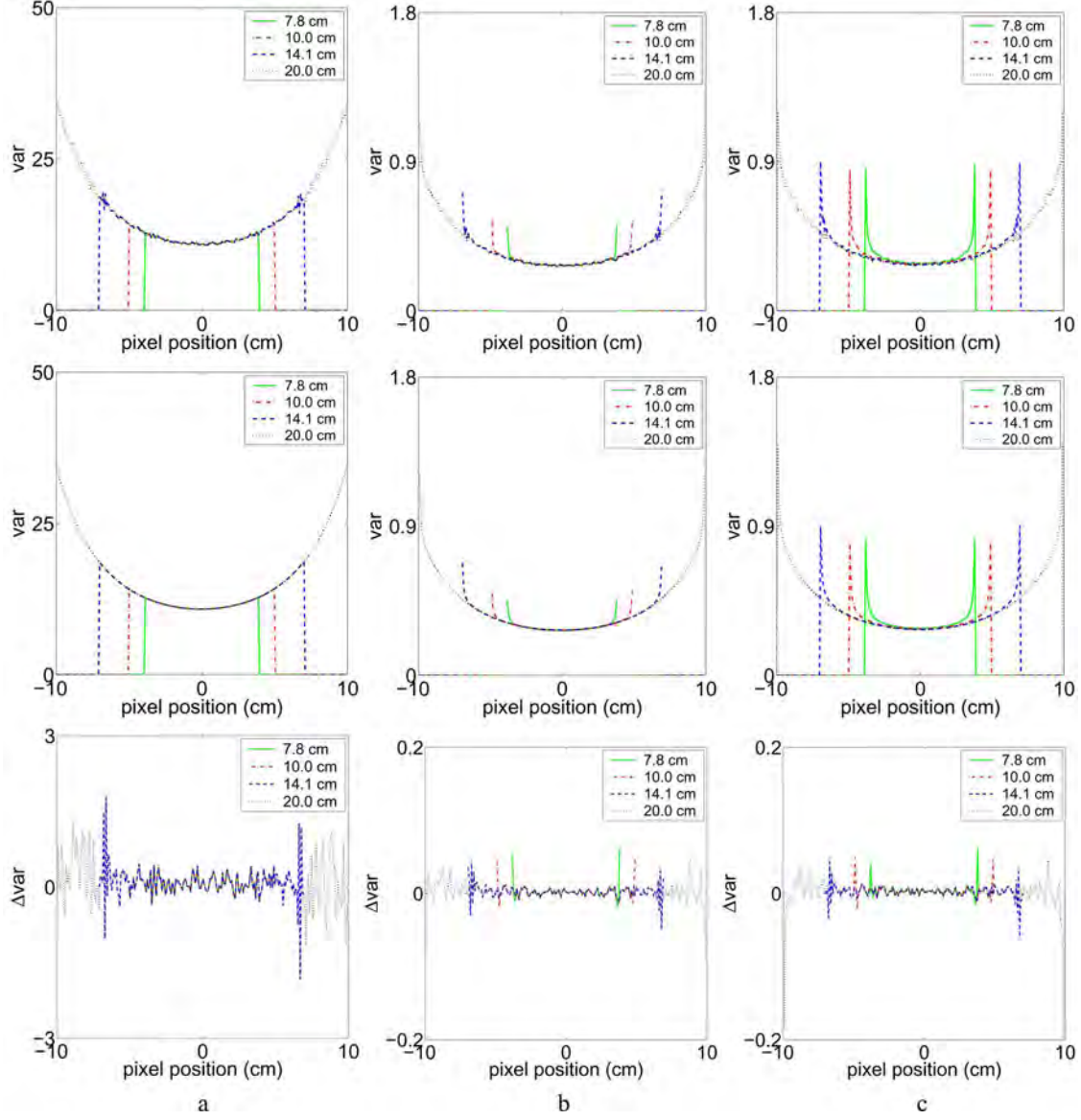


Fig. 8. Empirical (top row) and analytical (middle row) variances of (a) $g(x_c, s_a, s_b)$, (b) $\hat{f}(x_c, s_a, s_b)$, and (c) $f_c(x_c, s_a, s_b)$ obtained on four reconstruction segments from fan-beam data containing Gaussian noise. Difference between empirical variances and analytical variances is also shown in bottom row, which demonstrates the analytical variances agree well with the empirical variances. Lengths of these segments are indicated in the box in upper-right corners of plots.

indicated in the variance images. Results in Fig. 10 support the conclusion that both BPF and MDFBP algorithms yield images with comparable variance levels.

2) *Noise Properties in Reconstruction From Nontruncated Fan-Beam Data*: The FBP algorithm cannot reconstruct exactly images from truncated fan-beam data. Thus, we evaluate the noise properties of the FBP reconstruction from nontruncated fan-beam data. For the purpose of comparison, we have also included reconstruction results of the BPF and MDFBP algorithms from the same data sets. Using the numerical phantom and fan-beam configuration described above, we generated nontruncated fan-beam data at 512 views uniformly covering 2π . Using the noiseless data as the means, we generated 500 sets of data containing Gaussian noise and 500 sets of data containing Poisson noise. The standard deviation for the Gaussian noise is 2.3% of the maximum value of the noiseless data, whereas the standard deviation for the Poisson noise is the noiseless

data scaled to yield a total photon count of 5×10^5 for each view. For a given chord specified by s_a and s_b , one can reconstruct its image from data acquired over the right-side trajectory (i.e., $s \in [s_a, s_b]$), as shown in Fig. 11(a). Conversely, one can also reconstruct the chord image from data acquired with both right-side trajectory (i.e., $s \in [s_a, s_b]$) and left-side trajectory (i.e., $s \in [s_b, s_a]$), as shown in Fig. 11(b). In chord-based image reconstruction, we decompose image area into chords parallel to the vertical direction and the source scans from s_a to s_b and then from s_b to s_a , as shown in Fig. 11.

For each chord in the set covering the image area, we first reconstructed the images by use of the BPF, MDFBP, and FBP algorithms from data containing Gaussian noise acquired over the right-side trajectory specified by $s \in [s_a, s_b]$. Subsequently, we computed empirically chord-image variances from these noisy reconstructions. By assembling the chord-image variances, we obtain the variance images, which are shown in the upper row of

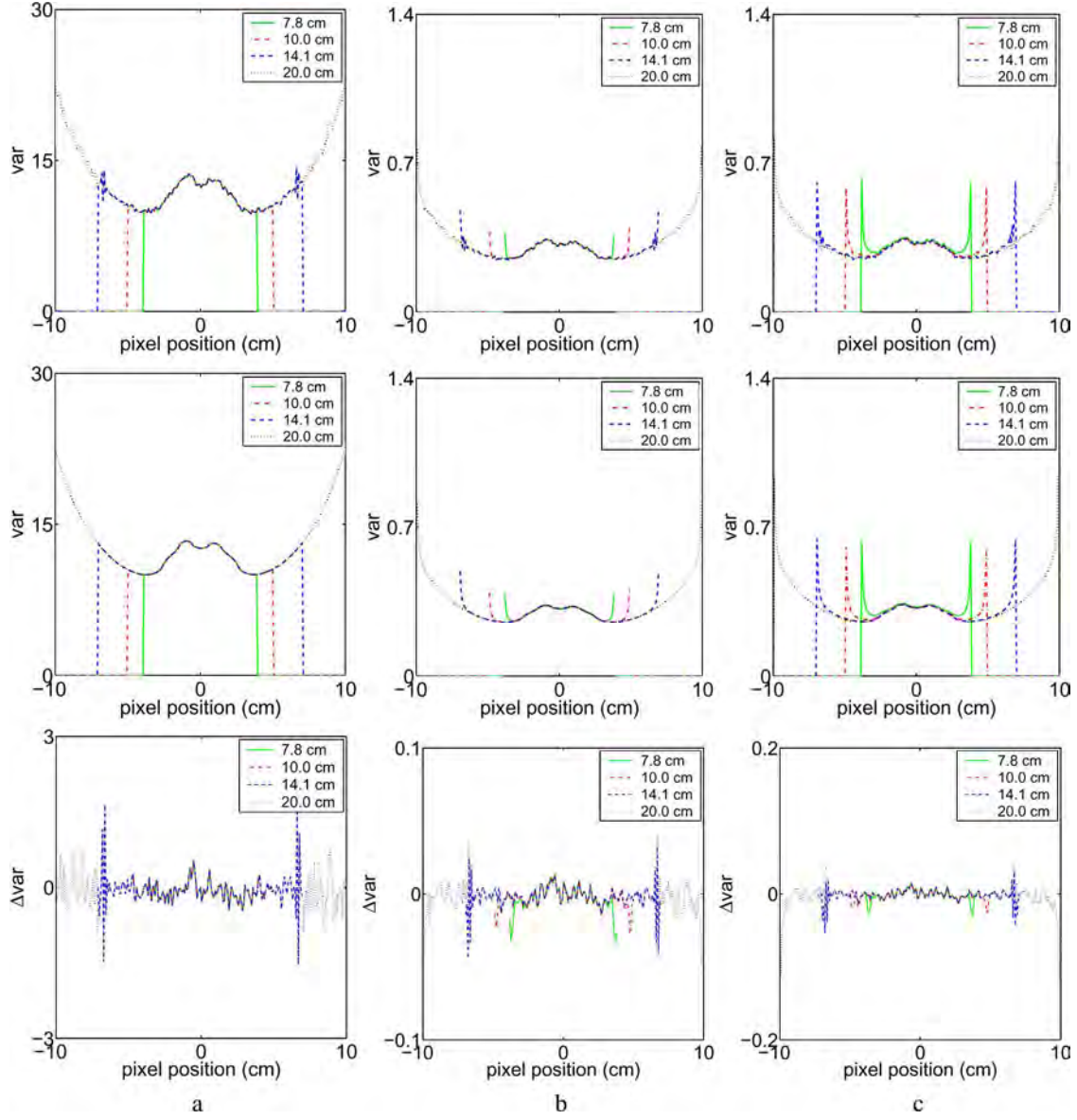


Fig. 9. Empirical (top row) and analytical (middle row) variances of (a) $g(x_c, s_a, s_b)$, (b) $\hat{f}(x_c, s_a, s_b)$, and (c) $f_c(x_c, s_a, s_b)$ obtained on four reconstruction segments from fan-beam data containing Poisson noise. Difference between empirical variances and analytical variances is also shown in bottom row, which demonstrates analytical variances agree well with empirical variances. Lengths of these segments are indicated in the box in upper-right corners of plots.

Fig. 12, for the BPF, MDFBP and FBP algorithms, respectively. Similarly, from data containing Poisson noise, we obtained the image variances, which are displayed in lower row of Fig. 12.

We show in column one of Fig. 13 the image variances on a chord specified by $s_a = -\pi/2$ and $s_b = \pi/2$ obtained from data containing Gaussian noise (upper row) and Poisson noise (lower row), respectively. As already seen, the variance increases with the position along the chord near the source trajectory. There is little difference between the three algorithms. Furthermore, these variance images have similar properties: the chords on the right part have higher and more nonuniform image variance than those on the left part in the image area. In column 2 of Fig. 13, we show the profiles on the middle points across the vertical chords (i.e., on the middle horizontal lines in the variance images shown in Fig. 12). The results reveal that some difference of the MDFBP result from the BPF and FBP results

in the peripheral region. This difference may be attributed to the data weighting prior to the backprojection step, which differs from that in the BPF and FBP algorithms. We should point out that this difference is only seen in the extreme periphery of the imaging area. For most practical situations these three algorithms perform virtually identically in terms of image variance.

We investigate further the general trend of the variance decreasing for chords on the left of the variance image. The first impression of this behavior is that this trend is obvious, because the scanning trajectory is on the right side, chords on the left of the variance image are reconstructed with a longer scanning trajectory. It appears that more data are used in reconstructing chords covering the left part of the variance image. This explanation is, however, incorrect. First, there is a slight upturn in the variance for the chords on the extreme left of the variance image, which runs counter to this trend. Second,

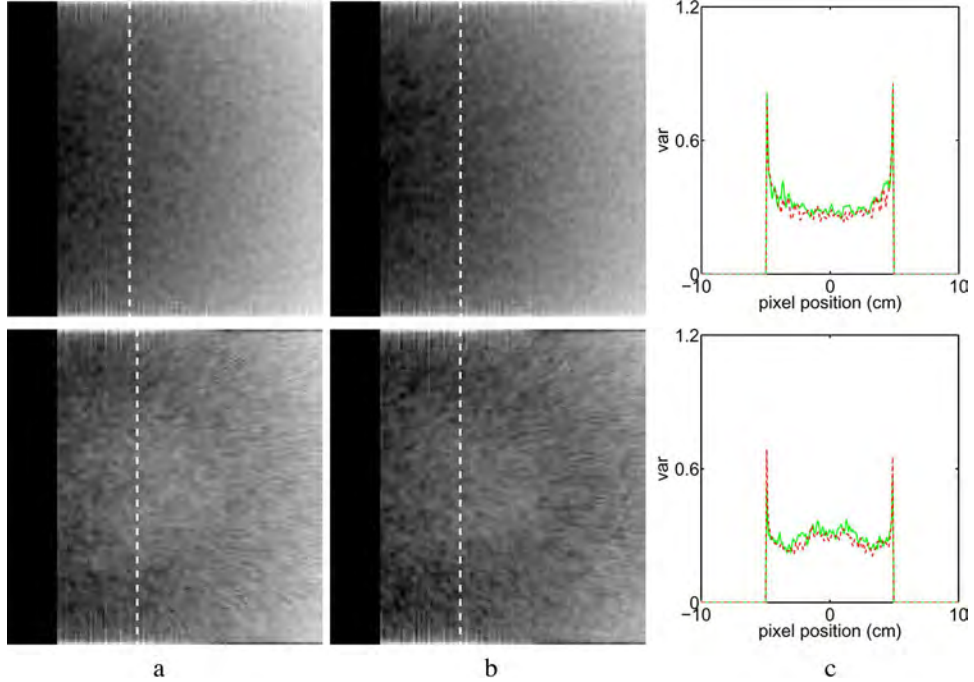


Fig. 10. Empirical ROI-image variances obtained by use of (a) BPF and (b) MDFBP algorithms from truncated fan-beam data containing Gaussian noise (upper row) and Poisson noise (lower row), respectively. (c) Variance profiles on dashed lines indicated in columns (a) and (b) obtained with BPF (solid) and MDFBP (dashed) algorithms, respectively. For the purpose of displaying details in central (i.e., low variance) regions, we have applied a logarithmic scale to variance images. Display windows are $[-0.76, 0.29]$ and $[-0.75, -0.04]$ for Gaussian noise and Poisson noise, respectively.

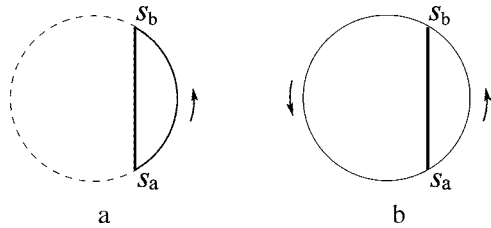


Fig. 11. (a) Right-side trajectory (solid) of chord (thick) specified by s_a and s_b . (b) Right-side trajectory (solid) and left-side trajectory (solid) of chord (thick) specified by s_a and s_b . Scanning configuration in (b) corresponds to a full fan-beam scan.

it can be demonstrated that the amount of data going into the chord reconstruction does not necessarily increase as the scanning trajectory increases. Based upon (32), one can conclude that the true cause of the variance behavior is spatially dependent weighting factor, $1/|\vec{r} - \vec{r}_0(\lambda)|$, in the BPF, MDFBP, and FBP algorithms [19].

For a given chord specified by s_a and s_b , when full scan data are available, one can reconstruct two chord images by use of data acquired with the right-side and left-side trajectories, as shown in Fig. 11 and then obtain a final chord image by averaging the two chord images. We show, in Fig. 14, the variance images of the full scan with accompanying profiles in Fig. 15.

D. Numerical Studies of Noise Properties in Cone-Beam Reconstruction

The BPF and MDFBP algorithms can yield exact image reconstruction on a chord specified by s_a and s_b as long as the

support segment on the chord is illuminated by the X-ray beam at the projection views $s \in [s_a, s_b]$, because these algorithms require data only on the fan-beam projections of the support segment. From the perspective of the chord-based algorithms, the reconstruction of a chord image from cone-beam data is similar to that of a chord image from fan-beam data. In the fan-beam case, the orientation of the fan-beam planes at different views remain unchanged, whereas, in the cone-beam case with a non-planar trajectory, the orientation of the fan-beam-illumination planes generally varies from view to view. As discussed in Section III-A3, the noise properties of differentiation, backprojection, and filtration in the cone-beam case are similar to that in the fan-beam case. Therefore, we include below only the study results on the noise properties of the final chord-images reconstructed from cone-beam data.

1) *Helical Cone-Beam Configuration*: In our investigation of the noise properties of image reconstruction from cone-beam data, we consider the helical trajectory, which is the most widely used in clinical and industrial CT. For a helical scan, the source trajectory is described mathematically as $\vec{r}_0(s) = (R \cos s, R \sin s, (h/2\pi)s)$, where R is the source to center-of-rotation distance, and h indicates the helical pitch. For a chord specified by s_a and s_b , if $(n-1)\pi \leq |s_b - s_a| \leq (n+1)\pi$, where n is a positive odd integer, the chord is also referred to as an $n\pi$ -line segment [20], [21], as shown in Fig. 16(a). In particular, when $n = 1$ and thus $0 \leq |s_b - s_a| \leq 2\pi$, the chord is referred to as a π -line segment [2], [11]. In this paper, we consider image reconstruction only on π -line segments for the reason that the imaging volume enclosed by the helix can be filled uniquely and completely by

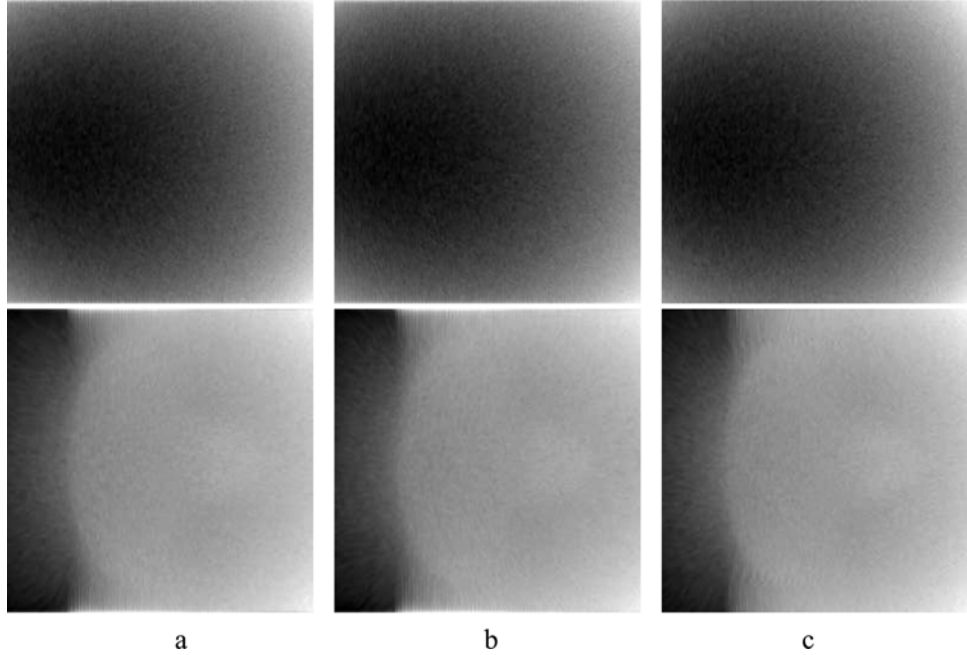


Fig. 12. Empirical variance images obtained by use of (a) BPF, (b) MDFBP, and (c) FBP algorithms from nontruncated fan-beam data containing Gaussian (upper row) and Poisson (lower row) noise. For the purpose of displaying details in central (i.e., low variance) regions, we have applied a logarithmic scale to variance images. Display window is $[-1.0, 0.65]$ and $[-2.02, 0.29]$ for Gaussian noise and Poisson noise, respectively.

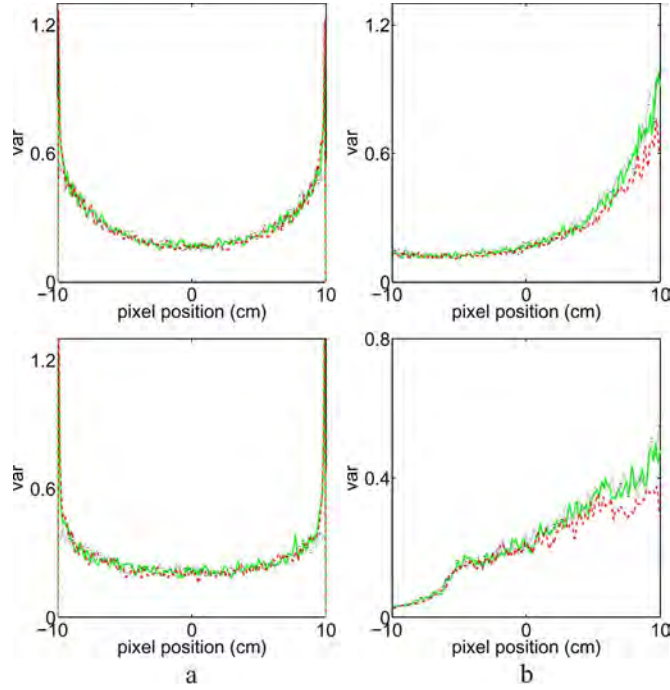


Fig. 13. Variance profiles along central (a) vertical and (b) horizontal lines in variance images shown in Fig. 12, obtained by BPF (solid), MDFBP (dashed), and FBP (dotted) algorithms from data containing Gaussian noise (upper row) and Poisson noise (lower row).

π -line segments [11], [12]. Thus, π -line segments can be used to form 3-D images in a helical cone-beam scan.

We computed the noiseless data from a Shepp-Logan phantom by use of the configuration parameters in Table I.

Using the noiseless data as the means, we subsequently generated 500 sets of data containing Gaussian noise and 500 sets of data containing Poisson noise, respectively. The standard deviation of Gaussian noise is chosen to be 0.7% of the maximum value of the noiseless data, whereas the standard deviation for the Poisson noise is the noiseless data scaled to yield a total count of 5×10^5 for each view.

2) Noise Properties in Reconstruction From Helical Cone-Beam Data: A curved surface in the helix volume can be formed by a set of π -line segments for which we fix one end-point at s_a and sweep the other endpoint over a range $s_b \in [s_{\min}, s_{\max}]$. We show in Fig. 16(a) a curved surface obtained by concatenating a set of π -line segments specified by $s_a = -\pi$ and $s_b \in [-0.5\pi, 0.5\pi]$. Using generated noisy helical cone-beam data, we reconstructed noisy images on the π -line surface by use of the BPF, MDFBP, and FBP algorithms. From these noisy images we subsequently computed empirical image variances on the π -line surface. In Fig. 17, we display the image variances obtained with BPF, MDFBP, and FBP algorithms from data containing Gaussian noise and Poisson noise.

We also display in Fig. 18(a) and (b) image variances on the π -line segment specified by $s_a = -\pi$ and $s_b = 0$ in the surface, obtained from data containing Gaussian noise and Poisson noise, respectively. The image variances show similar characteristics to that of fan-beam image variances observed in Fig. 13. Namely, the variance image on the π -line surface in Fig. 17 has a structure that is similar to the right-side scan fan-beam results presented in Section III-C-1; the images on π -line segments reconstructed from smaller helix segments tend to have higher and more nonuniform variances. The similarity with the fan-beam case is not surprising because the geometrical arrangement of

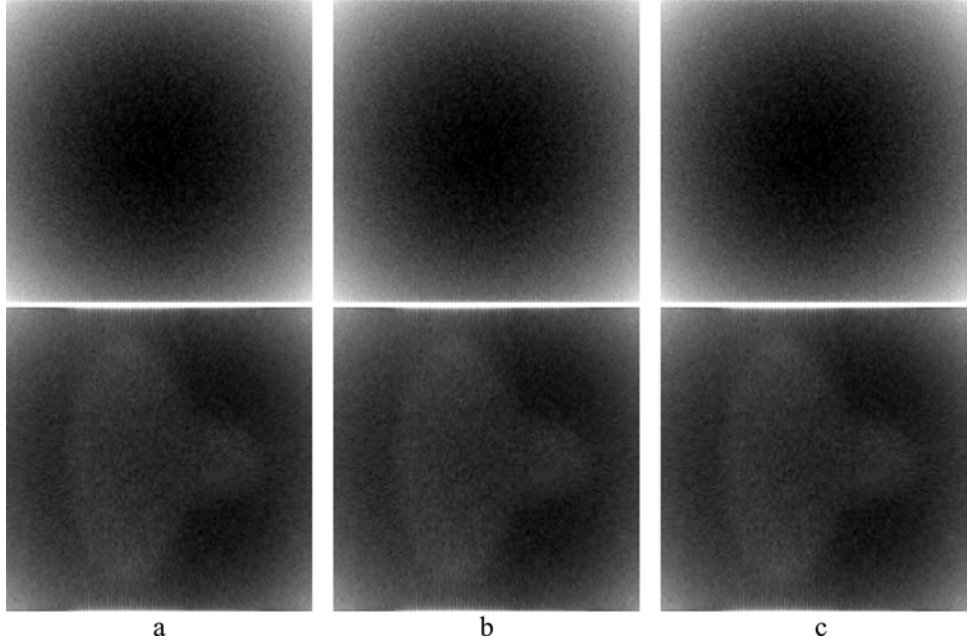


Fig. 14. Variance images obtained by use of (a) BPF, (b) MDFBP, and (c) FBP algorithms from full-scan fan-beam data containing Gaussian (upper row) and Poisson (lower row) noise. For the purpose of displaying details in central (i.e., low variance) regions, we have applied a logarithmic scale to variance images. Display windows are $[-1.19, 0.31]$ and $[-1.18, 0.20]$ for Gaussian noise and Poisson noise, respectively.

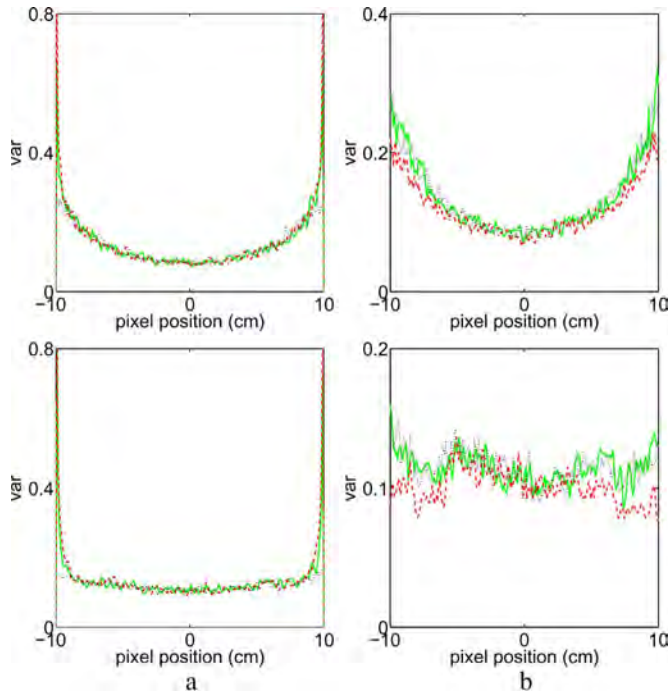


Fig. 15. Variance profiles along the central (a) vertical and (b) horizontal lines in variance images, which are shown in Fig. 14, obtained by BPF (solid), MDFBP (dashed), and FBP (dotted) algorithms from data containing Gaussian noise (upper row) and Poisson noise (lower row).

the π -line with respect to its scanning trajectory is very similar to the relationship between the chords and corresponding fan-beam scanning trajectory. The only difference is that there is an out-of-plane bend to the helix segment.

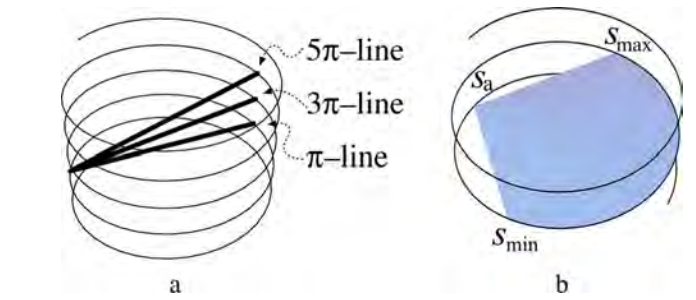


Fig. 16. (a) π -line, 3π -line, and 5π -line segments in a helical scan. (b) Surfaces generated in imaging volume by concatenating π -line segments specified by $s_a = -\pi$ and $s_b \in [-0.5\pi, 0.5\pi]$.

Regarding the nonuniform shape of the variance, one can attribute the high variance in the image periphery to the weighting factors multiplying the data derivatives before backprojection. As the algorithms are essentially the same for chord-image reconstruction in fan- and cone-beam cases, this conclusion should come as no surprise. In the 2-D fan-beam case, the variance nonuniformity and level was reduced by equally weighting reconstructions for both left and right side scans for each chord of the scanning circle. For the helical configuration, it is clear that in a typical scan there will be some overscan for nearly all the chords comprising the volume. But the overscan part of the trajectory does not form a closed loop so using the overscan data to reduce image variance is not as obvious as the case of the circular scan. Future work will focus on how to utilize the overscan data for non-closed trajectories for the purpose of reducing the impact of data noise on chord-base ROI-image reconstruction.

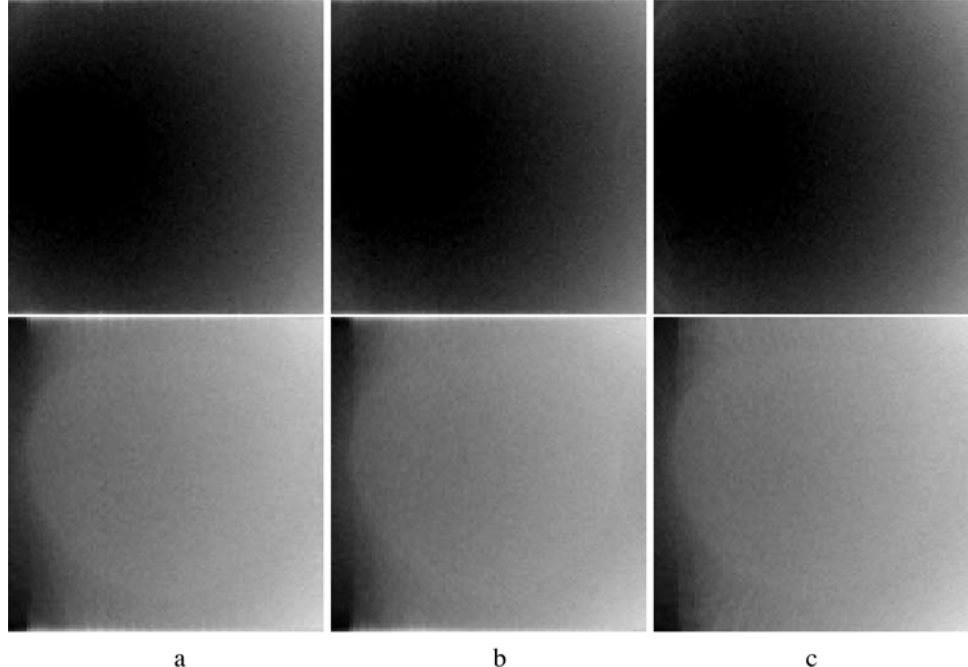


Fig. 17. Empirical variance images on π -line surface shown in Fig. 16(b) obtained by use of (a) BPF, (b) MDFBP, and (c) FBP algorithms from data containing Gaussian noise (upper row) and Poisson noise (lower row), respectively. For the purpose of displaying details in central (i.e., low variance) regions, we have applied a logarithmic scale to variance images. Display windows are $[-1.80, 0.30]$ and $[-1.80, 0.60]$ for Gaussian noise and Poisson noise, respectively.

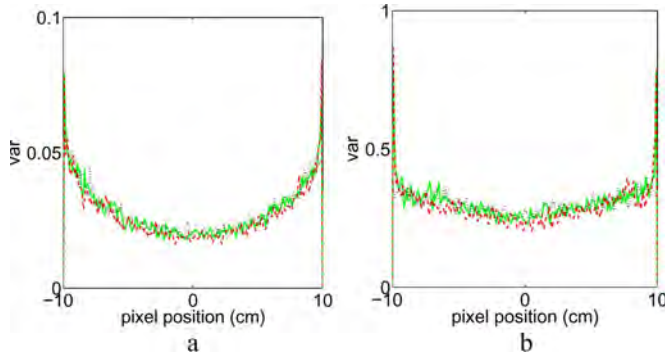


Fig. 18. Variances on central vertical line segment, specified by $s_a = -\pi$ and $s_b = 0$, obtained with BPF (solid), MDFBP (dashed), and FBP (dotted) algorithms from data containing (a) Gaussian noise and (b) Poisson noise.

IV. DISCUSSION

In this paper, we have performed analytic and numerical investigations of the noise properties of chord-based image reconstructions from parallel-, fan-, and cone-beam data. One of the main points of the investigation was to test whether or not the reduced illumination in designing a minimal data set for a particular ROI leads to a significant reduction in exposure. The idea was to compare the statistical properties of the ROI image reconstructed from noise realizations of the minimal data set with noise realizations of the full data set. Similar noise levels were used in both data sets, which are equivalent to modeling similar incident X-ray beam intensities. Our study indicates that the resulting image variance was almost the same for images reconstructed from both data sets.

Thus, the minimal data set for ROI reconstruction leads to a significant overall dose reduction, because the body is exposed to lower amount of ionizing radiation in the reduced scan. For fan-beam and cone-beam imaging, we explored the noise properties of the extreme periphery of the imaging region by investigating large fan- and cone-angles. Image variance nonuniformity was found to be caused by spatially dependent weighting factors in the chord-based reconstruction algorithms. This work represents a study of the noise properties of chord-based reconstruction and of the impact of physical factors on ROI imaging in fan-beam and cone-beam CT. In seeking ways to reduce the impact of noise in volume imaging, we will investigate schemes to incorporate overscan data. The analysis presented in this work can directly be applied to chord-based image reconstruction for general trajectories. Finally, it is important to investigate the behavior of the ROI-reconstruction algorithms when other important factors are included in the data model such as X-ray polychromicity and nonlinear partial volume averaging.

REFERENCES

- [1] A. Katsevich, "Analysis of an exact inversion algorithm for spiral cone-beam CT," *Phys. Med. Biol.*, vol. 47, pp. 2583–2597, 2002.
- [2] Y. Zou and X. Pan, "Exact image reconstruction on PI-line from minimum data in helical cone-beam CT," *Phys. Med. Biol.*, vol. 49, pp. 941–959, 2004.
- [3] Y. Zou and X. Pan, "An extended data function and its backprojection onto PI-lines in helical conebeam CT," *Phys. Med. Biol.*, vol. 49, pp. N383–N387, 2004.
- [4] E. Y. Sidky, Y. Zou, and X. Pan, "Minimum data image reconstruction algorithms with shift-invariant filtering for helical, cone-beam CT," *Phys. Med. Biol.*, vol. 50, pp. 1643–1657, 2005.

- [5] J. D. Pack, F. Noo, and R. Clackdoyle, "Cone-beam reconstruction using the backprojection of locally filtered projections," *IEEE Trans. Med. Imag.*, vol. 24, no. 1, pp. 2317–2336, Jan. 2005.
- [6] Y. Zou, X. Pan, and E. Y. Sidky, "Theory and algorithms for image reconstruction on chords and within regions of interest," *J. Opt. Soc. Amer.*, vol. 22, pp. 2372–2384, 2005.
- [7] S. Zhao, H. Yu, and G. Wang, "A unified framework for exact cone-beam reconstruction formulas," *Med. Phys.*, vol. 32, pp. 1712–1721, 2005.
- [8] T. Zhuang, S. Leng, B. E. Nett, and G. Chen, "Fan-beam and cone-beam image reconstruction via filtering the backprojection image of differentiated projection data," *Phys. Med. Biol.*, vol. 49, pp. 5489–5503, 2004.
- [9] J. D. Pack and F. Noo, "Cone-beam reconstruction using 1D filtering along the projection of m-lines," *Inv. Prob.*, vol. 21, pp. 1105–1120, 2005.
- [10] Y. Zou and X. Pan, "Image reconstruction on PI-lines by use of filtered backprojection in helical cone-beam CT," *Phys. Med. Biol.*, vol. 49, pp. 2717–2731, 2004.
- [11] P. E. Danielsson, P. Edholm, and M. Seger, "Towards exact 3D-reconstruction for helical cone-beam scanning of long objects. A new detector arrangement and a new completeness condition," in *Proc. 1997 Int. Meeting Fully Three-Dimensional Image Reconstruction Radiol. Nucl. Med.*, D. W. Townsend and P. E. Kinahan, Eds., Pittsburgh, PA, 1997, pp. 141–144.
- [12] M. Defrise, F. Noo, and H. Kudo, "A solution to the long-object problem in helical cone-beam tomography," *Phys. Med. Biol.*, vol. 45, pp. 623–643, 2000.
- [13] X. Pan, Y. Zou, and D. Xia, "Peripheral and central ROI-image reconstruction from and data redundancy exploitation in truncated fan-beam data," *Med. Phys.*, vol. 32, pp. 673–684, 2005.
- [14] G. Chen, "An alternative derivation of Katsevich's cone-beam reconstruction formula," *Med. Phys.*, vol. 30, pp. 3217–3226, 2003.
- [15] F. Noo, M. Defrise, R. Clackdoyle, and H. Kudo, "Image reconstruction from fan-beam projections on less than a short scan," *Phys. Med. Biol.*, vol. 47, pp. 2525–2546, 2002.
- [16] Y. Ye and G. Wang, "Filtered backprojection formula for exact image reconstruction from cone-beam data along a general scanning curve," *Med. Phys.*, vol. 32, pp. 654–665, 2005.
- [17] X. Pan, D. Xia, Y. Zou, and L. Yu, "A unified analysis of FBP-based algorithms in helical cone-beam and circular cone- and fan-beam scans," *Phys. Med. Biol.*, vol. 49, pp. 4349–4369, 2004.
- [18] F. Noo, R. Clackdoyle, and J. Pack, "A two-step Hilbert transform method for 2D image reconstruction," *Phys. Med. Biol.*, vol. 49, pp. 3903–3923, 2004.
- [19] X. Pan and L. Yu, "Image reconstruction with shift-variant filtration and its implication for noise and resolution properties in fan-beam computed tomography," *Med. Phys.*, vol. 30, pp. 590–600, 2003.
- [20] R. Proksa, T. Köhler, and J. Timmer, "The n-PI-method for helical cone-beam CT," *IEEE Trans. Med. Imag.*, vol. 19, no. 7, pp. 848–863, Jul. 2000.
- [21] C. Bontus, T. Köhler, and R. Proksa, "A quasiexact reconstruction algorithm for helical CT using a 3-Pi acquisition," *Med. Phys.*, vol. 30, pp. 2493–2502, 2003.

Image representation with non-isotropic spatial resolution on iterative reconstruction accuracy in breast tomosynthesis

Dan Xia, Emil Sidky, Junguo Bian, Ingrid Reiser, Robert Nishikawa, Xiaochuan Pan

Department of Radiology, The University of Chicago
5841 S Maryland Avenue, Chicago, IL 60637

Clinical Relevance/Application:

Breast tomosynthesis has received renewed interest because it can provide 3D information about the breast. This work concerns iterative reconstruction of accurate breast tomosynthesis images.

Purpose:

In current breast tomosynthesis, image representation with non-isotropic spatial resolution is used for reducing computational time. This can, however, lead to artifacts in iterative reconstruction of breast tomosynthesis images. In the work, we investigate the effect of non-isotropic image representation on the reconstruction accuracy. Based upon the investigation, we devise schemes for reducing artifacts in iterative reconstruction.

Materials and Method:

In the work, we focus on investigating the effect of non-isotropic image representation on reconstruction accuracy of iterative algorithms. The iterative algorithms under study include the total-variation (TV) based, expectation maximization (EM), and algebraic reconstruction technique (ART) algorithms. Tomosynthesis data are generated at 12 and 20 views over 50 degrees from phantoms, including a breast phantom. We have reconstructed images by using image representations with different degrees of non-isotropic spatial resolution. Specifically, in each image representation, the ratio between the in-plane and longitudinal resolution for an image voxel is selected to be a value less than 1.

Results:

We have reconstructed images by use of TV-based, EM, and ART algorithms for image representations with different ratios of in-plane and longitudinal resolution. Our results demonstrate that non-isotropic image representation can lead to significant artifacts in reconstructed images. The appearance and severity of the artifacts depend not only upon the ratio between the in-plane and longitudinal resolution but also upon the iterative algorithms. The TV-based algorithm seems to be less susceptible to the effect than the EM and ART algorithms. Through the selection of algorithm parameters, the artifacts can be reduced.

Conclusion:

The non-isotropic image representation can significantly affect reconstruction accuracy obtained with iterative algorithms in breast tomosynthesis.

Image Noise Properties in Circular Sinusoid Cone-beam CT

Dan Xia, *Student Member, IEEE*, Seungryong Cho, *Student Member, IEEE*, Xiaochuan Pan, *Fellow, IEEE*

Abstract—Recently, a reduced circular sinusoid scan was proposed in which data are collected only over an open portion of the full circular sinusoid trajectory. In general, for reconstructing the same ROI image, the reduced-scan approach uses less cone-beam data than what required for a full circular sinusoid scan. It is of practical significance to investigate and evaluate the numerical and noise properties of the image reconstruction for reduced circular sinusoid trajectories. In this work, we carry out studies on the noise properties in images for full and reduced circular sinusoid trajectories reconstructed by use of the recently developed full-scan and reduced-scan FBP algorithms. It can be observed that the spatially dependent weighting factors in the FBP algorithms can lead to non-uniform image variances.

I. INTRODUCTION

Circular trajectory cannot yield data sufficient for exact reconstruction of 3D images. On the other hand, non-circular trajectories such as helical and saddle trajectories can produce data that would allow for exact 3D image reconstruction. In the last several years, there have been significant advances in the development of algorithms for image reconstruction from data acquired with non-circular trajectories [1], [2], [3]. It is expected that, among these non-circular trajectories, the class of circular sinusoidal trajectories, which includes the saddle trajectory as a special case, may find important applications in cardiac imaging and C-arm CT. Based upon the Pack-Noo formula [4], [5], Yang et. al. have developed a filtered backprojection (FBP) algorithm for reconstructing images within regions enclosed by the circular sinusoid trajectory, which we refer to as a full scan [6]. In the last year, we proposed a reduced circular sinusoid scan in which data are collected only over an open portion of the circular sinusoid trajectory. Using the result in [5], [6], we have subsequently derived a reconstruction formula for achieving exact reconstruction of images in a reduced scan. In general, for reconstructing the same ROI image, our reduced-scan approach uses less cone-beam data than what required for a full circular sinusoid scan [6], thus leading a reduction of radiation dose to the imaged subject, scanning time, and possibly imaging artifacts. It is of theoretical and practical significance to investigate and evaluate the numerical and noise properties of the algorithms for full and reduced circular sinusoid trajectories. In the absence of data inconsistencies such as noise and sample aliasing, the algorithms for data acquired with full and reduced circular sinusoid scans yield identical reconstruction. However, in the presence of data inconsistencies, the algorithms for full and reduced circular sinusoid trajectories are expected to behave differently, thus yielding images with different noise properties. In this work, we have carried out studies on the noise properties in images for full and reduced

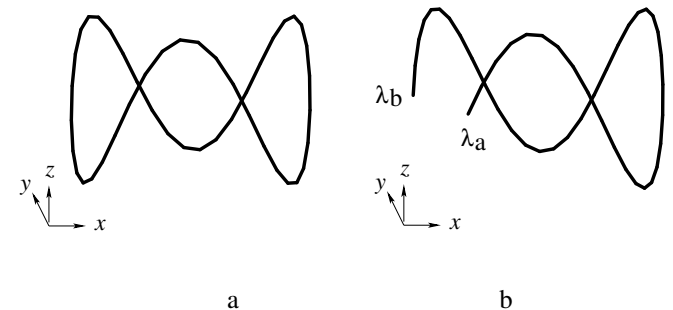


Figure 1. Circular sinusoidal trajectories of order $m = 3$. (a) A full-scan (or, equivalently, closed) circular sinusoidal trajectory, where $\lambda \in [-\pi, \pi]$. (b) A reduced-scan (or, equivalently, open) circular sinusoidal trajectory, where $\lambda \in [\lambda_a, \lambda_b]$, and $-\pi < \lambda_a < \lambda_b < \pi$.

circular sinusoid trajectories reconstructed by use of the recently developed full-scan and reduced-scan FBP algorithms.

II. CIRCULAR SINUSOIDAL TRAJECTORY

In a fixed-coordinate system, a circular sinusoidal source trajectory $\vec{r}_0(\lambda)$ of order m can be expressed mathematically as

$$\vec{r}_0(\lambda) = (R \cos \lambda, R \sin \lambda, h \cos m \lambda)^T, \quad (1)$$

where λ denotes the rotation angle of the source point, R indicates the distance from the source to the rotation axis, h is the amplitude of the source's oscillation along z direction, and the superscript T stands for a matrix transpose. A circular sinusoidal trajectory has a minimal period 2π , and, as shown in Fig. 1a, a closed circular sinusoidal trajectory is formed when the rotation angle λ varies over the entire period of 2π , which we refer to as a full-scan circular sinusoidal trajectory. In contrast, an open circular sinusoidal trajectory is formed, as shown in Fig. 1b, when the scanning angular range is smaller than 2π , which we refer to as a reduced-scan circular sinusoidal trajectory. Notice that, when $m = 2$, the circular sinusoidal trajectory becomes the standard saddle trajectory [6], [7] and that, when h becomes zero, a circular sinusoidal trajectory becomes the 2D circular trajectory.

The cone-beam projection of an object function $f(\vec{r})$ at rotation angle λ is defined as

$$g(\lambda, \hat{\theta}) = \int_0^\infty dt f(\vec{r}_0(\lambda) + t \hat{\theta}), \quad (2)$$

where $\hat{\theta} \in S^2$, and S^2 is a set of all unit vectors over a hemisphere in 3D space.

III. THE RECONSTRUCTION ALGORITHM FOR A FULL SCAN AND A REDUCED SCAN

Consider a full scan with a closed circular sinusoidal trajectory as shown in the left panel of Fig. 2. A plane Π intersects with the trajectory at $n (\geq 3)$ different points $\vec{r}_0(\lambda_i)$, $i = 1, \dots, n$, and $\lambda_1 < \lambda_2 \dots < \lambda_n$. A convex polygon Ω_Π is formed by these intersection points within the plane. It has been shown [6] that image on this polygon can be reconstructed as

$$f(\vec{x}) = \frac{1}{2} \sum_{i=1}^{n-1} \mathcal{K}(\vec{x}, \hat{e}_i, \lambda_i, \lambda_{i+1}) + \frac{1}{2} \mathcal{K}(\vec{x}, \hat{e}_n, \lambda_n, 2\pi + \lambda_1), \quad (3)$$

where

$$\mathcal{K}(\vec{x}, \hat{e}, \lambda^-, \lambda^+) = -\frac{1}{2\pi^2} \int_{\lambda^-}^{\lambda^+} d\lambda \frac{1}{\|\vec{x} - \vec{r}_0(\lambda)\|} g_F(\lambda, \vec{x}, \hat{e}), \quad (4)$$

and the $g_F(\lambda, \vec{x}, \hat{e})$ denotes the filtered projection data, given by

$$g_F(\lambda, \vec{x}, \hat{e}_i) = \int_{-\pi}^{\pi} d\gamma \frac{1}{\sin\gamma} \frac{\partial g(\lambda, \hat{\theta}(\lambda, \vec{x}, \hat{e}_i, \gamma))}{\partial \lambda}, \quad (5)$$

$$\hat{\theta}(\lambda, \vec{x}, \hat{e}_i, \gamma) = \cos\gamma \hat{\alpha}(\lambda, \vec{x}) + \sin\gamma \hat{\beta}(\lambda, \vec{x}, \hat{e}_i), \quad (6)$$

$$\hat{\beta}(\lambda, \vec{x}, \hat{e}_i) = \frac{\hat{e}_i - (\hat{e}_i \cdot \hat{\alpha}(\lambda, \vec{x})) \hat{\alpha}(\lambda, \vec{x})}{\|\hat{e}_i - (\hat{e}_i \cdot \hat{\alpha}(\lambda, \vec{x})) \hat{\alpha}(\lambda, \vec{x})\|}, \quad (7)$$

and

$$\hat{\alpha}(\lambda, \vec{x}) = \frac{\vec{x} - \vec{r}_0(\lambda)}{\|\vec{x} - \vec{r}_0(\lambda)\|}. \quad (8)$$

The filtering directions are given by $\hat{e}_i = \frac{\vec{r}_0(\lambda_{i+1}) - \vec{r}_0(\lambda_i)}{\|\vec{r}_0(\lambda_{i+1}) - \vec{r}_0(\lambda_i)\|}$, $i = 1, \dots, n-1$ and $\hat{e}_n = \frac{\vec{r}_0(2\pi + \lambda_1) - \vec{r}_0(\lambda_n)}{\|\vec{r}_0(2\pi + \lambda_1) - \vec{r}_0(\lambda_n)\|}$.

However, for a reduced scan, data cannot be collected over the trajectory segment between λ_n and $2\pi + \lambda_1$, as shown in the right panel of Fig. 2. Although the actual trajectory segment between λ_n and $2\pi + \lambda_1$ is missing, it can be shown that the contribution of the data on the trajectory segment over the angular range $[\lambda_n, 2\pi + \lambda_1]$ can be replaced by that of the open trajectory segment over angular range $[\lambda_1, \lambda_n]$ (i.e. $\mathcal{K}(\vec{x}, \hat{e}_n, \lambda_n, 2\pi + \lambda_1) = \mathcal{K}(\vec{x}, \hat{e}_n, \lambda_1, \lambda_n)$). Based upon this observation, we can obtain the reduced-scan FBP reconstruction algorithm as

$$f(\vec{x}) = \frac{1}{2} \sum_{i=1}^{n-1} \mathcal{K}(\vec{x}, \hat{e}_i, \lambda_i, \lambda_{i+1}) + \frac{1}{2} \mathcal{K}(\vec{x}, \hat{e}_n, \lambda_1, \lambda_n) \quad (9)$$

IV. NUMERICAL RESULTS

We have performed numerical studies to investigate the noise properties of the full-scan and reduced-scan FBP algorithms. In these studies, a low-contrast Shepp-Logan phantom was used to generate the noiseless cone-beam projection data for the circular sinusoidal trajectories of orders $m=2$ (i.e., saddle trajectory) and $m=3$. We generated the full-scan data at 300 projection views uniformly distributed over $[-\pi, \pi]$. A portion of the full-scan data over the angular range $[-\frac{3}{4}\pi, \frac{3}{4}\pi]$ was used to simulate the data acquired in a reduced scan. By adding stationary Gaussian noise to the noiseless data, we produced 500 sets of noisy data for each scan. From these full-scan and reduced-scan data sets, we

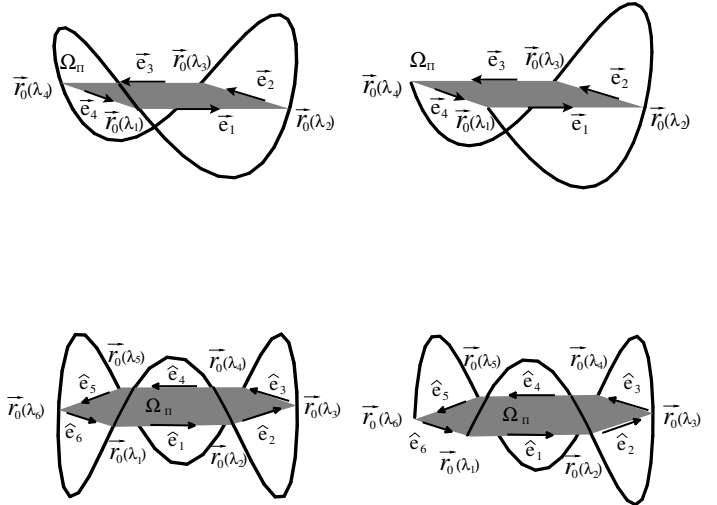


Figure 2. Illustration of the source trajectories in a full scan (left) and a reduced scan (right) for a circular sinusoidal trajectory of orders $m=2$ (top) and $m=3$ (bottom). The plane Ω_Π is parallel to the $x - y$ plane, and intersects with the source trajectory at four ($m=2$) or six ($m=3$) different points, $\vec{r}_0(\lambda_i)$, $i = [1 \dots n]$. The vectors \vec{e}_i , $i = [1 \dots n]$, denote the filtering direction.

reconstructed images by use of the FBP algorithm described in Sec. III.

In Fig. 3, we displayed one of the reconstructed images within a slice at $z = 0$ cm for the full-scan and reduced-scan circular sinusoidal trajectories of order $m=2$. Using the images reconstructed from these noisy data sets, we have computed empirical image variances, which are shown in Fig. 4. For the quantitative comparison, the image variances along the middle horizontal line and the middle vertical line are also displayed in Fig. 4. It can be observed in Fig. 4, that the image variances obtained from the full-scan data and reduced-scan data by use of the FBP algorithms are non-uniform. The reason for this phenomena is that the spatially dependent weighting factors (i.e., $1/|\vec{x} - \vec{r}_0(\lambda)|$) involved in the FBP algorithms can amplify data noise and inconsistencies [8], [9]. One can also observe that, for the full scan, the empirical variance within the central region of the field of the view (FOV) is relative smaller compared to that within the peripheral region, and the variance increases as the distance to the center of rotation increases. However, for a reduced scan in which the trajectory is on the right-hand side of the FOV, the spatially dependent weighting factors results in image variance on the left side is lower than that on the right side of the image space.

Again, we showed in Fig. 5 the reconstructed images within a slice at $z = 0$ cm for the circular sinusoidal trajectory of order $m=3$. The empirical image variances and the corresponding profiles are displayed in Fig. 6. The similar behavior of the image variances can be observed.

V. DISCUSSION

In this work, we have investigated the noise properties in images reconstructed by use of the FBP algorithms for full and reduced circular sinusoid scans. It was observed that the spatially

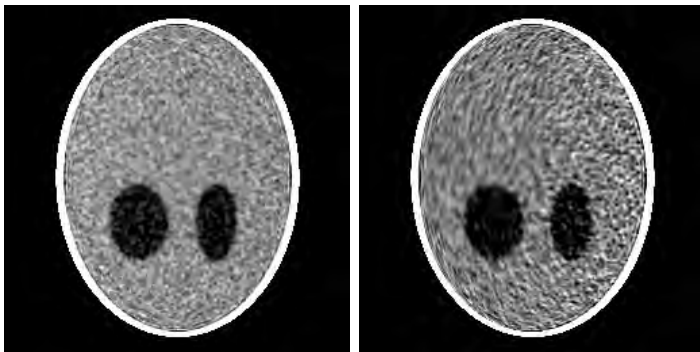


Figure 3. The reconstructed images within the 2D slices at $z = 0$ cm from the noisy projection data acquired in a full-scan (left) and a reduced-scan circular sinusoidal trajectory of order $m=2$ (right). The display grey scale is [1.0, 1.04].

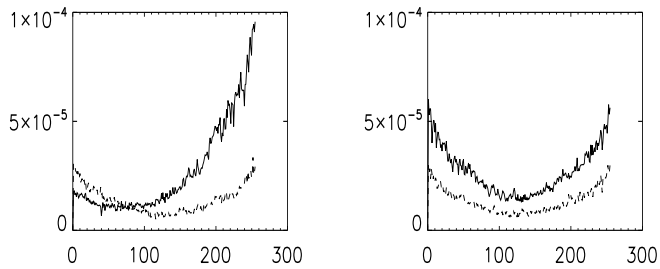
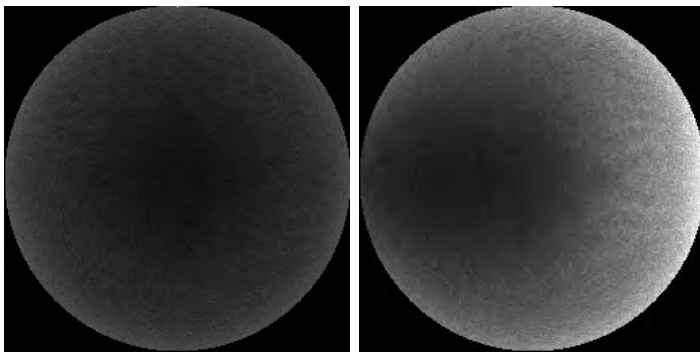


Figure 4. Top row: image variances within the 2D slices at $z = 0$ cm obtain from the noisy projection data in a full scan (left) and a reduced scan (right). Bottom row: Bottom row: variance profiles on the middle horizontal line (left) and the middle vertical line (right) of the variance images in a full scan (dashed line) and a reduced scan (solid line) for the circular sinusoidal trajectory with order $m=2$.

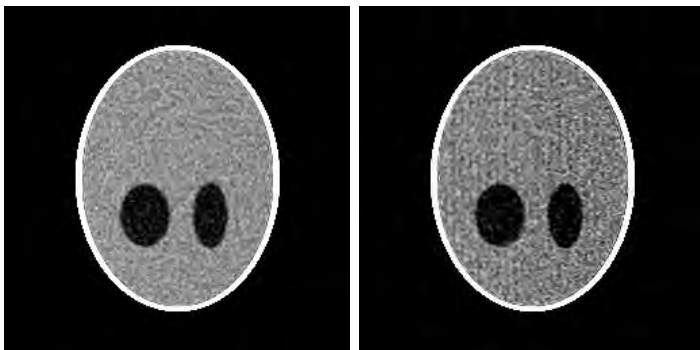


Figure 5. The reconstructed images within the 2D slices at $z = 0$ cm from the noisy projection data acquired in a full-scan (left) and a reduced-scan circular sinusoidal trajectory of order $m=3$ (right). The display grey scale is [1.0, 1.04].

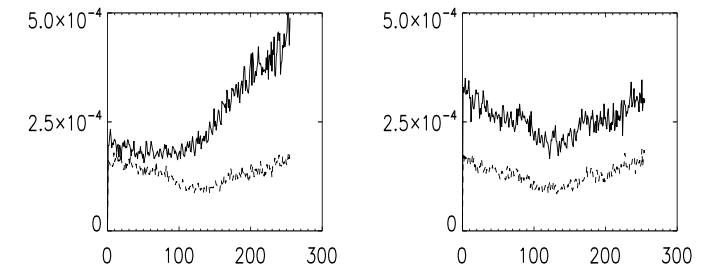
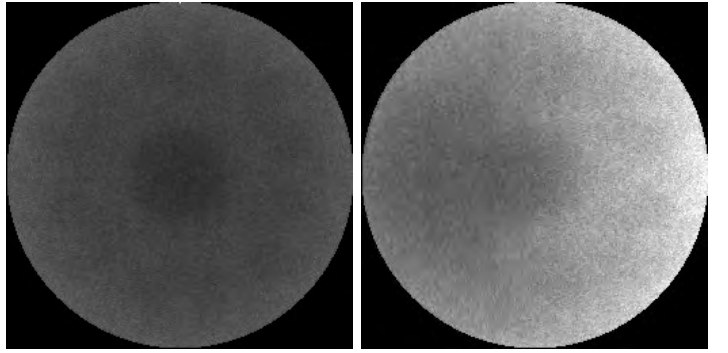


Figure 6. Top row: image variances within the 2D slices at $z = 0$ cm obtain from the noisy projection data in a full scan (left) and a reduced scan (right). Bottom row: Bottom row: variance profiles on the middle horizontal line (left) and the middle vertical line (right) of the variance images in a full scan (dashed line) and a reduced scan (solid line) for the circular sinusoidal trajectory with order $m=3$.

dependent weighting factors in the FBP algorithms can lead to non-uniform image variances.

VI. ACKNOWLEDGMENTS

D. Xia is supported in part by a DoD Predoctoral training grant BC051553, and S. Cho is supported in part by a DoD Predoctoral training grant PC061210. This work was also supported in part by National Institutes of Health grants EB00225 and CA120540.

REFERENCES

- [1] J. D. Pack, F. Noo, and R. Clackdoyle, "Cone-beam reconstruction using the backprojection of locally filtered projections," *IEEE Trans. Med. Imaging*, vol. 24, pp. 2317–2336, 2005.
- [2] A. Katsevich, "Image reconstruction for the circle-arc trajectory," *Phys. Med. Biol.*, vol. 50, pp. 2249–2265, 2005.
- [3] Y. Zou, X. Pan, and E. Y. Sidky, "Theory and algorithms for image reconstruction on chords and within region of interests," *Journal of the Optical Society of America A*, vol. 22, pp. 2372–2384, 2005.
- [4] C. Bontus, T. Köhler, and R. Proksa, "A quasieexact reconstruction algorithm for helical CT using a 3-Pi acquisition," *Med. Phys.*, vol. 30, pp. 2493–2502, 2003.
- [5] J. D. Pack and F. Noo, "Cone-beam reconstruction outside R-lines using the backprojection of 1-d filtered data," in *Proceedings of the 2005 International Meeting on Fully Three-Dimensional Image Reconstruction in Radiology and Nuclear Medicine*, Salt Lake, 2005, pp. 287–290.
- [6] H. Yang, M. Li, K. Koizumi, and H. Kudo, "Exact cone beam reconstruction from a saddle trajectory," *Phys. Med. Biol.*, vol. 51, pp. 1157–1171, 2006.
- [7] J. D. Pack, F. Noo, and H. Kudo, "Investigation of saddle trajectories for cardiac CT imaging in cone-beam geometry," *Phys. Med. Biol.*, vol. 49, pp. 2317–2336, 2004.
- [8] L. Yu and X. Pan, "Halfscan fan-beam computed tomography with improved noise and resolution properties," *Med. Phys.*, vol. 30, pp. 2629–2637, 2003.
- [9] D. Xia, L. Yu, E. Y. Sidky, Y. Zou, N. Zuo, and X. Pan, "Noise properties of chord-image reconstruction," *IEEE Trans. Med. Imaging*, vol. 26, pp. 1328–1344, 2007.

Tomosynthesis with Source Positions Distributed over a Surface

Dan Xia¹, Seungryong Cho¹, Junguo Bian¹, Emil Y. Sidky¹, Charles A. Pelizzari²,
and Xiaochuan Pan¹

¹Department of Radiology, The University of Chicago

²Department of Radiation and Cellular Oncology, The University of Chicago

February 29, 2008

Abstract

In classical tomosynthesis, the X-ray source generally is moved along a curve segment, such as a circular trajectory, within a plane that is perpendicular to the detector plane. Studies suggest that, when the angular coverage and number of projection views are limited, it can be difficult to reconstruct accurate images within planes perpendicular to the detector plane in classical tomosynthesis. In this work, we investigate imaging strategies in tomosynthesis using trajectories that are not confined within a plane perpendicular to the detector plane. We expect that such trajectories can increase data information and thus lead reconstructed images with improved quality. Numerical studies were conducted for evaluating the image-reconstruction quality in classical tomosynthesis and tomosynthesis with trajectories that are not confined within a plane perpendicular to the detector plane. The results of the studies indicate that, with the same number of views, (or, equivalently, the same amount of imaging radiation), data acquired in tomosynthesis with the trajectories that are not confined within a plane perpendicular to the detector plane generally contain more information than that acquired with classical tomosynthesis and can thus yield images with improved quality.

1 Introduction

In the past decade or so, there have been renewed interests in the development of tomosynthesis for applications to breast imaging, image-guided radiation therapy, and security scans [1, 2]. In these studies, the X-ray source often is moved along a curve segment within a plane that is perpendicular to the detector plane. For convenience, we refer to such a source trajectory as a planar trajectory. In some practical applications of tomosynthesis, however, the source trajectory need not be restricted to be within a planar trajectory, and it can be a trajectory in 3D space. For example, the X-ray source may move over a surface such as a portion of the sphere in some applications. In these cases, we refer to the trajectories as non-planar trajectories. We hypothesize that tomosynthesis with certain non-planar trajectories can yield images with improved quality over that obtained with a planar trajectory. In this work, we conduct a preliminary investigation of image reconstruction in classical tomosynthesis that uses a planar trajectory and tomosynthesis that uses a non-planar trajectory. We will apply the TV-minimization iterative algorithm for image reconstruction from data acquired in the two tomosynthesis configurations [3, 4].

2 Scanning configurations for tomosynthesis

In classical tomosynthesis, the x-ray source is moved along a curve segment. When the curve segment is a portion of a circular trajectory, it can be expressed mathematically as

$$\vec{r}_0(\lambda) = (R \sin \lambda, 0, R \cos \lambda) \quad \lambda \in [\lambda_s, \lambda_e], \quad (1)$$

where λ denotes the rotation angle, R is the distance from the source point to the rotation center, and parameters λ_s and λ_e denote the starting and ending angles of the rotation. For each rotation angle λ , a 2D detector is used to measure the projection data, which is the path integral of the x-ray attenuation

coefficient along the rays connecting the source spot and an individual detector bin. In terms of discrete detector array and image array, the data model can be written as the weighted sum over the pixels traversed by the source-bin ray, i.e.,

$$\vec{g} = M\vec{f}, \quad (2)$$

where \vec{f} and \vec{g} are two finite vectors, representing the image function and projection data. The dimensions of \vec{f} and \vec{g} are N_{image} and N_{data} , which denote the elements of discrete image and data arrays. The system matrix M thus composes N_{data} row vectors \vec{M}_i of dimension of N_{image} , yielding $g_i = \vec{M}_i \cdot \vec{f}$. Each element M_{ij} of the system matrix is the length of the i th ray traversing the j th pixel. The process of image reconstruction is to obtain an image represented by the finite vector \vec{f} from knowledge of the data vector \vec{g} and the system matrix M .

In classical tomosynthesis for breast imaging, projection data are measured at about 20 projection views uniformly distributed over an angular range of about 30° . One may improve the image quality of classical tomosynthesis by increasing the number of projections and/or the scanning angular range. However, this approach results in increased imaging radiation dose to the subject. On the other hand, it may be possible to design innovative scanning configurations for acquiring more information than that collected with a planar trajectory in Fig. 1a in classical tomosynthesis, yet without increasing the imaging radiation dose. In this work, we investigate a non-planar imaging configurations in tomosynthesis for acquiring increased data information and thus for achieving improved image quality. In contrast to the planar trajectory in classical tomosynthesis, we study in this work a non-planar trajectory that is on a curved surface. In particular, we consider a source trajectory that consists of two orthogonal curve segments on a portion of a spherical surface, as shown in Fig. 1b. The two curve segments of the non-planar trajectory are expressed as

$$\vec{r}_0(\lambda) = (R \sin \lambda, 0, R \cos \lambda) \quad \lambda \in [\lambda_s, \lambda_1], \quad (3)$$

$$\vec{r}_0(\lambda) = (0, R \sin(\lambda), R \cos(\lambda)) \quad \lambda \in [\lambda_2, \lambda_e]. \quad (4)$$

It can be observed that the two circular segments are chosen to be within x - z and y - z planes. Both of them are on a spherical surface of radius R . Clearly, they are not within a single plane. In this work, we will investigate and compare images reconstructed by use of the TV-minimization algorithm from data acquired with the planar trajectory in classical tomosynthesis and from data obtained with the non-planar trajectory.

3 Reconstruction algorithm

We briefly review the TV-minimization algorithm [3] that is used to reconstruct images from tomosynthesis data in this work. In many imaging applications, it is not uncommon that images to be reconstructed are relatively constant over extended volumes, and that significant, rapid variation in the image may occur only at boundaries of internal structures. In these situations, the image formed by taking the magnitude of its gradient could be approximately sparse. Therefore, the reconstruction strategy considered in the TV-minimization algorithm is to incorporate the assumption of gradient image sparseness on the image function \vec{f} to arrive at a solution from knowledge of the data \vec{g} . Based upon this strategy, the TV-minimization algorithm seeks to find the solution for the optimization problem below:

$$\vec{f}^* = \operatorname{argmin} \|\vec{f}\|_{TV}, \quad (5)$$

with two constraints,

$$|M\vec{f} - \vec{g}| \leq \epsilon \quad \text{and} \quad f_i \geq 0,$$

where \vec{f}^* is the reconstructed image. The inequality used in the first constraint accounts for data inconsistency, such as noise, continuous-to-discrete inconsistency. The parameter ϵ can be selected for controlling the impact level of potential data inconsistency on the image reconstruction. In our investigation of 3D tomosynthesis reconstruction, the TV of a discrete image is defined as

$$\|\vec{f}\|_{TV} = \sum_{s,t,r} |\vec{\nabla} f_{s,t,r}| = \sum_{s,t,r} \sqrt{(f_{s,t,r} - f_{s-1,t,r})^2 + (f_{s,t,r} - f_{s,t-1,r})^2 + (f_{s,t,r} - f_{s,t,r-1})^2}, \quad (6)$$

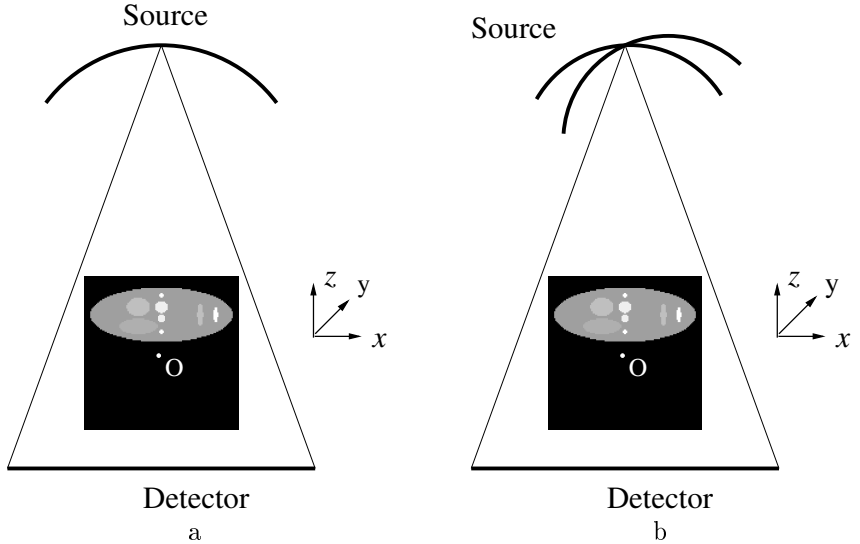


Figure 1: (a) Scanning configuration with a planar trajectory within x - z plane in classical tomosynthesis. (b) Scanning configuration with a non-planar trajectory that consists of two orthogonal, circular segments within x - z and y - z planes, respectively (right).

where s , t , and r indicate the pixel indices within the 3D image.

The implementation of the TV-minimization algorithm includes two major steps: gradient descent method and projection on convex sets (POCS) (see e.g. Sec. 15.4.5 of Ref. [5]). The gradient descent method is used for minimizing the image total variation, whereas the POCS is used for enforcing the constraints imposed by the known projection data. The reason the POCS is used here is that, even in the case of sparse sampling, the size of the projection data sets can be large, and POCS can efficiently handle large data sets.

4 Results

We have conducted numerical studies to investigate image reconstructions by using the TV-minimization algorithm from tomosynthesis data acquired with planar and non-planar trajectories shown in Fig. 1. We use $\vec{r}_0(\lambda)$ to denote a source trajectory. In our study, we first consider classical tomosynthesis in which the source trajectory is a segment of the planar circular trajectory, as shown in Fig. 1a. In the study, we have chosen $R = 7.0$ cm, and $\lambda \in [-\pi/6, \pi/6]$. A flat-panel detector is placed perpendicular to the line connecting the source and the rotation center. The source-to-detector distance is 10.0 cm. A 3D phantom is used to generate cone-beam projection data. It should be pointed out that we have generated analytically the data so that the data contain the so-called continuous-to-discrete inconsistency to reflect realistic imaging conditions in practical tomosynthesis. Such inconsistency may have a significant impact on reconstruction accuracy. In top row of Fig. 2, we display the phantom images within planes specified by $x = 0$ cm, $y = 0$ cm, and $z = 0.5$ cm, respectively. We first generated projection data from the phantom at 30 views uniformly distributed on the planar circular trajectory described above. From the data, we subsequently reconstructed images by using the TV-minimization algorithm, and we displayed in the middle row of Fig. 2 the reconstructed images within planes specified by $x = 0$ cm, $y = 0$ cm, and $z = 0.5$ cm.

We also consider a non-planar trajectory that consists of two orthogonal, circular segments, as shown in Fig. 1b. In this study, geometric parameters such as R and detector-to-source distance were chosen to be identical to those in the above study for the planar circular trajectory. However, the angular ranges of the two orthogonal circular segments are specified by $\lambda \in [-\pi/6, \pi/6]$ and $\lambda \in [\pi/6, \pi/2]$, respectively. Using this non-planar trajectory, we generate analytically projection data from the same phantom over total 30 views of which 15 views are uniformly distributed on each of the two orthogonal circular segments.

The number of views over one of the two trajectories is only one half of that for the planar trajectory. Therefore, the total imaging radiation doses in the studies involving the planar and non-planar trajectories are the same. From the generated data, we reconstructed images by use of the TV-minimization algorithm. In the bottom row of Fig. 2, we show the reconstructed images within planes specified by $x = 0$ cm, $y = 0$ cm, and $z = 0.5$ cm, respectively. We also display in Fig. 3 the profiles in the reconstructed images along the axes specified by $x = 0$ cm and $y = 0$ cm, by $y = 0$ cm and $z = 0$ cm, and by $x = 0$ cm and $z = 0$ cm, respectively. Comparison of the results in Figs. 2 and 3 suggests that tomosynthesis with a non-planar trajectory may yield more data information, and thus images with higher quality, than classical tomosynthesis with a planar trajectory.

5 Conclusion

In the work, we have investigated non-planar trajectories in tomosynthesis for yielding more data information than classical tomosynthesis with a planar trajectory. Our preliminary study indicates that with the same number of projection views (or, equivalently, the same dose level,) the new imaging configuration may lead to images with improved quality over that obtained with classical tomosynthesis. The proposed imaging strategy and TV-minimization reconstruction algorithm may find applications in IGRT, security scan, industrial imaging, and sample/specimen evaluation.

References

- [1] Senhu Li and Huabei Jiang, “A practical method for three-dimensional reconstruction of joints using a C-arm system and shift-and-add algorithm,” *Med. Phys.*, vol. 32, pp. 1491–1499, 2005.
- [2] G. Bachar, J. H. Siewerdsen, M. J. Daly, D. A. Jaffray, and J. C. Irish, “Image quality and localization accuracy in C-arm tomosynthesis-guided head and neck surgery,” *Med. Phys.*, vol. 34, pp. 4664–4677, 2007.
- [3] E. Sidky, C.-M. Kao, and X. Pan, “Accurate image reconstruction from few-views and limited-angle data in divergent-beam CT,” *J. X-Ray Sci. and Tech.*, vol. 14, pp. 119–139, 2006.
- [4] T. Wu, R. H. Moore, E. A. Rafferty, and D. B. Kopans, “A comparison of reconstruction algorithms for breast tomosynthesis,” *Med. Phys.*, vol. 31, pp. 2636–2647, 2004.
- [5] H. H. Barrett and K. J. Myers, *Foundations of Image Science*, John Wiley & Sons, Inc., Hoboken, New Jersey, 2004.

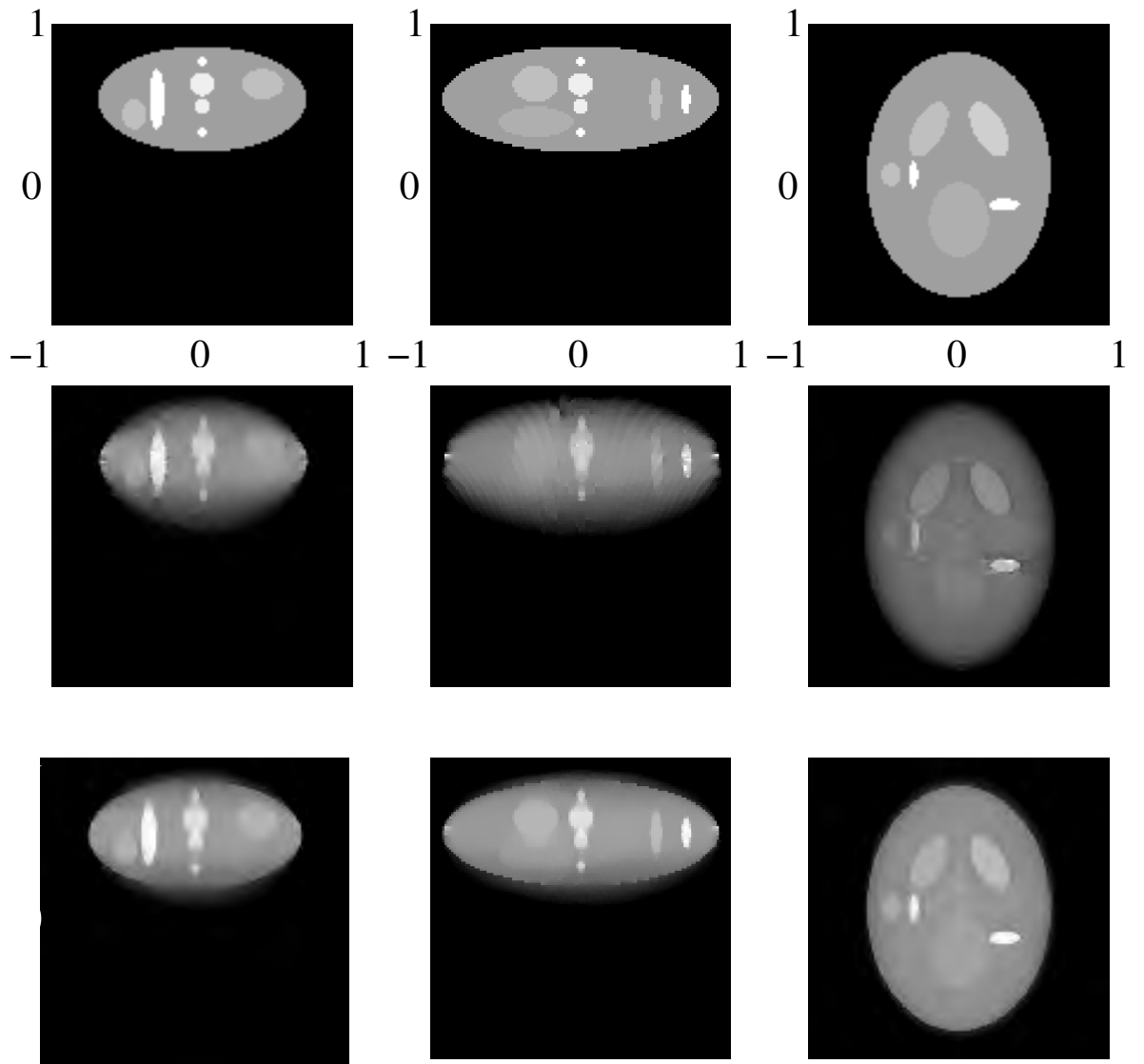


Figure 2: True image (top row) and images reconstructed from 30-view projection data acquired with the planar trajectory (middle row) and the non-planar trajectory (bottom row). The first, second, and third columns represent the images within 2D slices specified by $x = 0$ cm, $y = 0$ cm, and $z = 0.5$ cm, respectively. The display gray scale is $[0, 2]$. The horizontal and vertical axes have a unit of cm.

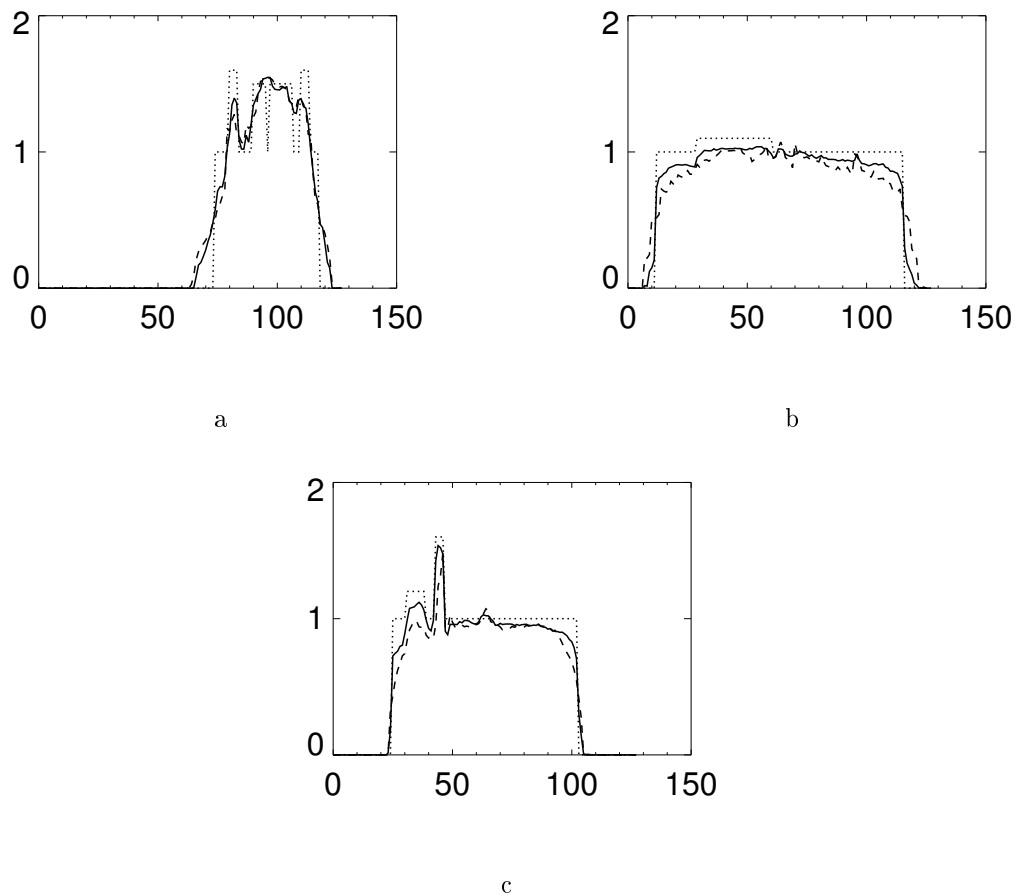


Figure 3: Profiles of the images reconstructed from 30-view projection data acquired with the planar trajectory (dashed curve) and the non-planar trajectory (solid curve) along (a) the z -axis, (b) the x -axis, and (c) y -axis, respectively. The dotted curve indicates the true profiles along these lines.

Non-circular Scans and Image Reconstruction for Breast CT

Junguo Bian^a, Nathan J. Packard^b, Kai Yang^b, Dan Xia^a,
John M. Boone^b, and Xiaochuan Pan^a

^a Department of Radiology, The University of Chicago, Chicago, IL 60637;

^b University of California Davis Medical Center, Sacramento, CA 95817

ABSTRACT

Current dedicated, cone-beam breast CT scanners generally use a circular scanning configuration largely because it is relatively easy to implement mechanically. It is also well-known, however, that a circular scanning configuration produces insufficient cone-beam data for reconstructing accurate 3D breast images. Approximate algorithms, such as FDK has been widely applied to reconstruct images from circular cone-beam data. In the FDK reconstruction, it is possible to observe artifacts such as intensity decay for locations that are not within the plane containing the circular source trajectory. Such artifacts may potentially lead to false positive and/or false negative diagnosis of breast cancer. Non-circular imaging configurations may provide data sufficient for accurate image reconstruction. In this work, we implement, investigate innovative, non-circular scanning configurations such as helical and saddle configurations for data acquisition on a dedicated, cone-beam breast CT scanner, and develop novel algorithms to reconstruct accurate 3D images from these data. A dedicated, cone-beam breast CT scanner capable of performing non-circular scanning configurations was used in this research. We have investigated different scanning configurations, including helical and saddle configurations. A Debrise disk phantom and a dead mouse were scanned by use of these configurations. For each configuration, cone-beam data were acquired at 501 views over each turn. We have reconstructed images using our BPF algorithm from data acquired with the helical scanning configuration.

1. INTRODUCTION

There has recently been a renewed interest in developing dedicated breast CT scanner because of its potential to provide 3D images of high quality, potentially leading to improved sensitivity and specificity in breast cancer detection. Current dedicated, cone-beam breast CT scanners^{1,2} use a circular scanning configuration for data acquisition. It is well-known, however, that a circular scanning configuration cannot yield cone-beam data sufficient for reconstructing accurate 3D images of the breast. We hypothesize that advanced, non-circular scanning configurations and appropriate reconstruction algorithms can yield images with quality higher than that obtained with a circular scanning configuration and the approximate FDK algorithm. In this work, we investigate and develop advanced, non-circular scanning configurations for data acquisition in dedicated breast CT, and we also develop algorithms for reconstructing accurate 3D images from the acquired data.

2. METHOD AND MATERIALS

2.1 Imaging configuration

In this study, we have used a dedicated, cone-beam breast CT scanner capable of performing non-circular scanning configurations at UC-Davis.³⁻⁵ With the patient lying prone on a table of the scanner, the patient's breast hangs in a pendulant position through an opening in the table. The source and flat-panel detector can be rotated around and/or translated with respect to the patient's breast for collecting cone-beam data. Using a Debrise disk phantom and a dead mouse as the imaged subjects, we have investigated several advanced, non-circular scanning configurations such as the helical and saddle scanning configurations. The helical configuration has most widely been adopted in diagnostic CT for achieving rapid data acquisition. Helical scan is a natural extension of circular scan, and it has been shown to yield data sufficient for accurate 3D reconstruction. The saddle scanning configuration can be interpreted as a generalization of the circular scanning configuration, in which the z-component of the X-ray source will now vary periodically. It can yield data sufficient for accurate 3D reconstruction of breast images. The implementation of a saddle configuration requires the X-ray source movement along the z-axis according to a non-linear function of the rotation angle.

We use the Defrise disk phantom in our study because it provides a test on the reconstruction accuracy along the longitudinal direction. For each configuration, we acquired cone-beam data at 501 views uniformly distributed over a turn. In certain non-circular scanning configurations under study such as the saddle configuration, the X-ray source needs to be translated as a non-linear function of the source rotation angle. Because of the mechanical limitation of motor control, such a non-linear movement was realized through a series of analytically pre-determined source positions and additional interpolated positions between two adjacent pre-determined source positions. In the implementation of the saddle scanning configuration, we computed 250 source positions distributed equally over 2π using an analytic formula. Based upon the 250 pre-calculated source positions, we interpolated additional 250 source positions for additional data collection.

2.2 Reconstruction algorithm

In the last few years, significant advances have been made in the development of theoretically exact algorithms for image reconstruction from cone-beam projections. These algorithms were initially developed for a helical trajectory. However, they have subsequently been extended to reconstruct images from cone-beam projections acquired with other trajectories, for example, saddle trajectory, line+circle trajectory and other general trajectory. One of these algorithms is the back-projection filtration (BPF) algorithm for reconstructing images on chords.⁶ A unique property of the BPF algorithm is that it can reconstruct an image on a chord from truncated data as long as the data on the intersection segment of the chord with the object is non-truncated. It has been shown that the property of the BPF algorithm can be exploited for obtaining an region of interest (ROI) image from projection data containing truncations. ROI imaging can reduce the dose to patient and it has the potential benefits of scatter reduction. The reconstruction formula for BPF can be written as:

$$f_c(x_c, \lambda_a, \lambda_b) = \frac{1}{2\pi^2} \frac{1}{\sqrt{(x_{c2} - x_c)(x_c - x_{c1})}} \left[\int_{x_{c1}}^{x_{c2}} \frac{dx'_c}{x_c - x'_c} \sqrt{(x_{c2} - x'_c)(x'_c - x_{c1})} g_c(x'_c, \lambda_a, \lambda_b) + C \right] \quad (1)$$

$$g_c(x_c, \lambda_a, \lambda_b) = \int_{\lambda_a}^{\lambda_b} \frac{\operatorname{sgn} \left[-\hat{\beta} \cdot \hat{e}_w \right] d\lambda}{|\vec{r}(x_c) - \vec{r}_0(\lambda)|} \left. \frac{d}{d\lambda} P(u_d, v_d, \lambda) \right|_{\hat{\beta}} \quad (2)$$

where λ denotes the rotation angles of the x-ray source, chord is defined as the line segment connecting two points $\vec{r}_0(\lambda_a)$ and $\vec{r}_0(\lambda_b)$ on the trajectory, x_c denotes a point on the chord, which relates to the spatial vector as $\vec{r}(x_c) = \frac{1}{2}[\vec{r}_0(\lambda_a) + \vec{r}_0(\lambda_b)] + x_c \hat{e}_c$, \hat{e}_c indicates the direction along the chord, $x_c \in [-l, l]$, $l = \frac{1}{2}|\vec{r}_0(\lambda_a) - \vec{r}_0(\lambda_b)|$ denotes one half of the chord length, $f_c(x_c, \lambda_a, \lambda_b)$ is the image function on the chord, $g_c(x_c, \lambda_a, \lambda_b)$ is the back-projection of weighted data derivative onto the chord, $\hat{\beta}$ is the unit vector along the projection direction, and \hat{e}_w points along the rotation axis. The detector is assumed to be a flat panel detector, and $P(u_d, v_d, \lambda)$ is the projection data at view angle λ .

The helical trajectory under study can be expressed as

$$\vec{r}_0(\lambda) = \left(R \cos \lambda, R \sin \lambda, \frac{h}{2\pi} \lambda \right)^T \quad (3)$$

where R is the distance from the source point to the rotation axis, and h is the pitch of the helical trajectory, which is defined as the translation distance of the imaged object during one turn of gantry rotation.

The saddle trajectory under study can be expressed as

$$\vec{r}_0(\lambda) = (R \cos \lambda, R \sin \lambda, h \cos 2\lambda)^T \quad (4)$$

which can be interpreted as a generalization of circular trajectory.

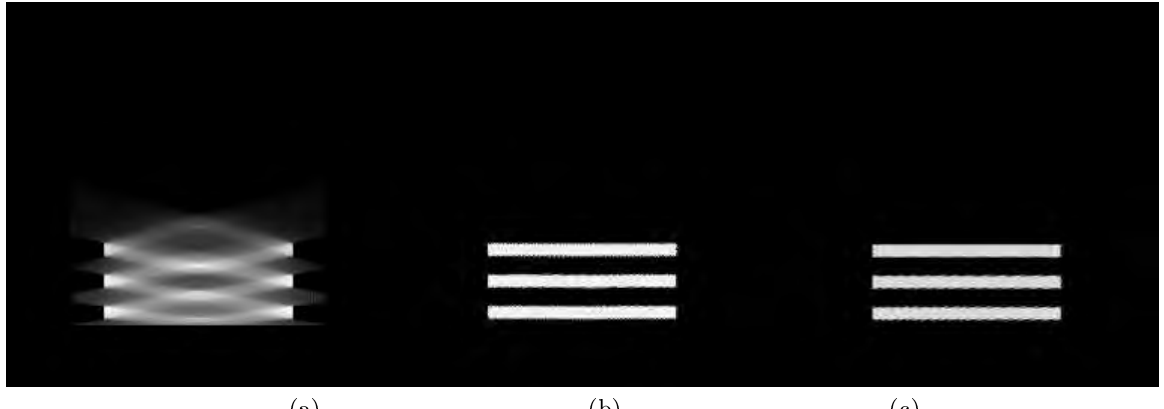


Figure 1. (a) Image reconstructed by use of the FDK algorithm from circular cone-beam data. (b) Image reconstructed by use of the BPF algorithm from helical cone-beam data. (c) Image reconstructed by use of the BPF from saddle cone-beam data.)

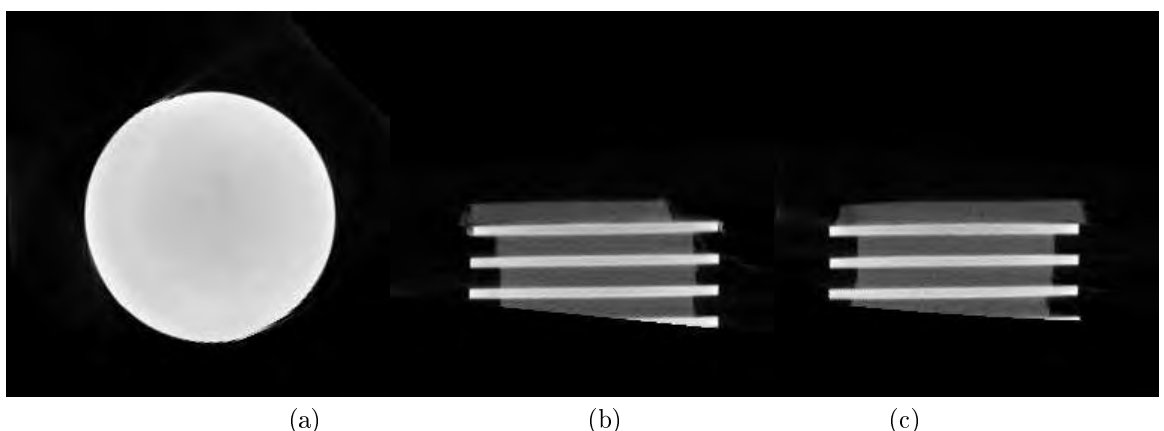


Figure 2. Images within (a) transverse, (b) sagittal, and (c) coronal slices, respectively, reconstructed by use of the BPF algorithm from real data acquired with a helical scanning configuration.

3. RESULTS

We have conducted studies using both computer-simulated and real phantom data. In the simulation studies, we acquire cone-beam data at 501 views uniformly distributed over 2π angular range. A flat-panel detector used has a size of 512x512, and an image is reconstructed on a 256x256x256 array. Using the Defrise phantom, we first generated cone-beam projection data at 501 views with the circular trajectory. From the circular cone-beam data, we reconstructed images by using the FDK algorithm. In Fig. 1a, we display one of such reconstructed images in which strong artifacts can be observed. We also generated cone-beam projection data using a helical trajectory and a saddle trajectory. From these data, we used the BPF algorithm to reconstruct images, which are shown in Figs. 1b and 1c.

We have also implemented helical, saddle, and other non-circular scanning configurations on the dedicated breast CT scanner. Using these configurations, data were collected from the Defrise disk phantom from which we reconstructed images by use of the BPF algorithm. In Fig. 2, we show the reconstructed images within (a) the transverse, (b) sagittal, and (c) coronal slices, respectively, from data acquired with the helical scanning configuration. Clearly, the helical scanning configuration can yield data sufficient for accurate reconstruction of 3D images. Moreover, we used the helical configuration to acquire a data set from the mouse from which we reconstructed a 3D mouse image using the BPF algorithm. In Fig. 3, we display mouse images within (a) a transverse, (b) a sagittal, and (c) a coronal slice, respectively.

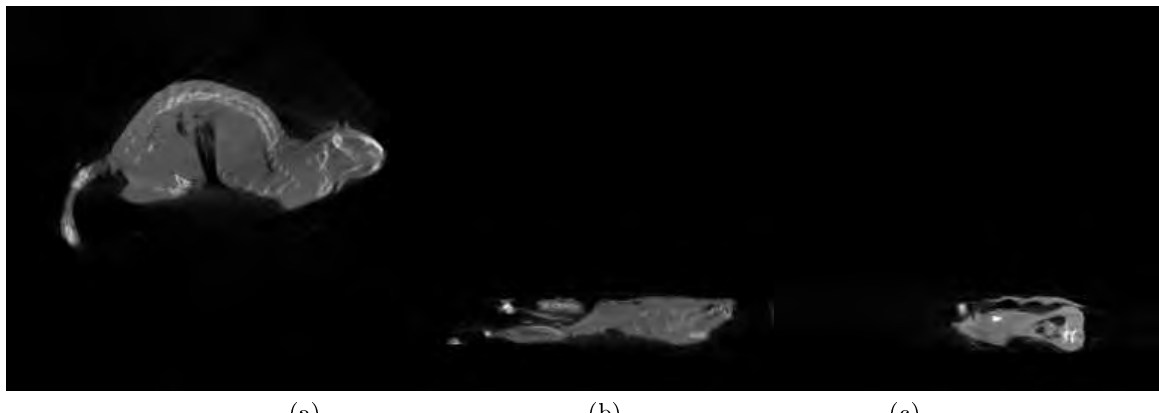


Figure 3. Mouse images within (a) transverse, (b) sagittal, and (c) coronal slices, respectively, reconstructed by use of the BPF algorithm from data acquired with a helical scanning configuration.

4. CONCLUSION

In this work, we have conducted a preliminary investigation and implementation of non-circular scanning configurations on a dedicated breast CT scanner for acquiring cone-beam data sufficient for accurate image reconstruction. We also studied image reconstruction from data acquired with the non-circular trajectories under studies by using the recently developed BPF algorithm. Results of the studies suggest that non-circular scanning configurations can be developed on dedicated, cone-beam breast CT for acquiring data sufficient for accurate 3D reconstruction of breast images.

REFERENCES

1. J. M. Boone, A. L. Kwan, K. Yang, G. M. Burkett, K. K. Lindfors, and T. R. Nelson, "Computed tomography for imaging the breast," *J. Mammary Gland Biol. and Neoplasia* **11**, pp. 103–111, 2003.
2. B. Chen and R. Ning, "Cone-beam volume ct breast imaging: Feasibility study," *Med. Phys.* **29**(5), pp. 755–770, 2002.
3. J. M. Boone, A. L. C. Kwan, J. A. Seibert, N. Shah, K. K. Lindfors, and T. R. Nelson, "Technique factors and their relationship to radiation dose in pendant geometry breast ct," *Medical physics* **32**(12), pp. 3767–3776, 2005.
4. K. Yang, A. L. C. Kwan, and J. M. Boone, "Computer modeling of the spatial resolution properties of a dedicated breast ct system," *Medical physics* **34**(6), pp. 2059–2069, 2007.
5. A. L. C. Kwan, J. M. Boone, K. Yang, and S. Huang, "Evaluation of the spatial resolution characteristics of a cone-beam breast ct scanner," *Medical physics* **34**(1), pp. 275–281, 2007.
6. Y. Zou, X. Pan, and E. Y. Sidky, "Theory and algorithms for image reconstruction on chords and within region of interests," *Journal of the Optical Society of America* **22**, pp. 2372–2384, 2005.